

# UC Merced

## UC Merced Electronic Theses and Dissertations

### Title

Organo-Metalic Halide Perovskite Photonics

### Permalink

<https://escholarship.org/uc/item/8f4581n7>

### Author

Delmas, William

### Publication Date

2022

Peer reviewed|Thesis/dissertation

UNIVERSITY OF CALIFORNIA, MERCED

**Organo-Metalic Halide Perovskite Photonics**

by **William Grant Delmas**

A dissertation submitted in partial  
satisfaction of the requirements for the  
degree of

Doctorate of Philosophy

in

Physics

**Committee in Charge:**

Professor Chih-Chun Chien (Chair)

Dr. Tiziana Bond

Professor Sayantani Ghosh

Professor Michael Scheibner

Professor Jay Sharping

2022

Copyright  
William Grant Delmas, 2022  
All rights reserved

The dissertation of William Grant Delmas', titled , Organo-Metalic Halide Perovskite Photonics, is approved, and it is acceptable in quality and form for publication on microfilm and electronically:

Date of Signature

---

Dr. Jay Sharping  
Associate Professor, Department of Physics  
University of California, Merced  
Dissertation Committee Member

---

Dr. Tiziana Bond  
Staff Scientist, Engineering Branch  
Lawrence Livermore National Laboratory  
Dissertation Committee Member

---

Dr. Sayantani Ghosh  
Professor, Department of Physics  
University of California, Merced  
Dissertation Advisor

---

Dr. Michael Scheibner  
Associate Professor, Department of Physics  
University of California, Merced  
Dissertation Advisor

---

Dr. Chih-Chun Chien  
Associate Professor, Department of Physics  
University of California, Merced  
Dissertation Committee Chair

# Contents

List of Figures	vii
List of Tables	xii
Abbreviations	xiv
Abstract	xv
Curriculum Vita	xvi
Acknowledgements	xx
<b>1 Introduction</b>	<b>1</b>
1.1 Motivation and Purpose . . . . .	2
<b>2 Optical, Electrical and Chemical Properties of Perovskite</b>	<b>3</b>
2.1 Crystal Structure . . . . .	3
2.1.1 Structural Phase Dynamics . . . . .	4
2.2 Chemical Stability . . . . .	5
2.2.1 Moisture . . . . .	6
2.2.2 Oxygen . . . . .	6
2.2.3 Solar Spectrum Illumination . . . . .	7
2.2.4 Thermal Stress . . . . .	7
2.2.5 Mechanical Stress . . . . .	8
2.3 Band Contributions . . . . .	8
2.4 Chemical Tunability . . . . .	9
2.4.1 Changes in Band Gap . . . . .	9
2.4.2 Increased Light Absorption . . . . .	10
2.4.3 Increased Stability . . . . .	10
2.5 Defect Tolerance . . . . .	10

---

<b>3</b>	<b>3-D Thin Film Perovskites for Space-Based Photovoltaics</b>	<b>12</b>
3.1	Thin Film Basics . . . . .	13
3.1.1	Perovskite Thin Film Synthesis . . . . .	13
3.1.2	Perovskite Grains . . . . .	14
3.2	Encapsulation of Perovskite films to Meet AIAA S-11 Photovoltaic Standards . . . . .	15
16		
3.2.2	Results and Discussion: Encapsulated Devices . . . . .	20
3.2.3	Conclusions . . . . .	28
3.3	10 Month Space Flight of Sample 18 . . . . .	29
3.3.1	Timeline . . . . .	29
3.3.2	How Perovskite Optical Properties Correlate to Electrical Performance . . . . .	31
3.3.3	Degradation Mechanisms in Low Earth Orbit . . . . .	32
3.3.4	Optical Analysis . . . . .	33
3.3.5	Confocal Analysis . . . . .	33
3.3.6	Room Temperature PL and TRPL Analysis . . . . .	35
3.3.7	Temperature Dependent Properties . . . . .	36
3.3.8	Photostability . . . . .	37
3.3.9	Conclusion . . . . .	37
3.4	Conclusion . . . . .	38
<b>4</b>	<b>Charge Dynamics of 2-D Perovskites</b>	<b>43</b>
4.1	Crystal Structure . . . . .	43
4.2	Effect of Quantum Confinement . . . . .	43
4.2.1	Self Trapped Excitons . . . . .	45
4.3	Manganese Doping in 2D Perovskites . . . . .	45
4.4	Authors Work: Mn Doped 2DLP Energy Transfer Dynamics . . . . .	46
4.4.1	Materials and Synthesis . . . . .	46
4.4.2	Room Temperature Dynamics . . . . .	48
4.4.3	Cryogenic Photodynamics . . . . .	48
4.4.4	Energy Transfer Dynamics Calculations . . . . .	49
4.5	Spin Dynamics . . . . .	53
4.6	Conclusion . . . . .	55
<b>5</b>	<b>Zero Dimensional Colloidal Perovskite Quantum Dots</b>	<b>56</b>
5.1	Effect of Quantum Confinement . . . . .	56
5.2	Effect of Ligands . . . . .	57
5.2.1	Surface Passivation . . . . .	57
5.2.2	Controlled Growth . . . . .	58
5.2.3	Surface Energy Manipulations . . . . .	58

---

5.3	Authors Work: Effect of Conductive Ligands on PQD Properties . . .	58
5.3.1	Materials and Synthesis . . . . .	59
5.3.2	Ligand Dynamics . . . . .	61
5.3.3	Room Temperature PL . . . . .	61
5.3.4	Conductive Ligand's Effect on PQD Lifetime . . . . .	63
5.3.5	Temperature Dependent Electronic Behaviour . . . . .	66
5.4	Conclusion . . . . .	70
<b>6</b>	<b>PQD Single Photon Emitters</b>	<b>72</b>
6.1	Quantum Emitter Basics . . . . .	72
6.1.1	Photon Purity . . . . .	73
6.1.2	Repetition-Rate . . . . .	73
6.1.3	Indistinguishability . . . . .	73
6.2	State of SPE Research . . . . .	73
6.3	Core Shell Colloidal Quantum Dots . . . . .	75
6.3.1	Progress to date . . . . .	75
6.3.2	Auger Recombination in Core-Shell Nonstructures . . . . .	76
6.3.3	Enhanced light-matter coupling . . . . .	77
6.4	Perovskite Quantum Dots . . . . .	77
6.4.1	Tunability of Perovskites . . . . .	77
6.4.2	Progress to date . . . . .	78
6.5	Authors Work: Room Temperature Analysis of Single PQDs . . . . .	78
6.5.1	Materials and Methods . . . . .	79
6.5.2	PL and Antibunching of Low-Density PQD Ensembles . . . . .	79
6.6	Conclusion . . . . .	81
<b>7</b>	<b>Conclusion and Outlook</b>	<b>82</b>
<b>A</b>	<b>Semiconductor Investigation Tools</b>	<b>85</b>
A.1	Transmission Spectroscopy . . . . .	86
A.1.1	Theory . . . . .	86
A.1.2	Experimental . . . . .	87
A.1.3	Tauc Plot Analysis . . . . .	88
A.2	Photoluminescence (PL) Spectroscopy . . . . .	89
A.2.1	Photon Emission Basics [1] . . . . .	89
A.2.2	Direct Measurement of PL and TRPL . . . . .	91
A.2.3	Absorption . . . . .	94
A.2.4	Photo-active Stability . . . . .	94
A.2.5	Spectral Selective TRPL . . . . .	96
A.2.6	Power Dependent Excitation Spectroscopy . . . . .	96
A.2.7	Temperature Dependent Spectroscopy . . . . .	97

A.3 Microscopy . . . . .	97
--------------------------	----



# List of Figures

2.1	<b>Halide Perovskite Crystal Structure.</b> $ABX_3$ crystal structure where the A site cation can be the organic molecules methylammonium ( $CH_3NH_3$ ), Formadimium ( $CH_5N_2$ ) or Cesium ( $Cs$ ). The B site metal can be lead ( $Pb$ ) or tin ( $Sn$ ). The X site halides can be iodide ( $I$ ), chloride ( $Cl$ ) or bromide ( $Br$ ). . . . .	4
2.2	<b>Structural Phase Dynamics</b> A: Orhtorombic Phase, B: Tetroagonal, C: Cubic Phase . . . . .	4
2.3	<b>Binary Perovskite Degradation.</b> A shows a MAPI perovskite film after synthesis. Image 1" by 1". B shows a similarly synthesised film that has fully degraded into $PbI_2$ , evidenced by its change in color from black to yellow. Image 1/2" by 1/2" . . . . .	5
2.4	<b>Halide Perovskite Band Contributions.</b> A/B: shows the typical orbital structure of the Sn, Pb / Cl, Br, I constituents of the perovskite crystal structure. C: Shows how the overlapping atomic orbitals form the perovskite band gap. D: Is the typical bandgap for perovskite crystals with varying chemistries. . . . .	11
3.1	<b>Perovskite Grains:</b> SEM of a perovskite thin film. Total image width is 30 $\mu m$ . . . . .	14
3.2	<b>Perovskite Structures Studied</b> A: Basic perovskite encapsulated with glass. B: Perovskite covered in $SiO_2$ between 50 nm and 150 nm. C: Same structure as B but with the addition of a 2 nm to 4 nm of APTES ligands. D: Transmission spectra of the three structures after synthesis. Inset: Structure of the APTES ligand. . . . .	16
3.3	<b>Perovskite Device Synthesis</b> A: Perovskite device structure synthesis within glove box. B: Perovskite device structure synthesis in ambient conditions within a glove box. . . . .	17
3.4	<b>Perovskite Transmission Spectra</b> Transmission spectrum of brand new MAPI thin film (Bottom left / dark grey film) and a sample that has fully degraded into $PbI$ (Top right/ yellow film). . . . .	20

3.5	<b>Simple Perovskite Structure Behaviour</b> A: Displays the t=84 hrs on the right and t=300 hrs images of sample 1. B: Displays the vertical structure of the sample with their thicknesses. C: Displays the transmission curves of the sample at different exposure times to the humid environment. . . . .	22
3.6	<b>Absorption Intensity Decay over 300 hrs</b> Displays the the decay of the AI over a given time of 300 hours. . . . .	24
3.7	<b>Band Gap Extrapolation</b> A/B/C: Tauc plot of Sample 1/2/3 over time. D: All the sample band gaps as a function of time. . . . .	25
3.8	<b>Moisture Ingression Simulation</b> Dynamic simulation of moisture particles diffusing into the encapsulant at a single point of entry. The length scales and time constants involved are arbitrary and just for illustration purposes. . . . .	27
3.9	<b>Moisture Penetration Depth</b> Moisture penetration as a function of depth from the encapsulant/air interface. . . . .	28
3.10	<b>MISSE13 sample pre- and post-flight</b> (A) Schematic of assembled layers. (B) Photographs of edges of (top) Control A and (bottom) Flight sample, both post-flight. (C) ISS on day 52 of MISSE duration. Yellow arrows indicate the position of the MISSE13 sample. . . . .	30
3.11	<b>The Role of Radiation</b> Results of SRIM (Stopping and Range of Ions in Matter) and TRIM (Transport of Ions in Matter) simulations. A: SRIM Penetration depth of protons in borosilicate glass as a function of energy. Inset shows the energy of protons within the 1mm thick cover glass. B: TRIM ion simulation for perovskite sample using 14 MeV protons. . . . .	33
3.12	<b>Confocal Analysis of MISSE 13 Sample</b> A/B/C: Displays the 400/490/700 nm to 410/530/800 nm collection maps for the edge of the Ground Control Sample. D/E: Are the emission maps for the Ground/Emission Samples. F: Displays the statistics and averages for the $PbI_2$ inclusions in the two samples. A,B,C images are identical in dimension and scale bars are 200 $\mu\text{m}$ . D,F,E,G images are identical in demension and scale bars are 200 $\mu\text{m}$ . . . . .	39
3.13	<b>PL and TRPL Maps</b> A/B Statistical distributions Energy and Lifetimes from PL and TRPL Maps. . . . .	40
3.14	<b>Resorption Measurements</b> Redshift as a function of the probe beam distance. . . . .	40
3.15	<b>Temperature Dependent PL</b> A/B: Temperature dependent PL Maps, where each temperature is a PL spectra. C: Displays the temperature dependent PL map of the flight sample after light soaking. D/E: Displays the PL-Energy / PL-Linewidth as a function of temperature. Both maps are in steps of 10K. . . . .	41

3.16	<b>AM 1.5 Photo-stability Test</b> A/B: The PL intensity/Energy as a function of time. With insets of the sample images before and after the test. Both A and B are to 15 hours. . . . .	42
4.1	<b>2DPL Crystal Structure</b> Example of the $L_2A_nX_{3n+1}$ where n is the number of layers in between the planes of organic molecules. . . . .	44
4.2	<b>2DLP Perovskite Emission</b> A: PL of undoped 2DLP at different temperatures. B: Peak wavelength of BE emission red-shifting with decreasing T. . . . .	44
4.3	<b><math>C_2H_5PbBr_4 : Mn^{2+}</math> Sample Structure</b> A: Schematic of $C_2H_5PbBr_4$ with $Mn^{2+}$ dopants substituting for $Pb^{2+}$ . B: SEM image of $EA2PbBr_4:Mn^{2+}$ C: EDS mapping of $Mn^{2+}$ showing uniform dopant distribution within the SEM image.D: Powder X-ray diffraction (PXRD) of $C_2H_5PbBr_4$ with different $Mn^{2+}$ dopant concentrations. . . . .	47
4.4	<b>Room Temperature <math>C_2H_5PbBr_4 : Mn^{2+}</math> Photoluminescence</b> PL emission from the 2% and 7% Mn Doped 2DPL samples at room temperature. . . . .	49
4.5	<b>Temperature Dependent <math>C_2H_5PbBr_4 : Mn^{2+}</math> Photoluminescence</b> A/B: Temperature dependent PL Map for the 2% and 7% Mn Doped 2DLP Samples. C: PL Spectra of the same sample at 30 K showing the Band Edge emission (red), the self trapped exaction's (green), and the $Mn^{2+}$ emission (blue). D: In descending order $\rightarrow$ Movement of Band Edge (red) peak with temperature (Solid 2%, hollow 7%). Movement of 2% doped 2DLP STE (Green) followed by Mn(Blue). Then Movement of 10% doped 2DLP of STE followed by Mn. . . . .	50
4.6	<b>Temperature Dependent Mn Doped 2DLP TRPL and PL Intensity Trends</b> A: Graphic of energy transfer dynamics in the $C_2H_5PbBr_4 : Mn^{2+}$ 2DIP samples. B/C: TRPL spectra / extracted single exponential lifetimes with temperature. D/E/F: PL intensity trends of $C_2H_5PbBr_4 : Mn^{2+}$ 2DIP samples with temperature. (Solid 2%, hollow 7%) G/H: Plots fit with eq. 4.4 and eq. 4.6 to extract activation energies. . . . .	52
4.7	<b>Polarisation Dependent Spectroscopy</b> A: Left (Red) and right (Blue) circularly polarized emission from $Mn^{2+}$ dopants. B: Total polarisation of $Mn^{2+}$ emission as a function of temperature. . . . .	54
5.1	<b>Quantum Dot Dynamics</b> Cartoon depiction of an unfunctionalized Quantum Dots and the accompanying states on the Left and a depiction of the effect on surface potential of Quantum Dots. . . . .	57
5.2	<b>PQD Species Room Temperature Characteristics.</b> . . . . .	60

5.3	<b>PQD Species Room Temperature PL.</b> Upper Half: Displays the PQDs studied with their ligand combinations. The percentages inside the PQD – Ligand schematics are their optical quantum yields. A: Displays the PL spectra for each PQD species with the peaks offset to match their solid-state quantum yields. B: Displays the PDPL of each PQD species at room temperature. . . . .	62
5.4	<b>PQD Species Room Temperature TRPL</b> A: TRPL Spectra for the BZA-BA PQD solution (Grey) and solid state thin film (Red), with insets of each displayed. Solid PQD films are 1/2” by 1/2” and PQD solution is a 1 1/2” tall 10 $\mu$ L vial. B/C: Spectrally Resolved TRPL for BZA-BA/IPBZA-PAA solid state thin films. . . . .	64
5.5	<b>PQD Charge Transfer</b> A/B: TRPL curves with increasing PQD density for BZA-BA/IPBZA-PAA. C/D: Calculated charge transfer efficiencies as a function of PQD density. Right: Diagram of increasing PQD density. . . . .	65
5.6	<b>Temperature Dependent PL</b> A: BAZ-BA PL map. B: Spectra of BZA-BA at 150K, 90K and 30K. C/D Energy and linewidth dynamics respectively. E/F: Energy diagram at 300K/20K. . . . .	67
5.7	<b>Temperature Dependent PL &amp; TRPL</b> A/B/C: Temperature dependent PL maps of IPBZA-BA/BZA-PAA/IPBZA-PAA. D/E: Lifetime dynamics of the PPA/BA species. . . . .	69
5.8	<b>Cryogenic Free Charges</b> A: Temperature Dependent PL Map, B: Spectra of BAZ-BA at 150K, 90K and 30K, C/D: Wavelength/FWHM shift with temperature of BZA-BA. E/F: Energy level diagram of PQD at 300K/20K. . . . .	70
6.1	<b>PQD Correlations</b> A/B: TEM and UV-Solution images of 1:10 / 1:100 dilutions of the PQD stock. Image width is 300nm and 200nm respectively. C: PL/TRPL/Antibunching in-lab setup used to measure the PQD dilutions. D: PL of the bulk PQD ensemble verses the 1:100 dilution. E: correlation function of the 1:100 diluted spin coat samples. . . . .	80
A.1	<b>Measuring Material Transmission</b> A: Stock image from Perkin-Elmer. B: Optical image setup simplifying the basics of measuring a materials properties. C: Transmission curve of basic perovskite sample. . . . .	87
A.2	<b>Electronic Transitions in Semiconductor</b> Basic cartoon of photoexcitation, non radiative decay to band edge and recombination of the electron and hole resulting in emission of a photon. . . . .	89

---

A.3	<b>PL/TRPL Collection Setup</b> A: Typical PL/TRPL setup used in the collection of PL and TRPL data within this dissertation. B: Example of a MAPI PL spectra at room temperature, with the corresponding TRPL curve shown in C. . . . .	92
A.4	<b>Re-Absorption / Photo-active Stability / Spectral Selective TRPL</b> A: Typical edge collection setup to measure total internal reflection from the emission of the film. B: The results of the Gaussian fit from the resorption measurement on a MAPI film. C: Image from the lab of the AM1.5 photoexcitation setup. D: TOP PANEL) Displays the solar spectrum of the sun terrestrially, with MAPI PL shown in red. The blue line signifies the short-pass filter used before the sample and the long-pass filter used after the sample. BOTTOM PANEL) The PL intensity decay of a typical encapsulated MAPI sample. E: Displays the spectrally selective TRPL setup, with the data acquired from a typical PQD sample in F. . . . .	95

# List of Tables

2.1	<b>Perovskite Phases</b> Shows the typical phases of perovskites for the three common chemistries. . . . .	5
3.1	<b>Perovskite Thin Film Manifest:</b> List of perovskite samples used for this project with the thickness of $SiO_2$ thickness and APTES deposition method included. NA indicates that layer is not present in sample stack. Samples are all 1" by 1" . . . . .	20
3.2	<b>Non-Emissive Areas/PbI<sub>2</sub> Inclusions</b> Displays the average size of the $PbI_2$ Inclusions and total area they cover . . . . .	34
4.1	<b>Doping concentrations of Mn<sup>2+</sup></b> Relative to the sum of $Pb^{2+}$ and $Mn^{2+}$ ion content, of undoped and Mn-doped $EA_2PbBr_4$ with differing molar ratios of Mn/Pb. Measurement were made using ICP-OES. . .	48
4.2	<b>Activation Energies</b> Activation energies extracted from population fits. . . . .	53
6.1	<b>Sate of SPE Technologies [2]</b> Table listing the current values of SPE technologies including: Operation Temperature, Operation Wavelength, Photon Purity and Lifetime Limited Linewidth. . . . .	74
A.1	<b>Objectives Used:</b> This table lists the objectives used in this study.	93

# Abbreviations

**0-D** Zero Dimensional. xvi, 1, 84

**2-D** Two Dimensional. v, xvi, 1, 43, 83, 84

**2DLP** 2D Layered Perovskite. 43

**3-D** Three Dimensional. xvi, 1, 12

**AI** Absorption Intensity. 21

**AIAA** American Institute of Aeronautics and Astronautics. 12

**Cs** Cesium. 3

**EQE** External Quantum Efficiency. 10

**eV** Electron Volts. 9

**LED** Light Emitting Diode. xvi, 5, 10

**LLNL** Laurence Livermore National Lab. 2

**MA** Methylomonium:  $CH_3NH_3$ . 3

**MAPI** Methylammonium Lead Iodide,  $CH_3NH_3PbI_3$ . 5, 15

**Mn** Manganese. xvi, 2, 83, 84

**NASA** National Aeronautics and Space Administration. 1

**OMHP** Organo-Metalic Halide Perovskite. xvi, 1, 38, 82, 83

**PCE** Power Conversion Efficiency,  $CH_3NH_3PbI_3$ . 10, 12

**PQD** Perovskite Quantum Dot. xvi, 1, 2, 56, 72, 84

**PV** Photovoltaic. xvi, 1, 5, 10, 38, 82–84

**Si** Silicone. xvi, 1, 82

**SPE** Single Photon Emitter. 2

**T** Temperature. 4

**UCM** University of California, Merced. 1



# Abstract

Organo-Metalic Halide Perovskite (OMHP) materials have been under investigation in recent years due to their easy fabrication, high defect tolerances and high absorption coefficients across the visible spectrum making them ideal for integration into Photovoltaic (PV) [3–13] or Light Emitting Diodes (LED) [8, 14–22] devices. Perovskite photovoltaics have recently exceeded 25% in power conversion efficiencies swiftly approaching the best-reported silicon (Si) and III-V single-junction cells to date. [23] In addition, perovskite materials are easily synthesized through low-temperature solution-based methods, in contrast to Si, and III-V materials that require high temperatures and low defect densities to produce. [24] Other applications where OMHP have demonstrated promising results include photodetection [25], lasing [26, 27] and light emission [28, 29]. The emergence of low dimensional variants of OMHPs have further increased the versatility of this family of compounds. Two dimensional (2-D) perovskites offer increased exciton binding energies with increased moisture stability. In addition, zero-dimensional (0-D) perovskite quantum dots (PQDs) allow size-tunability of opto-electronic properties [30–32] and high photoluminescent quantum yields (80%) [20], which make them strong candidates for room temperature high fidelity single photon emission sources. [33, 34] This dissertation will focus on the authors work with space qualifying three dimensional (3-D) perovskite thin films, understanding energy transfer in Manganese (Mn) doped 2-D perovskites and the modification of Perovskite Quantum Dot PQD surfaces to increase PQD ensemble conductivity. In addition, it will highlight the importance on the non-destructive optical properties used, with a specific emphasis on the value of temperature dependent spectroscopy.

# Curriculum Vita

William Grant Delmas

wdelmas1995@gmail.com

---

## Education

**University of California, Merced**

5th Year, Ph.D. Candidate  
Department of Physics

*August 2017 - Present*

Overall GPA: 4.0

University of California, Merced  
Bachelors of Science, Physics  
School of Natural Sciences

*August 2013- May 2017*

Overall GPA: 3.2

## Research Experience

**University of California - Lab Fee Fellow**

University of California, Merced and Laurence Livermore National Lab

*April 2020 - April 2022*

- A two year award that facilitated collaboration between myself and staff scientists at Laurence Livermore National Laboratory (LLNL) to enhance the scope and impact of my dissertation project, with 50% of my time being spent on site at LLNL.
- During this two year period I made significant progress on my dissertation project, "Perovskite Quantum Dot Single Photon Emitters". While assisting on multiple feasibility projects at LLNL in fields ranging from Fiber-Based Environmental Gas Sensing using Raman Spectroscopy to 3D Laser-Induced Metal Printing.

**Graduate Summer Intern**  
NASA Glenn Research Center

*May 2019 - August 2019*

- Fabricate and space qualify Perovskite thin films for use in space-based photo-voltaics. Special emphasis was placed on the encapsulation of the films and its resistance to humidity. Sample quality was assessed using image processing and absorption spectroscopy.

**Graduate Summer Intern**  
NASA Langley Research Center

*May 2018 - August 2018*

- Chemically synthesize and test Boron Nitride Nanotube (BNNT) polymeric composites. Testing included, Scanning Electron Microscopy, Fourier Transform Infrared Spectroscopy and Thermogravimetric Analysis. Focus was placed on the BNNT-Polymeric piezoelectric response due to the hexagonal structure of the Boron Nitride structure. The bias induced response of the composite films was investigated showing promise for possible applications in energy harvesting.

## **Publications**

1. **Evaluation of hybrid perovskite prototypes after 10-month space flight on the International Space Station** (In-Progress) (First Author)
2. **Encapsulants and Barrier Layers for enhanced MAPbI<sub>3</sub> Durability for Applications in Space.** Timothy J Peshek, **William Delmas**, Kyle M Crowley, Kaitlyn T Vansant, Samuel Erickson, Jennifer Williams, Joseph M Luther, Jeremiah Mcnatt and Sayantani Ghosh, submitted.
3. **High Efficiency Luminescent Solar Concentrator based on Organometal Halide Perovskite Quantum Dots with Plasmon Enhancement.** Benaz Colabewala, Evan T. Vickers, Katerina Nikolaidou, Albert DiBenedetto, **William G. Delmas**, Jin Z. Zhang and Sayantani Ghosh, Adv. Optical Mater. 2021, 2100754.
4. **”Systematic Study of Space-Grade Encapsulants and Barrier Layers for durability of MAPbI<sub>3</sub> ,”** Timothy J. Peshek, **William Delmas** , Meghan Bush, Deyaneira Torres-Gonzalez, Shireen Khayat, Sayantani Ghosh, Jennifer W. Williams, and Lyndsey McMillon-Brown, Member, 2020 47th IEEE Photo-voltaic Specialists Conference (PVSC), 2020, pp. 1121-1123
5. **Low temperature energy transfer via self-trapped excitons in Mn-doped 2D organic halide perovskites.** Som Sarang, **William G. Delmas** , Sara Bonabi Naghadeh, Vivienne Cherrette, Jin Z. Zhang, and Sayantani Ghosh, J. Phys. Chem. Lett. 2020, 11, 10368–10374

6. **Modulating charge carrier dynamics and transfer via surface modification in organo-metallic halide perovskite quantum dots .** William G. Delmas , Evan T. Vickers, Albert C. DiBenedetto, Calista Lum, Isaak N. Hernandez, Jin Z, Zhang, and Sayantani Ghosh, J. Phys. Chem. Lett. 11, 7886, (2020).
7. **Enhancing Charge Carrier Delocalization in Perovskite Quantum Dot Solids with Energetically Aligned Conjugated Capping Ligands.** Evan Vickers, Emily E. Enlow, William Delmas , Albert DiBenedetto, Ashraf Chowdhury, Behzad Bahrami, Benjamin Dreskin, Thomas Graham, Isaak Hernandez, Sayantani Ghosh, Qiquan Qiao, Jin Zhang. ACS Energy Lett. 5, 817 (2020).
8. **Electromagnetic coupling to centimeter-scale mechanical membrane resonators via RF cylindrical cavities.** Martinez, L. A., Castelli, A. R., Delmas, W., Sharping, J. E., 38; Chiao, R. (2016).New Journal of Physics, 18 (11), 113015.

## Conference Presentations

1. **Self-Trapped Exciton Assisted Energy Transfer from the Band Edge to Mn Dopant in Mn<sup>2+</sup>-Doped 2D Organometal Halide Perovskites.** @ American Physical Society March Meeting 2021
2. **Enhancing Charge Carrier Delocalization in Perovskite Quantum Dot Solids with Energetically Aligned Conjugated Capping Ligands.** @ Material Research Society Spring Meeting 2021

## Professional Trainings

### Hands on Photovoltaic Experience (HOPE)

National Renewable Energy Laboratory

*July 2019*

Golden, CO

- A week long intensive that focused on the theory, fabrication and characterization of photovoltaics of all types. Specific emphasis was placed on triple cation perovskite solar cell fabrication for tandem cell applications.

### Interdisciplinary Computational Graduate Education Program *Jan 2019 - May 2019*

NSF National Research Training

University of California, Merced

- Training included introductions to languages and computational tools such as Bash, Python, Matlab, Machine Learning, custom library generation and Monte Carlo simulations.

- The training promoted the formation of interdisciplinary groups to generate and execute a collaborate research plan. Our project scraped twitter for posts about mass shootings to map the length of public discourse after their occurrence.

# Acknowledgements

The author acknowledges the Space Technology Mission Directorate's Center Innovation Fund and Early Career Innovation Programs for support of this work. The author acknowledges the Materials for Optoelectronic Research and Education (MORE) Center at Case Western Reserve University, and the Ohio Third Frontier program for establishing this core facility in 2010. The author acknowledges the MISSE-X contract to Alpha Space Test and Research Alliance, LLC. The author acknowledges the NASA MIRO award NNX15AQ01A.

# Chapter 1

## Introduction

The class of materials known as Organo-Metalic Halide Perovskite OMHP are optical direct bandgap semiconductors, unlike the naturally occurring perovskites that were first discovered in the 19th century. [35] This dissertation summarizes the authors work at the University of California, Merced UCM and is comprised of research into OMHP while varying their dimensionality from 3-D thin-film perovskites, 2-D Ruddlesden-Popper perovskite flakes, 0-D PQD. The progression of this work will follow inversely with perovskite dimensionality, namely, it will start with 3-D perovskites and move downward towards 2-D and then finally to 0-D Perovskites. Each chapter will discuss a particular dimensionality of perovskites and the effect that dimensionality has on basic perovskite optoelectronic properties.

**Chapter Two** of this dissertation will examine the basics of halide perovskites, focusing on the contribution of chemical composition to crystal structure and bandgap. It will begin with a summary of dimensionally invariant properties, to provide a good foundation of the fundamental characteristics, and to emphasize the effects changing dimensionality has on halide perovskites.

**Chapter Three** will introduce the most well-studied category, 3-D thin-film OMHP. Thin-film perovskites are well known for their strong performance as high-efficiency PV, surpassing conventional Si in only 15 years of study. This section will include the authors work on similar films at the National Aeronautics and Space Administration NASA Glenn research center during a summer internship in 2019. This work there focused on the fabrication of thin-film perovskites for applications in space-based PV. This work was later expanded on in further collaborations between UCM and NASA Glenn, where a thin-film perovskite sample the author previously fabricated was flown to the International Space Station and exposed to space for ten months. Much of Chapter three will focus on the post-flight analysis of this sample and its implications for the feasibility of space-based perovskite photovoltaics.

**Chapter Four** of the dissertation will focus on 2-D Ruddlesden-Popper perovskite flakes. This specific class of perovskite possesses a large organic molecule in the center

of its cubic structure, pushing the perovskite layers apart, inducing quantum confinement in one direction. Along with the effects of this mono-directional confinement, chapter three will explore the authors work with Mn doped 2-D perovskites. Doping 2-D perovskites with Mn facilitates access to optical transitions within the Mn itself through optical excitation of the host perovskite. Study of this Mn-doped 2-D perovskite revealed interesting charge transfer dynamics and is a strong candidate for a white light-emitting diode.

**Chapter Five** will focus on the lowest dimensionality of perovskites, PQD. In this regime, quantum confinement dominates the optical and electronic properties, along with new surface effects, as the surface area to volume ratio increases. This chapter will describe the effect organic molecules (ligands) have when used to functionalize the surfaces of the PQDs, and how a systematic study can allow tuning the PQD properties through rationally designed ligands.

**Chapter Six** will focus on single PQDs. This work is part of the authors University of California-Lab Fee Graduate Fellowship, done in collaboration with Lawrence Livermore National Lab LLNL. It focuses on studying isolated, single PQDs to probe their viability as single-photon emitters SPE.

## 1.1 Motivation and Purpose

The purpose of this work in halide perovskites is due to their unique material properties leading to a wide variety of possible applications, specifically in photovoltaics and renewable energy. This dissertation will highlight the varied applications of perovskites across their dimensionalities. This will be in contrast to the investigative techniques used in these studies, that remain standard. The non-destructive micro optical techniques used in this work are infrequently utilized in the perovskite field. **The goal of this dissertation is to highlight the versatility of these non-destructive microscopy and spectroscopy techniques and the novel physics that they reveal within this class of material.** This work is comprised of both physics and material science allowing the application of in-depth, physics-based, non-linear optical analysis to a commonly studied material to tease out the fundamental physics within, allowing identification of new avenues for advancements in sample design and implementation.



## Chapter 2

# Optical, Electrical and Chemical Properties of Perovskite

Perovskites are a naturally occurring compound, with the crystal structure  $ABX_3$ , where: A is a cation that makes up the center of a cubic, tetragonal or orthorhombic structure, B is a metal and C is an anion. It derived its name because the first material discovered to have this structure was calcium titanate ( $CaTiO_3$ ).

### 2.1 Crystal Structure

Due to the chemical makeup of the naturally occurring perovskite, a perfect cubic atomic lattice was assumed after its initial discovery but once x-ray diffraction technology progressed it was later shown to have a tetragonal lattice, displaying 1% stretching along the tetrad axis from the originally assumed perfect cubic. [36] Fig. 2.1 shows the standard  $ABX_3$  crystal structure.

As previously discussed these naturally occurring perovskites gave way to synthetically manufactured perovskites with semiconductor properties in the early 21<sup>st</sup> century. These new semiconducting perovskites maintained the  $ABX_3$  crystal structure but with extra restrictions, shown in Fig. 2.1. The A site consists of three different options, Methylomonium ( $CH_3NH_3$ ) (MA), Formadimium ( $CH_5N_2$ ) or Cesium (Cs). The B site is a metal typically lead (Pb) but can be substituted for Tin (Sn). The C site can consist of 3 different atoms: Iodide (I), Chloride (Cl), Bromide (Br). This class of perovskites has been dubbed halide perovskites due to the C site atoms all being halides. This structure is a simple centered cubic structure with the A site at the center and the corner sites being the lead iodide octahedral.

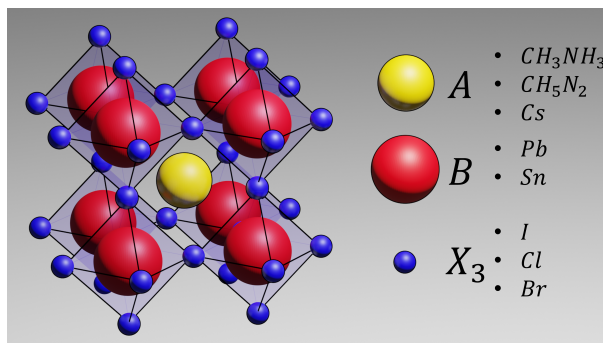


Figure 2.1: **Halide Perovskite Crystal Structure.**  $ABX_3$  crystal structure where the A site cation can be the organic molecules methylammonium ( $CH_3NH_3$ ), Formadimium ( $CH_5N_2$ ) or Cesium ( $Cs$ ). The B site metal can be lead ( $Pb$ ) or tin ( $Sn$ ). The X site halides can be iodide ( $I$ ), chloride ( $Cl$ ) or bromide ( $Br$ ).

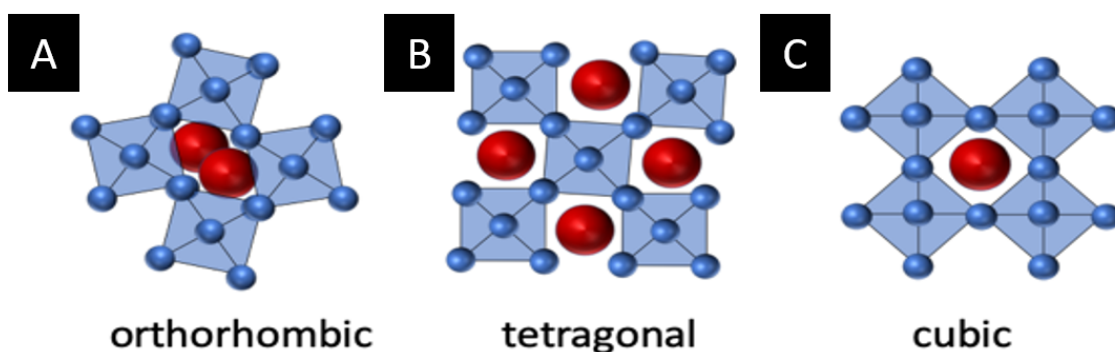


Figure 2.2: **Structural Phase Dynamics** A: Orthorhombic Phase, B: Tetragonal, C: Cubic Phase

### 2.1.1 Structural Phase Dynamics

The structural phase of halide perovskites is temperature-dependent and consists of three different configurations: cubic, tetragonal and orthorhombic. When in the cubic structure the three lattice vectors  $x_1, x_2$ , and  $x_3$  are equal. A tetragonal structure is when two of the three lattice vectors are equal while the third is different. An orthorhombic structure occurs when all three lattice vectors are different from one another. These three stable phases are shown in Fig. 2.2.

The stable temperature of these phases is determined by the crystal's phase diagram which is specific to the chemical makeup. Table 2.1 displays the typical temperature  $T$  ranges the crystal structures are stable for some common perovskites.

Chemical Formula	Orthorombic	Tetroagonal	Cubic	Ref
$CH_3NH_3PbI_3$	$T < 162.2K$	$162.2 < T < 327.4K$	$T > 327.4K$	[37]
$CH_3NH_3PbBr_3$	$T < 144.5K$	$149.5 < T < 236.9K$	$T > 236.9K$	[38]
$CH_3NH_3PbCl_3$	$T < 172.9K$	$172.9 < T < 179.8K$	$T > 179.8K$	[38]

Table 2.1: **Perovskite Phases** Shows the typical phases of perovskites for the three common chemistries.

## 2.2 Chemical Stability

The most significant barrier to perovskite implementation is its chemical instability to:

1. Moisture
2. Oxygen
3. Solar Spectrum Illumination
4. Thermal Stress
5. Mechanical Stress

Other degradation mechanisms do exist when perovskite films are incorporated into PV or LED however the majority of the research in this dissertation focuses on the absorber/emitter layers of these devices thus these additional degradation pathways will not be mentioned within this document.

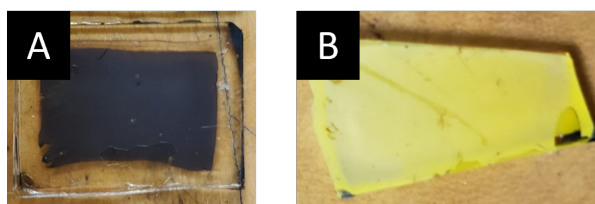


Figure 2.3: **Binary Perovskite Degradation.** A shows a MAPI perovskite film after synthesis. Image 1" by 1". B shows a similarly synthesised film that has fully degraded into  $PbI_2$ , evidenced by its change in color from black to yellow. Image 1/2" by 1/2"

Starting with the most studied chemical composition of perovskites, methylammonium lead iodide  $CH_3NH_3PbI_3$ , MAPI, both theoretical [25, 39] and experimental [25, 40] studies have shown that MAPI degrades into its binary components, as

shown in equation 2.1. The exact pathways of degradation vary based on the chemical composition but all have similar pathways to the MAPI film.

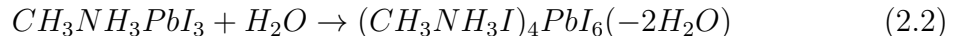


This degradation of MAPI into its binary components has even been seen in an inert ( $N_2$ ) environment without any stimuli. [41] The reason for this unprompted degradation is speculated to be because of the negative formation energy of the MAPI structure. [39] This means that the reaction is exothermic, the amount of energy it takes to break bonds is less than the amount of energy that is released when making the bonds.

This binary decomposition is seen in all dimensionalities of  $XPbI_3$  samples, this is typically seen as a visual change to the  $PbI_2$  crystal structure with a characteristic yellow color, as shown in Fig. 2.3

### 2.2.1 Moisture

Most materials will react with oxygen and perovskites are no exception. Experimental results suggest that the incorporation of the moisture molecule ( $H_2O$ ) into the MAPI lattice causes the formation of an intermediate MAPI hydrate shown in equation 2.2. [41]

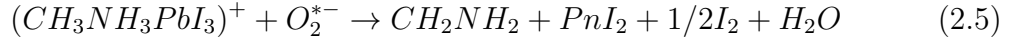
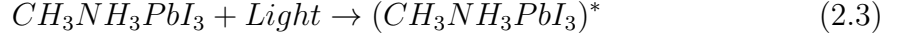


This hydrated intermediate phase has been shown reversible at a relative humidity of less than 50% for the first 48 hours upon drying the film out. However, beyond this, the reaction does not appear reversible and results in the formation of a hydrated  $PbI_2$  phase. [42] The initial formation of this hydrate forms strong hydrogen bonds with the organic cations in the crystal weakening the bonds between the  $PbI_6$  octahedral making the crystal more prone to degradation from the other stimuli. [41]

### 2.2.2 Oxygen

Perovskite films have shown a robustness to oxygen ( $O_2$ ) exposure in the dark for extended periods [42, 43] however they have shown significant instability when exposed to oxygen while illuminated. [44] Investigations into this phenomenon have also revealed that degradation rates correlate with the number of iodide vacancies within the film. [45] Bryant and group speculated that the oxygen uses the iodide vacancies as inoculation points and pathways through the film due to molecular oxygen being similar to volume to iodide. Once within the crystal, the molecular oxygen ( $O_2$ ) acts as an electron donor and in the presence of light photo-excited electrons are generated that transfer to the  $O_2$  creating a super-oxide. This is shown in equation 2.3 and 2.4

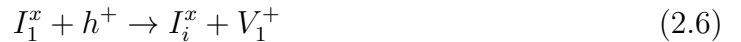
with the creation of a photo-excited MAPI followed by the donation of that electron to the molecular oxygen<sup>1</sup>. [46]



This super-oxide causes an acid-base reaction with the acidic A site cation deprotonating it and causing the formation of a gaseous Aminomethyl ( $CH_2NH_2$ ), lead iodide, lone iodide, and water, shown in equation 2.5. [47] The water generated from this reaction can then go on to further degrade the perovskite.

### 2.2.3 Solar Spectrum Illumination

Perovskite thin films under light illumination have shown evidence of light-induced halide movement throughout the perovskite film. [48] Christians and group showed that in perovskite films iodide separates from the illumination sites causing defects in the crystal in the form of iodide vacancies. The movement of this iodide is proposed to be caused by the oxidation of the iodide ion ( $I_1^x$ ) by the positively charged hole ( $h^+$ ) generated under photo-excitation. This then results in the formation of a neutral iodide ( $I_i^x$ ) and an iodide vacancy ( $V_1^+$ ).



This process is shown in equation 2.6 and generates the pathway for halide diffusion because the neutral iodide is smaller in volume than the iodide vacancy, allowing diffusion from its lattice site. This motion of constituent atoms to the perovskite structure is also seen with the cation centers, displaying the ability to separate and diffuse through the lattice causing more vacancies.

### 2.2.4 Thermal Stress

To discuss the thermal stability of the perovskite crystal we need to discuss the phase stability of the perovskite crystal. [49] We will start by discussing the stable structure of perovskites with the Goldschmidt tolerance factor  $t$ : shown in equation 2.7

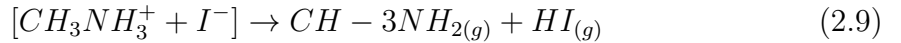
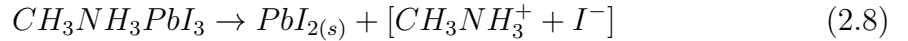
$$t = \frac{r_A + r_X}{\sqrt{2}(r_B + r_X)} \quad (2.7)$$

---

<sup>1</sup>\* symbolises a photo-excited species

In this equation  $r_A$  is the radius of the A-site cation in the crystal,  $r_B$  is the radius of the B-site cation, and  $r_x$  is the X-site anion. Filip et al. found through a series of data mining and predictive modeling that a perovskite crystal forms when  $0.71 > t > 1$ . [50] This suggests the most thermally (structurally) stable film is  $CH_3NH_3PbI_3$  with a tolerance factor of  $t=0.91$ , but the use of a Cs/FA results in a tolerance factor below/above the stable range.

Early studies of perovskite stability that heating at 85C produced  $PbI_2$  inclusions in the film within the first 24 hours of heating in ambient air, oxygen, and inert  $N_2$ . [51] Thermo-Gravimetric Analysis has shown that  $CH_3NH_3PbI_3$  films degrade into 3 different components, as shown in equation 2.8, 2.9



The  $CH_3NH_3$  structure breaks into a solid  $PbI_2$  component and an excess iodide with the A-site cation as shown in equation 2.8. This A site component with the extra iodide then turns into two gaseous components methylamine ( $CH_3NH_2$ ) and hydriodic acid (HI) both in their gaseous states. The reason for this breakdown is directly correlated to the structure dynamics. In the  $CH_3NH_3PbI_3$  crystal the lateral PbI bond is 1.7 angstroms while the horizontal bonds are 1.2 angstroms. During thermal excitation of the lattice, the increased vibration breaks the longer PbI bonds causing the degradation process laid out earlier.

## 2.2.5 Mechanical Stress

The mechanical stress in the perovskite crystal can cause additional disorder to the system and increases the rate of degradation from the 4 other sources mentioned above. Zhao and group found that applying both a tensile and compressive strain to the film decreases its stability. [52] They speculated that the strain weakened the bonds in the crystal increasing the probability of the other degradation routes, which all depend on the strength of the bonds, to begin with.

## 2.3 Band Contributions

The most exciting properties such as chemical tunability and defect tolerance of perovskites arise from their crystal structure discussed above and the effect that crystal structure has on the energetic bands for the perovskite semiconductors. These energetic bands arise from the overlap of energy potentials within the crystal due to the constituent atoms both filled and unfilled atomic orbitals. It has been shown that the A site cations contribute little to the band structure [53] and thus we will start

---

with the B site metals of Sn and Pb. The Sn and Pb atoms have two electrons of six available in the 5p and 6p along with fully occupied 5s and 6s orbitals respectively as shown in Fig. 2.4 A. The halide constituents of the crystal contributions are the 5p, 4p, and 3p for I, Br, and Cl, as shown in Fig. 2.4 B. These orbitals contain 5 of the 6 electrons leaving one electron unpaired. When these atomic orbitals overlap within the perovskite crystal they form the electronic bands of perovskite. Density functional theory calculations show that the top of the valence band of OMHP comes from the hybridization of the 3p/4p/5p halide states with the occupied metal 5s/6s states. While the conduction band of perovskites is formed by the unoccupied metal 5p and 6p states. [53]

## 2.4 Chemical Tunability

The chemical tunability of perovskites comes from changing the constituents of the perovskite crystal structure, this change in structure can lead to:

1. Changes in the band gap
2. Increased light absorption
3. Increased stability

### 2.4.1 Changes in Band Gap

The chemical tunability of the constituent elements also results in a change in the band gap of the perovskite. This bandgap change is directly linked to the energy levels of the metals and halides used in the perovskite. For example, in a  $APbCl_3$  perovskite, the Cl atom with the 3p contribution to the valence band is the lowest energetically while the Pb 6p contribution to the conduction band is the highest energetically, which results in the largest perovskite bandgap, around 2.6 electron volts (eV). While a  $ASnI_3$  perovskite has the highest valence band contribution of 5p and the lowest conduction band contribution of 5p results in the lowest perovskite bandgap of 1.23 eV. [54] Mixing of the perovskite constituents allows tunability between these two extremes of 1.23 eV to 2.6 eV. For example, a  $CH_3NH_3PbI_{0.6}BR_{0.4}$  perovskite has a band gap of 2.0 eV, increasing the bromide content will take it closer to the pure bromide band gap of 2.2 eV, while increasing iodide will take the band gap towards the pure iodide energy of 1.59 eV. All these chemistries and resulting bandgap energies are shown in Fig. 2.4 D. [55]

### 2.4.2 Increased Light Absorption

The use of organic cation centers such as methylammonium and formamidinium increases the photon absorption efficiency of the perovskite crystal. This translates to a total increase in the Power Conversion Efficiency PCE of perovskite photovoltaics and the External Quantum Efficiency EQE of LEDs.

### 2.4.3 Increased Stability

The incorporation of the inorganic Cs component into the perovskite structure has been shown to significantly increase its stability. The chemical degradation of the perovskite typically reacts with the more volatile organic centers like methylammonium and formamidinium. Dae Woo et al. found that the incorporation of Cs in perovskite doubles the thermal stability of the film at 100 C [56] while Lee *et al.* showed the incorporation of the Cs also increases the photo and moisture stability of the perovskite. [57]

## 2.5 Defect Tolerance

One of the reasons perovskites have shown great potential as active material in PV and LED is that it is defect tolerant, that is it maintains their inherent properties despite, dangling bonds, vacancies, and impurities. The reason for this is because the defects just listed all create shallow energy levels within the perovskite band structure [58], shown as the red lines in Fig. 2.4 E. A typical semiconductor has defect energy levels that exist mid-band gap and therefore act as recombination centers limiting their effectiveness in PV and LED



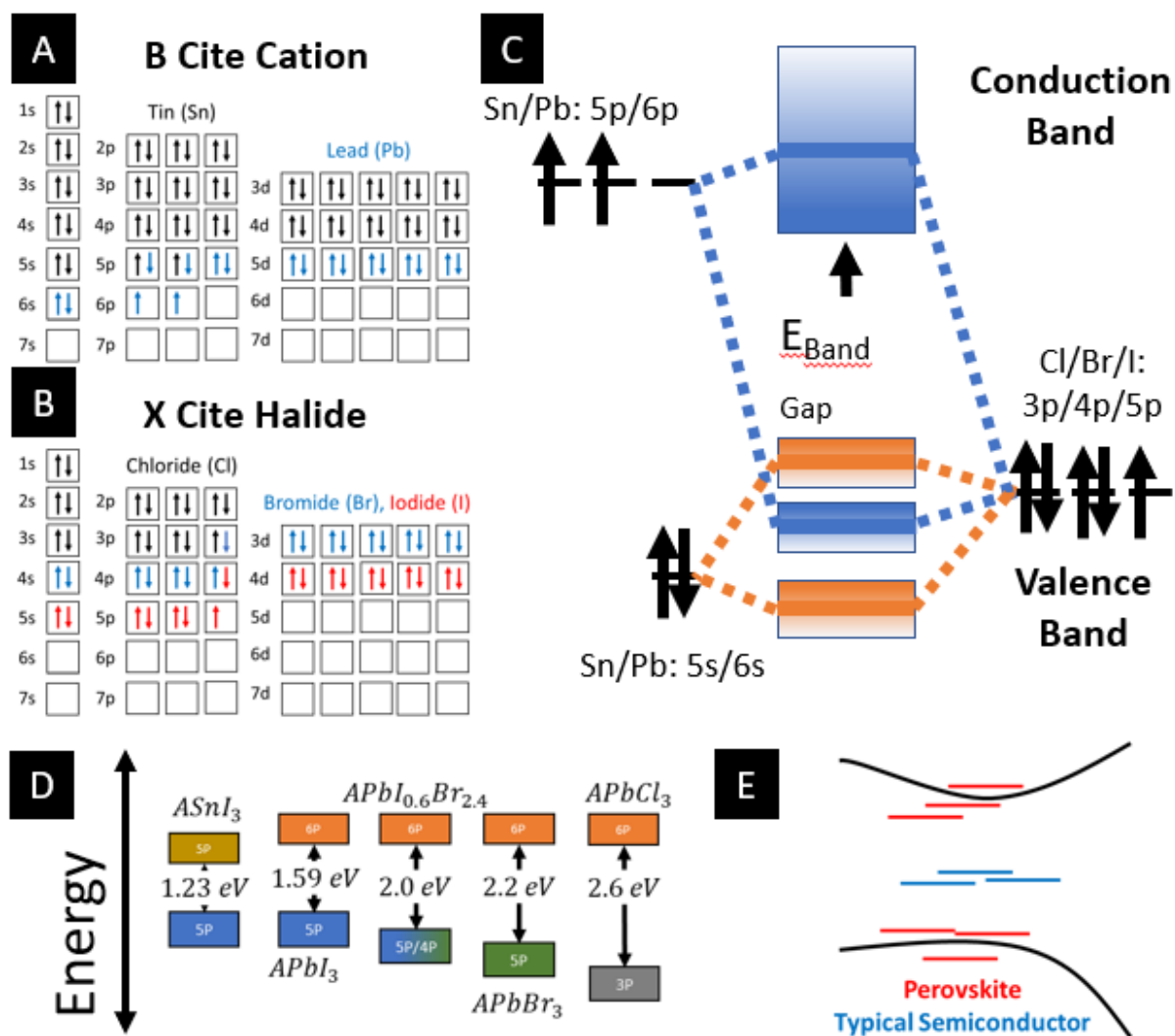


Figure 2.4: **Halide Perovskite Band Contributions.** A/B: shows the typical orbital structure of the Sn, Pb / Cl, Br, I constituents of the perovskite crystal structure. C: Shows how the overlapping atomic orbitals form the perovskite band gap. D: Is the typical bandgap for perovskite crystals with varying chemistries.

# Chapter 3

## 3-D Thin Film Perovskites for Space-Based Photovoltaics

Halide perovskite 3-D thin films are the most studied dimensionality of perovskites due to their strong applicability for the absorber layer in solar cells, with over 10,000 publications a year since 2017. Their implementation in photovoltaic devices in early 2012 saw an initial power conversion efficiency (PCE) of 13% that has nearly linearly increased in the following years to 25.7% in 2021. [23] The success of perovskite thin films as a photovoltaic absorber is a direct result of its chemical tunability, defect tolerance, and the thin film's unique property of low-temperature solution based synthesis. Due to these unique properties perovskites have attracted attention as possible space-based photovoltaics, both in the ground-to-space launch and in-space-synthesis regimes. With the new initiatives of a permanent presence in space and on the lunar surface, efficient and lightweight power sources are required. To this end, Perovskite thin-film photovoltaics offer strong single-junction power conversion efficiencies (PCE) of up to 25.5% [59–61]. In addition, the high specific power (power to weight ratio) of perovskites, due to their lightweight nature [62] offers additional benefits over conventional space-based photovoltaics. However, testing of perovskites in space has been limited to just hours to minutes within the space environment. [63–65]

**To make perovskites in space a reality**, perovskite solar cells have to be evaluated by American Institute of Aeronautics and Astronautics AIAA S-11 photovoltaic standards to be used in ground to space regime. That is the cells are fabricated terrestrially and then flown to space and deployed, similar to all space-based photovoltaics to date. After perovskites have been shown to meet these standards, an extended test of perovskite's robusticity in the space environment is needed. This chapter will focus on our efforts to space qualify  $CH_3NH_3PbI_3$  through:

1. Humidity testing of encapsulated perovskite thin films to space qualify the films according to AIAA S-11 photovoltaic standards.

- 
2. Fabrication, pre and post-flight testing of an encapsulated perovskite thin film for a 10-month space flight on the ISS

## 3.1 Thin Film Basics

The optoelectronic and chemical basics of the perovskites' crystal structure covered in Chapter 2 do not vary when applied to perovskite thin films. The additional properties of thin-film perovskites are due to the grain boundaries that exist in these thin films as a result of their synthesis. This section will focus on the synthesis method used in this work and the effect these grain boundaries have on the film's optoelectronic properties.

### 3.1.1 Perovskite Thin Film Synthesis

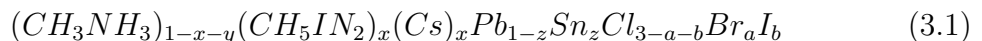
One of the most attractive advantages of thin-film perovskites is their easy low temperature ( $< 120C$ ) synthesis. This is due to perovskite's low formation energies, Young's modulus, and high thermal expansion coefficients. [66] These properties have led to a wide variety of synthesis methods that can be divided into one and two-step methods. One-step methods often employ a singular or bi-solvent method of Dimethylformamide (DMF) and/or Dimethyl sulfoxide (DMSO) with the binary perovskite components of AX and  $BX_2$  dissolved within. While two-step methods often entail the sequential deposition of one solvent containing dissolved with  $BX_2$  followed by the other solvent containing the dissolved AX.

The conventional spin coating method was first successfully used in 2009 with the binary constituents ( $PbI_2$ ) and ( $CH_3NH_3I$ ) dissolved in DMF, by Kojima and group with the first use of perovskites in a photochemical cell. [67] The film deposited was the most commonly studied chemistry of  $CH_3NH_3PbI_3$ , showing an external quantum efficiency of 65% and PCE of 3.8%. This first use of this method formed nano-crystalline grains of roughly 10 nm in size. Multiple variations of this method were developed in the 13 years to follow including the development of mixed halide devices and sequential deposition. A mixed halide film can be formed with this method through variations of the precursor solutions, also called ink. For example, our group achieves mixed Cl/I films through spin coating using an ink of a DMF/DMSO precursor solution with  $CH_3NH_3PbI$  and  $PbCl_2$ . This mixture forms a mixed Cl/I film formula,  $CH_3NH_3PbCl_{x-3}I_x$ , where the I content x, is controlled by the ratio (by weight) of the  $CH_3NH_3PbI$  and  $PbCl_2$  constituents.

Two-step perovskite deposition was developed by Xiao and group where they sequentially deposited a layer of  $CH_3NH_3I$  atop an already spun coat layer of  $PbI_2$  dissolved in DMF. [68] The resulting films made grain sizes of hundreds of nm in diameter, and solar cells of over 14% PCE, 10% higher than the initial trials of

single-step synthesis, only 5 years before. Another two-step method developed is the Anti-Solvent or Solvent Engineering method, where a single ink is used with all the requisite precursor components and an additional solvent is spun atop the un-annealed precursor solution driving away from the precursors solvent and speeding up nucleation. This method was pioneered by Jeon and group in 2014 with the use of a precursor ink of  $CH_3NH_3I$ ,  $CH_3NH_3Br$ ,  $PbI_2$  and  $PbBr_2$  dissolved in gamma-Butyrolactone (GBL) and DMSO in a 7:3 ratio by volume. After spin-coating deposition of the ink through spin coating, an antisolvent of toluene was deposited on the film. [69] It resulted in a film with grain sizes in the 100's of nm and a PCE of 16.5% when Incorporated into a full device stack.

This solvent engineering method led to the development of "Kitchen Sink" perovskites also known as mixed cation/halide perovskites with the chemical formulas shown in equation 3.1.



The formula has the additional restrictions of  $0 < x + y > 1$ ,  $0 < z > 1$  and  $0 < a + b > 3$ . These mixed halide perovskites have shown the highest efficiencies to date, between 23% to 25.4 %. [23] The anti-solvent method is required for these complex structures due to the disordered nature of the kitchen sink perovskites the structure must nucleate quickly to form a stable film. These perovskite thin films have only been successfully achieved using two-step synthesis methods.

### 3.1.2 Perovskite Grains

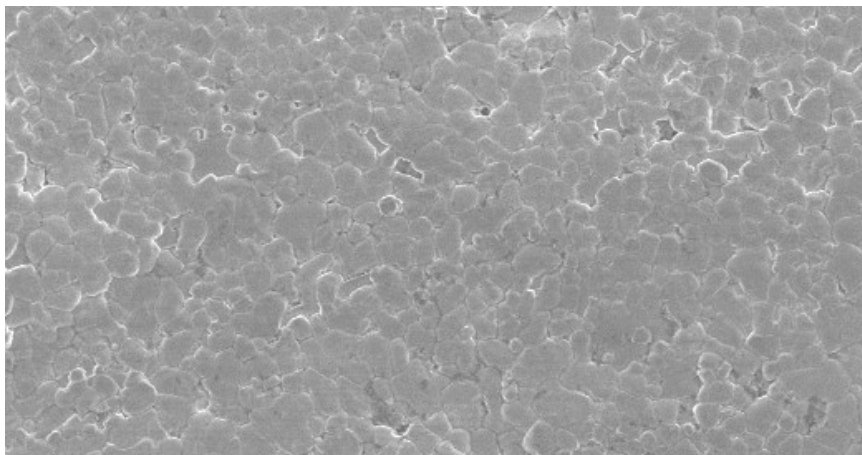


Figure 3.1: **Perovskite Grains:** SEM of a perovskite thin film. Total image width is 30  $\mu\text{m}$ .

---

Taking a basic MAPI film during synthesis, the ink is deposited onto the substrate and the constituents,  $CH_3NH_3I$  and  $PbI_2$ , are suspended in the solvent ready to form the seeds of the perovskite grains. When the film is placed onto the hotplate to anneal, the solvent is driven off the sample and those constituents nucleate across the sample forming grains. Example of perovskite grains is shown in Fig. 3.1. The degrees of freedom for this process are as follows:

1. Annealing Temperature
2. Solvent
3. Ratio of Constituents

By manipulating these factors it is possible to manipulate the size of the perovskite grains to a certain degree. For example, it is important to minimize the empty spaces between the grains as that can limit charge transport within a device due to difficulty with mobile electrons jumping the gap. This suggests that larger grain sizes are better, however, large grain sizes have been linked to smaller lifetimes. [70] It becomes a balancing act based on what application the film is being used for.

## 3.2 Encapsulation of Perovskite films to Meet AIAA S-11 Photovoltaic Standards

For solar cells to be certified for in-space operation they have to pass AIAA standards. The standards can be outlined as follows:

1. Expose the sample to  $95 \pm 4\%$  relative humidity at  $45^\circ\text{C}$  for 21 days
2.  $80^\circ\text{C}$  bake-out for 24 hours in a vacuum of  $10^{-5}$  Torr
3. Thermal cycling in humid and  $N_2$  environment to temperatures expected on mission for 25% of expected mission duration

To begin evaluating perovskites as possible photovoltaics they must meet these standards. The most daunting requirement for perovskites is the first, due to perovskite's known instability to moisture and oxygen. The reason for the moisture tolerant requirement is due to the weeks-long wait on the tarmac in Florida that electronics often undergo pre-launch into space. The proposed mechanism to counteract this moisture-induced degradation is encapsulating the perovskite film with a space-grade encapsulant. This encapsulant, Dow - DC 93-500 is a silicone elastomer and when dried, is transmissive across the entire visible spectrum. To determine its effectiveness we studied encapsulated perovskite thin films ( $CH_3NH_3PbI_3$ ) inside a

95% relative humidity chamber for 300+ hours. The quality of these films will be measured by routinely removing the films from the humidity chamber to perform transmission measurements. The diffusion of water through the encapsulant and additional barrier layers will be quantified by image analysis of the perovskite as it turns from grey to yellow as it decays into  $PbI_2$ .

### 3.2.1 Materials and Synthesis<sup>1</sup>

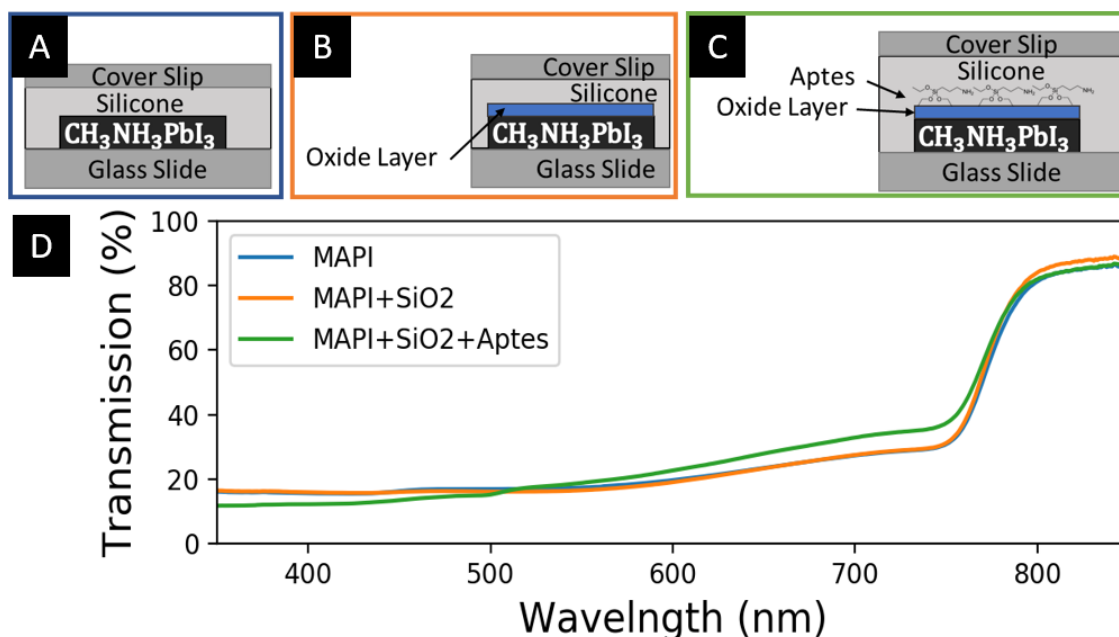


Figure 3.2: **Perovskite Structures Studied** A: Basic perovskite encapsulated with glass. B: Perovskite covered in  $SiO_2$  between 50 nm and 150 nm. C: Same structure as B but with the addition of a 2 nm to 4 nm of APTES ligands. D: Transmission spectra of the three structures after synthesis. Inset: Structure of the APTES ligand.

All sample structures in this study are shown in Fig. 3.2. The first structure (Bordered in Blue and shown in Fig. 3.2 A) is the basic perovskite thin-film structure fabricated atop a 1" x 1" area, 1mm thickness, silicate slide, encapsulated by our space-grade encapsulant DC-93-500 and capped with an identical glass slide. The second structure (bordered in orange) shown in Fig. 3.2 B) is identical to A) but with a 50 nm layer of  $SiO_2$  between the perovskite and DC-93-500 layer. The Third structure (Bordered in Green) is identical to B) but the  $SiO_2$  is coated in a self-

<sup>1</sup>All synthesis of samples was performed at CASE Western Reserve University in the MORE lab facility under the supervision and assistance of the lab director Dr. Ina Martin.

assembled layer of APTES<sup>2</sup>. The transmission curve shown in Fig. 3.2 D) shows the small differences that exist in the different device structures.

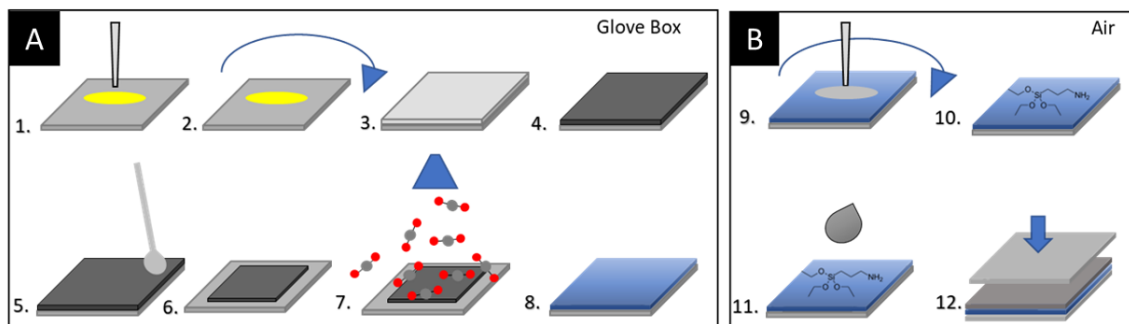


Figure 3.3: **Perovskite Device Synthesis** A: Perovskite device structure synthesis within glove box. B: Perovskite device structure synthesis in ambient conditions within a glove box.

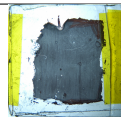
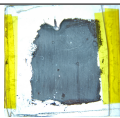
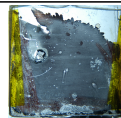
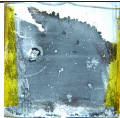
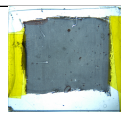
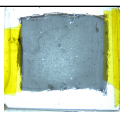
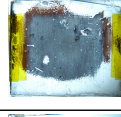
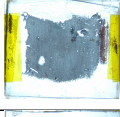
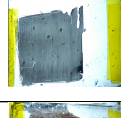
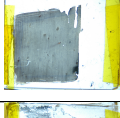
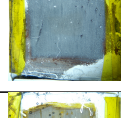
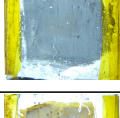
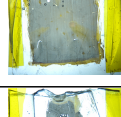
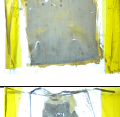


All sample structures were fabricated at Case Western Reserve University in the MORE Lab User Facility. The perovskite ink was purchased from Sigma Aldrich (Part#: Discontinued) and consisted of  $CH_3NH_3I$  and  $PbI_2$  suspended into DMF in the ratio 1:1:1 respectively. The APTES solution was purchased from Sigma Aldrich (Part#: 440140) and consists of 99%  $H_2N(CH_2)_3Si(OC_2H_5)_3$ . The encapsulant DC-93-500 is a silicone elastomer purchased from DOW CORNING prepared by mixing the precursor with the hardening agent in a 10:1 ratio respectively, stirring thoroughly, and then degassing at 40C in a vacuum oven. The following synthesis procedure follows the steps in Fig. 3.3 A and B.

1. Drop cast  $30\mu l$  of ink onto a 1" by 1" glass slide
2. Spin at 2000 RPM for 90 seconds
3. This results in a yellow-ish film atop the glass slide
4. Anneal on a hotplate at 100 Celsius for 60 minutes. The yellow film transitions to black seconds after being placed onto the hotplate
5. Dip a q-tip in DMF solvent and 'erase' the edges of the perovskite
6. Cut edges will allow a strong seal of the encapsulant
7. Using an Angstrom Instruments Chemical Vapor Deposition system, a 50nm to 150 nm of  $SiO_2$  was deposited atop the edged perovskite

<sup>2</sup>(3-Aminopropyl)triethoxysilane (APTES) is an aminosilane that is often employed in water-proofing a wide variety of surfaces.

8. After  $SiO_2$  deposition the films are removed from a glove box to a fume-hood
9. Drop cast 2ml of the APTES-Solvent while spinning at 200 RPM for 5 seconds then ramping up to 2000 RPM for 30 seconds
10. This deposits a 2nm - 4nm (3 to 7 layers) APTES film atop the perovskite
11. Drop a thimble-full of encapsulant onto the film
12. Press another 1" by 1" glass slide atop the encapsulant to spread the encapsulant atop the entirety of the perovskite structure

All the samples made using this method are shown in the manifest in Table 3.1.

Sample Number	$SiO_2$	APTES	t=84 hrs	t=300 hrs
01	NA	NA		
02	NA	NA		
03	50 nm	NA		
04	50 nm	NA		
05	150 nm	NA		
06	150 nm	NA		
07	50 nm	Long Exposure		
08	50 nm	Short Exposure		



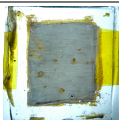
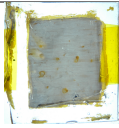
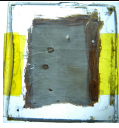
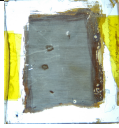
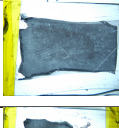
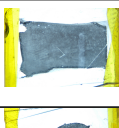
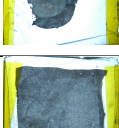
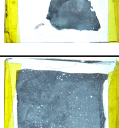
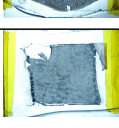
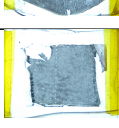
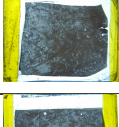
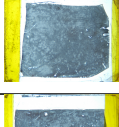
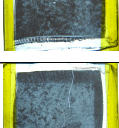
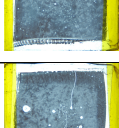
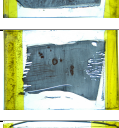
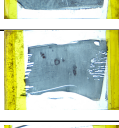
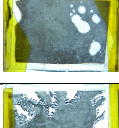
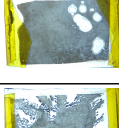
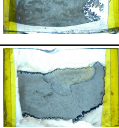
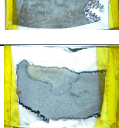
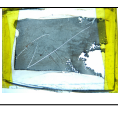
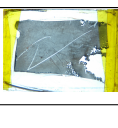






09	150 nm	Long Exposure		
10	150 nm	Short Exposure		
11	NA	NA		
12	NA	NA		
13	NA	NA		
14	NA	NA		
15	50 nm	NA		
16	50 nm	NA		
17	50 nm	NA		
18	50 nm	NA		
19	50 nm	Short Exposure		
20	50 nm	Short Exposure		
21	50 nm	Short Exposure		
22	50 nm	Short Exposure		

Table 3.1: **Perovskite Thin Film Manifest:** List of perovskite samples used for this project with the thickness of  $SiO_2$  thickness and APTES deposition method included. NA indicates that layer is not present in sample stack. Samples are all 1" by 1"

The design and fabrication of these samples were adaptive and changes in the fabrication procedure were made over time. Those changes will be highlighted in the results and discussion 3.2.2 as the stability of the samples informed the changes we made in the synthesis process.

### 3.2.2 Results and Discussion: Encapsulated Devices

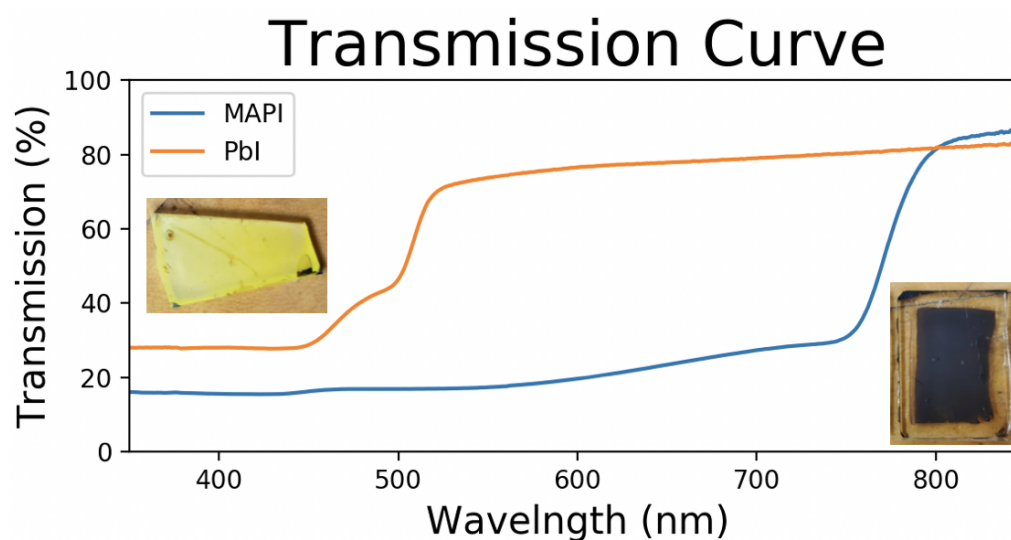


Figure 3.4: **Perovskite Transmission Spectra** Transmission spectrum of brand new MAPI thin film (Bottom left / dark grey film) and a sample that has fully degraded into PbI (Top right/ yellow film).

The quality of the perovskite thin film was quantified by its transmission curve and a visual inspection of the perovskite film's color through image analysis.<sup>3</sup> An transmission curve was taken for each sample when it was fabricated, an example absorption curve is shown in Fig. A.5. Fig. A.5 also displays the transmission curve of a perovskite thin film that has fully degraded into PbI. Transmission curves of

<sup>3</sup>All post-processing and visualization of data was performed in R-studio.

the samples are taken at different times during the entire period they are exposed to humidity. Three separate analyses are done on the transmission curves of these samples:

1. By calculating the area under the transmission curve it is possible to quantify the total absorption intensity (AI) of the Sample
2. Plotting this AI as a function of time it is possible to calculate the AI decay slope which gives a quantifiable comparative variable
3. Using the Tauc Plot analysis of transmission curves cut-on it is possible to calculate the materials band gap and then measure that as a function of time.

To start breaking down this data we will segment the data by sample structure, and start with Sample 1, shown in Fig. 3.5 A. There is no visual difference in the  $t = 84$  hours and  $t=300$  hours, images. Sample 1 has the solitary perovskite thin-film structure encapsulated by the DC-93-500 and two glass slides. The thicknesses of these layers, shown in Fig. 3.5 B, were measured mechanically for the glass and DC-93-500 layers and using ellipsometry for the other layers. Of all the samples measured, the perovskite thin-film layers were measured between 1.1 to 1.8  $\mu\text{m}$ . Examining the transmission curves in Fig. 3.5 C, we see the typical transmission spectra for a pristine perovskite thin film, that within the first 84 hours undergoes a vertical translation by about 10%. This vertical translation is not indicative of degradation, but a settling of the encapsulant within the encapsulant making it more transmissive. Beyond this shift due to settling in the encapsulant, no degradation is seen in the film over time.

Moving to Sample 3, which compared to Sample 1, just has the addition of the 50 nm layer of  $\text{SiO}_2$ , which is shown in Fig. 3.5 E. The thickness was confirmed by ellipsometry measurements to be  $50 \text{ nm} \pm 1 \text{ nm}$ . Fig. 3.5 D, shows the images of Sample 3, which show no visual difference in the  $t = 84$  hours and  $t=300$  hours, images and are very similar to Sample 1. The transmission curves for Sample 3, shown in Fig. 3.5 F, displays a gradually increasing degradation rate within the transmission spectra, with little effect on the above band gap region ( $<770 \text{ nm}$ ). The obvious explanation is the ingress of moisture and oxygen into the film, however, this degradation wasn't seen in Sample 1. Another mechanism for this degradation is the generation of surface defects at the perovskite- $\text{SiO}_2$  interface during the evaporation in step 7 of the fabrication project. More speculation on this in the next few sections.

Sample 7 in the manifest shows a significant change in film color/morphology compared to that of Sample 1, as shown in Fig. 3.5 H. This sample is identical to Sample 3, with the addition of APTES atop the  $\text{SiO}_2$  layer. Ellipsometry measurements show that the APTES layers vary between 2.4 nm to 3.6 nm in thickness. The deposition method used for Sample 7 is labeled as Long Exposure in Table 3.1, due

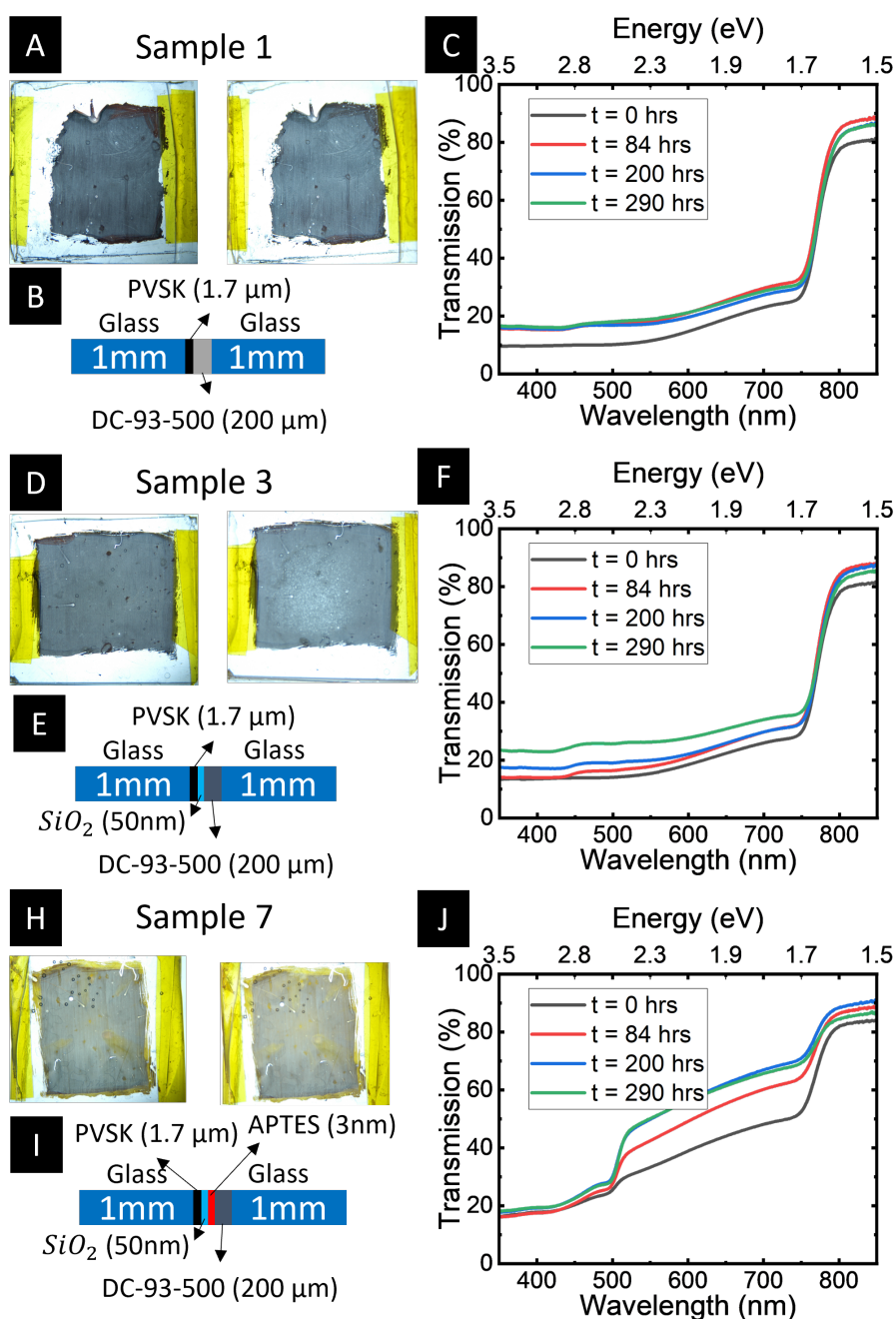


Figure 3.5: **Simple Perovskite Structure Behaviour** A: Displays the  $t=84$  hrs on the right and  $t=300$  hrs images of sample 1. B: Displays the vertical structure of the sample with their thicknesses. C: Displays the transmission curves of the sample at different exposure times to the humid environment.

to the deposition method used. In this method, We drop-cast 2ml of the APTES-Acetone solution while spinning at 200 RPM for 30 seconds then ramping up to 2000 RPM for 30 seconds. The acetone the APTES was suspended in appears to have had a detrimental effect on the perovskite film's transmission spectra, as shown in Fig. 3.5 J. The  $t = 0$  curve appears markedly different than Sample 1 and 3 with a pronounced slope between 500 nm to 770 nm, this increase in transmissivity increases over the remainder of the test. The solvent Acetone the APTES is dissolved in is known to degrade organic molecules such as the center cation in the perovskite structure, which would prompt the formation of  $PbI_2$ . This Acetone induced  $PbI_2$  formation mechanism is supported by the yellow spots in the film, as the  $PbI_2$  phase is yellow.

Due to this result, we modified the APTES deposition process to be: drop-cast 2ml of the APTES-Acetone solution while spinning at 200 RPM for 5 seconds then ramping up to 2000 RPM for 30 seconds to decrease this degradation. Altering this step resulted in APTES films between 1 nm to 2 nm in thickness, approaching the monolayer limit. This was measured through ellipsometry using a Horiba Uvisel DUV-NIR spectroscopic ellipsometer.

### Total Absorption Intensity Decay

The AI is calculated by calculating the area under the transmission curve from 400 nm to 750nm, just before the cut-on of the band gap. This is in comparison to the area under the same region in the  $PbI_2$  spectra which we take to be zero "Absorption". The change in the total AI for all 21 fabricated samples is shown in Fig. A.6 To identify which line and points correspond to which device structure use the legend on the right of Fig. A.6. All samples have the basic perovskite film, if  $SiO_2 = 0$  then there is no  $SiO_2$  layer atop the perovskite, if  $SiO_2 = 1$  there is a 50nm layer atop the perovskite and if  $SiO_2 = 3$  there is a 150nm layer atop the perovskite. If APTES = 0 then no perovskite is deposited, if APTES = 1 then the prolonged exposure deposition method was used, and if APTES = 2 then the immediate deposition was used.

What we see with this data is that there is a predictable change in the absorption within the perovskite and perovskite/ $SiO_2$  samples, a gradual 10% decrease in the samples AI over the 300-hour test. As far as total AI to start, the perovskite and perovskite/ $SiO_2$  samples are interchangeable, also showing the same behavior. However, Samples coated in APTES with the long exposure method both show lower than average AI's to start and show a total decrease of 20% AI over the 300 hr test. The remainder of the APTES coated samples were with the short exposure method. Two of the samples, 09/19, showed a 15% decrease in AI and then recovers to within 10% of their starting AI. The remaining 4 samples, 08/20/21/22 show little to no change from their initial AI over the 300 hr test. All APTES coated samples showed

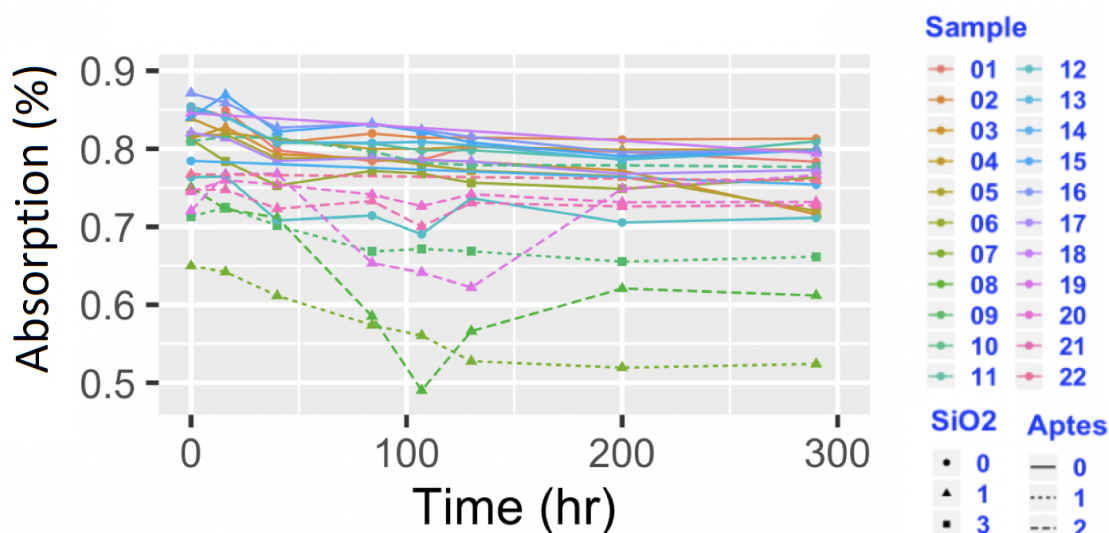


Figure 3.6: **Absorption Intensity Decay over 300 hrs** Displays the the decay of the AI over a given time of 300 hours.

a total maximum AI of 82%, on average, being outperformed by the perovskite and perovskite/ $SiO_2$ .

### Band Gap Extrapolation

We begin by using Tauc plot analysis, detailed in appendix A.1.3. Tauc plots are shown in Fig. 3.7 A/B/C for samples 1/3/7. Samples 1 and 3 show similar behaviors with an initial increase in bandgap in the first 84 hours followed by a settling of the bandgap to slightly lower energy. This tracks with the no visible changes in the samples and the slight changes in their AI over the 300 hr test. However, sample 7 displays a strong blue shift (shift to higher energy) which is also indicative of the formation of  $PbI_2$  regions speculated in the previous section. This blue shift due to the  $PbI_2$  is caused by  $PbI_2$ 's bandgap being at 2.2 eV. By looking at the overall change in bandgap for all the samples shown in Fig. 3.7 D. Only the APTES samples show an appreciable change in bandgap over time. This shows us that the change in AI from the PVSK and perovskite/ $SiO_2$  samples are due to the generation of localized defects and not  $PbI_2$  generation. Localized defect generation would cause a change in the AI without altering the bandgap of the material. To identify the exact mechanism for this degradation we first need to determine how far moisture ingresses into the film and if it can be the cause of the degradation we see.

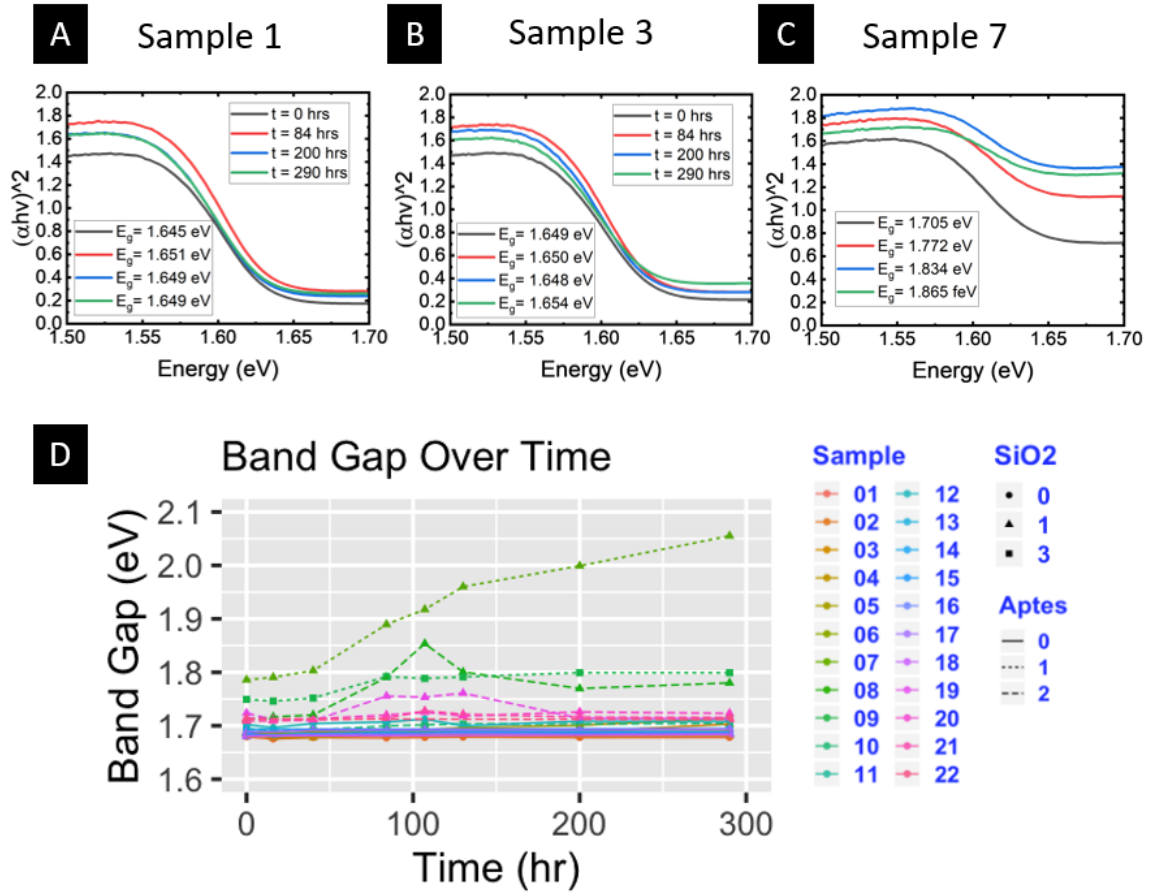


Figure 3.7: **Band Gap Extrapolation** A/B/C: Tauc plot of Sample 1/2/3 over time. D: All the sample band gaps as a function of time.

### Moisture Diffusion Analysis

To understand how moisture flows through the encapsulant we combine theory and simulation. To fully describe this system we need to look toward Fick's law. Fick's first law relates the diffusive flux to the concentration, under the assumption of a steady-state. It postulates that the flux goes from regions of high concentration to regions of low concentration, with a magnitude that is proportional to the concentration gradient (spatial derivative), or in simplistic terms the concept that a solute will move from a region of high concentration to a region of low concentration across a concentration gradient. Equation 3.2 shows the relation between the diffusivity  $D$ , the particle number  $n$ , and the particle flux  $J(n)$ .

$$-D\nabla n = J(n) \quad (3.2)$$

Since we are modeling how moisture flows through our encapsulant and all directions are symmetric we can both, simplify Equation 3.2 to the 1-D case and ignore boundary conditions. These constraints give us Equation 3.3.

$$-D \frac{dn}{dx} = \frac{d_n(x)}{dt} \quad (3.3)$$

By taking a single boundary condition into account, the air/encapsulate interface in the form of the variable A. It is possible to solve Equation 2 giving the result shown in Equation 3.4.

$$n \propto A * \operatorname{erfc}\left(\frac{x}{2\sqrt{Dt}}\right) \quad (3.4)$$

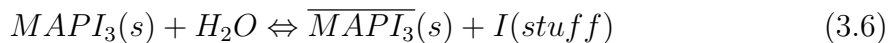
In Equation 3, A represents the saturation concentration  $n_0$ . Dividing the particle number by the saturation constant results in Equation 3.5.

$$\frac{n}{n_0} = \operatorname{erfc}\left(\frac{x}{2\sqrt{Dt}}\right) \quad (3.5)$$

Equation 3.5 represents the relative humidity (RH) inside the encapsulant itself. This equation itself allows us to simulate and extrapolate the RH at any given distance from the encapsulant boundary at any given time. This result allows us to simulate the diffusion of moisture into the encapsulant. Still, images of the dynamic particle simulation are shown in Fig. 3.8

In addition to the dynamic simulation, it is possible to plot the moisture ingress into the encapsulant as a function of distance from the boundary x. This result is plotted in Fig. 3.9.

In Fig. 3.9 the longer the exposure to humidity the further a specific RH penetrates the encapsulant. For example, 20% RH penetrates 1 mm after 176 hours, 4 mm after 400 hours, and 1.2 cm after 1500 hours. The only thing left to be determined is at exactly what RH starts to decay the perovskite. That answer comes from a recent paper by Schlipf et. al. [71] In this paper they perform a detailed study of what RH does perovskite degrade and the specific chemical processes that happen during that degradation. Their finding suggests that the perovskite undergoes some degradation at 20% RH and fully degrades under 80% RH. Now to examine the perovskite moisture reaction in more detail.



Analysis of the Gibbs free energy of Equation 3.6 can give us the dynamics of this reaction. If the changes in the Gibbs free energy of the system are positive the reaction moves forward if it's negative it does not progress. Starting with the expression for the Gibbs Free Energy in Equation A.13 we can set it equal to the chemical potentials for all our specific species in Equation 3.8.



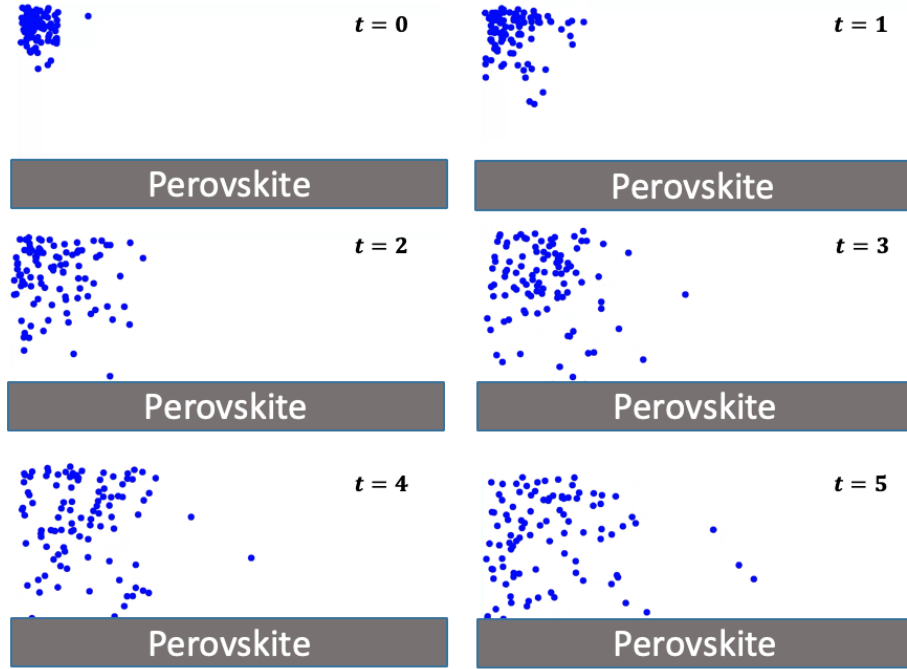


Figure 3.8: **Moisture Ingression Simulation** Dynamic simulation of moisture particles diffusing into the encapsulant at a single point of entry. The length scales and time constants involved are arbitrary and just for illustration purposes.

$$\Delta G_R = \Delta H_R - T\Delta S_R \quad (3.7)$$

$$\Delta G_R = \sum \mu_i = \mu_{MAPI_3} + \mu_{H_2O} = \mu_0 + RT\ln(\bar{P}_i) \quad (3.8)$$

The chemical potential of a solid is known and the chemical potential of a gas is a function of the gasses partial pressure  $\bar{P}_{H_2O}$ . In this case, the partial pressure is equal to the RH inside the encapsulant. By ignoring the constant  $\mu_0$  we arrive at the final expression in Equation 3.9.

$$\Delta G_R = RT\ln\left(\frac{n_{H_2O}}{n_{tot}}\right) \quad (3.9)$$

When the concentration reaches a point where the Gibbs free energy is positive the decay of the perovskite begins. Putting this together with the perovskite degradation at 20% and the 20% RH inside the encapsulant being a function of depth, this means these samples should degrade into  $PbI_2$  from the outside in.

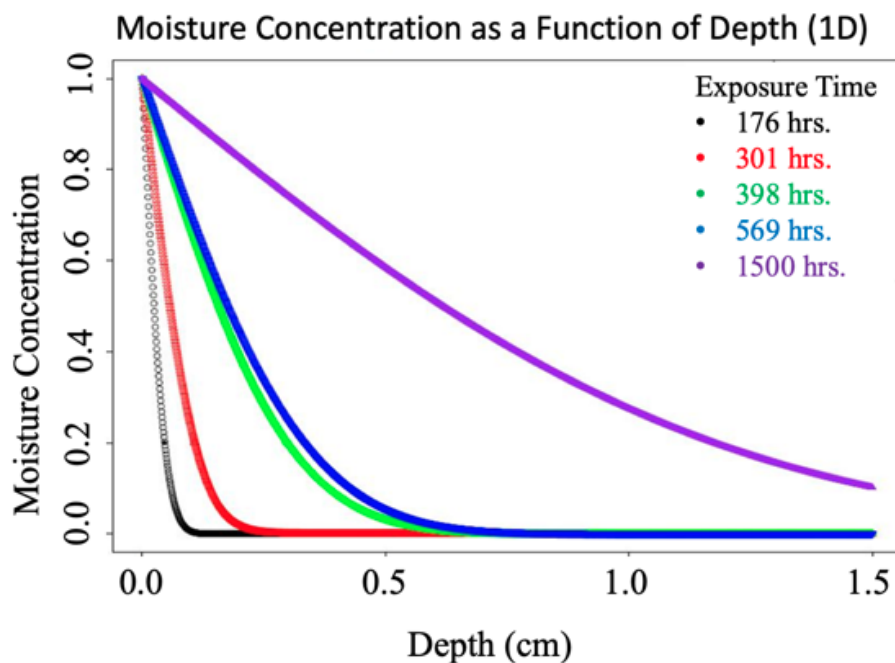


Figure 3.9: **Moisture Penetration Depth** Moisture penetration as a function of depth from the encapsilant/air interface.

### 3.2.3 Conclusions

The results of different sample structures in a 100% RH for 300 hrs at 40 C show minor to major signs of degradation in all the sample structures. In the APTES-free structures, this degradation is limited, as seen by the small changes in bandgap and AI over the 300 hr period. However, the APTES samples show a strong sign of  $PbI_2$  inclusions at a synthesis that appear to grow over time, as seen in the sample images, changes in AI, and blue-shifting of the bandgap. The majority of the instability in the samples appears to come from the deposition of the APTES layers and to some small part, the deposition of the oxide layers on the perovskite. The synthesis of these layers causes more defects and  $PbI_2$  centers than they prevented moisture contact with the perovskite. Simulations suggest that with a large enough erased region between the sample edge and the perovskite, any length of moisture ingress can be abated. In fact for the 21-day (500 hrs) AIAA standard humidity test, only a 5mm gap would be needed for any sized array to prevent moisture perovskite contact. Overall, a perovskite thin film on its own in this structure should have no issue meeting an official AIAA standardized test.

### 3.3 10 Month Space Flight of Sample 18

Herein we report the post-flight analysis of an encapsulated MAPI thin film (Sample 18, Table 3.1) flown to the international space station (ISS) as a part of the Materials International Space Station Experiment (MISSE) 13 and exposed to the space environment for 10 months. Herein dubbed the MISSE 13 Flight Sample. The sample was mounted on the Zenith position of the cube, exposed to the sun at the same interval as the ISS, as seen in Fig. 3.10 C. An identical sample (Sample 15, Table 3.1) and a MAPI sample with no barrier layer (Sample 14) were left on earth in a routinely used<sup>4</sup> nitrogen sample box. Herein dubbed Control Sample A and B respectively. Optical Photoluminescence (PL) and Time-Resolved PL (TRPL) maps performed on both samples reveal similar PL intensities for both samples but with Control A sample having longer average recombination lifetimes (8 nanoseconds (ns)) compared to the flight sample (4.5 ns). In addition, Control B demonstrates the traditional structural phase transition at 120 Kelvin (K) from tetragonal to orthorhombic structure, while the flight sample does not undergo this until 70 K. These two factors point toward a higher number of surface defects present in the flight sample. However, under exposure to 1 Sunlight soaking (LS) for 18 hours, the Control B sample showed significant and permanent yellowing, while the flight sample and Control A were unaffected, further emphasizing the different mechanisms affecting these two. We also examine the roles that thermal cycling, high-energy particle, and UV radiation may have had in increasing the number of surface defects in the flight sample, and find that these did not have a significantly detrimental effect on its optical properties, including carrier photogeneration, recombination, and photostability.

#### 3.3.1 Timeline

Methylammonium Lead Iodide ( $CH_3NH_3PbI_3$ ) perovskite thin films were fabricated and encapsulated with DC-93500 space-grade encapsulant for the project detailed in Sec. 3.2 project, in July of 2019. [72] A more detailed schematic of the sample stack is shown in figure 3.10 A. In October of 2019, a last-minute space opened on the MISSE 13 mission and two samples we selected from this previous project, both had shown no signs of visible degradation or change in transmission spectra. At random one was designated the MISSE 13 Flight sample while the other was ground control B.<sup>5</sup> Both samples were sent to Aphaspace in Florida and left in ambient conditions while preparing for spaceflight. The MISSE 13 flight sample was mounted on the Zenith (sun-facing) position on the MISSE Cube, figure 3.10 C from mid-March 2020 to mid-January 2021, approximately 10 months. Post-flight analysis began in July

<sup>4</sup>Often opened and closed to retrieve samples allowing intermittent oxygen and moisture exposure.

<sup>5</sup>Due to the fact these samples were fabricated at NASA Glenn and the spot on MISSE 13 was last minute, the level of pre-flight analysis was limited to transmission spectroscopy and visual analysis.

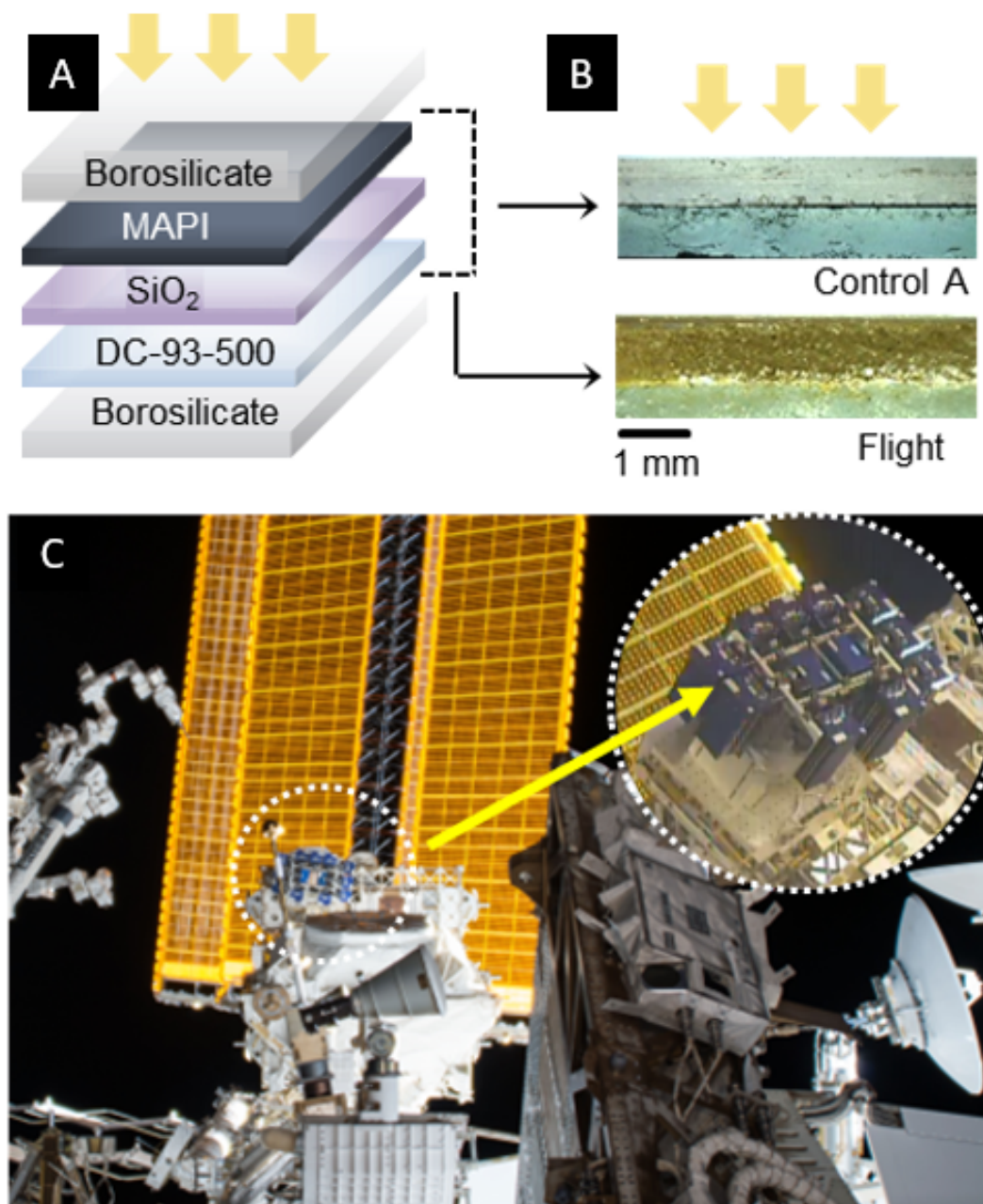


Figure 3.10: MISSE13 sample pre- and post-flight (A) Schematic of assembled layers. (B) Photographs of edges of (top) Control A and (bottom) Flight sample, both post-flight. (C) ISS on day 52 of MISSE duration. Yellow arrows indicate the position of the MISSE13 sample.

2021, two years after the initial synthesis.

### 3.3.2 How Perovskite Optical Properties Correlate to Electrical Performance

Due to the sample being encased in glass, we are restricted to measurements that can be done through 1 mm of glass such as reflection/emission confocal microscopy, PL, TRPL, and resorption measurements. It becomes necessary to correlate the measured optical properties to possible electrical properties to predict how the film would perform in a full device stack. The main optical measurements performed in this study are PL and TRPL. PL spectra of the MAPI films were fit with a Gaussian function shown in equation 1.

$$f(x) = Ae^{-4(\ln(2)(x-x_c)^2/\lambda^2)} \quad (3.10)$$

With A being the amplitude of the Gaussian function,  $x_c$  being the center wavelength, and  $\lambda$  as the linewidth, also known as full-width half max (FWHM). Discounting amplitude and the corresponding intensity metric,  $x_c$  represents the band gap of the film, influencing band alignments in a full device. The most important PL metric is linewidth ( $\lambda$ ), which above the  $1/2k_bT$  thermal background indicates the presence of defects in the sample. TRPL curves were fit with exponential decay functions, shown in equation 3.11, equal to the number of suspected decay routes, previous papers have fit perovskite TRPL decay curves with mono, and bi functions. [73]

$$f(x) = \sum_{n=1}^{\infty} a_n e^{-t/\tau_n} \quad (3.11)$$

Within the fit,  $a_n$  corresponds to the amplitude of the function, with a normalized mono-fit  $a_1 = 1$ . The lifetime is represented by  $\tau$  and represents the average length an excited electron will spend in the conduction band before radiatively recombining. The lifetime  $\tau$  is directly correlated to device variables of mobility and diffusion length, the longer the lifetime the better. Perovskite films are often fit with bi-exponential fits [73] with the lifetimes being spatially separated, versus the traditional electronically separated. One lifetime represents the center of a grain and the second lifetime the surface of the grains. Intrinsic defects in perovskites tend to migrate to grain surfaces where dangling bonds and surface degradation are present. [73] These surface defects act as scattering centers for excited electrons, decreasing their overall lifetime, thus, these double exponential fits also can act as indicators of surface defects in the perovskite film.

### 3.3.3 Degradation Mechanisms in Low Earth Orbit

The space environment poses challenges to the implementation of photovoltaics including:

1. Thermocycling as the ISS orbits the earth
2. High energy ionizing radiation
3. A strong Ultra-violet component

#### Thermocycling

Temperatures on the ISS can range from 100 C° in direct sunlight to -100 C° 45 min later when halfway through the earth's shadow. [74] Thermal cycling of perovskite devices has been extensively studied [52,75,76], but is often complicated by the use of a full device stack, so drawing parallels, in this case, is difficult. However, a recent study by He and company demonstrated that significant PL intensity loss and decreased lifetimes in an encapsulated MAPI film result from 200+ thermal cycles from -30 C° to 85 C°. [76] They attribute this loss to the constant structural phase transition from tetragonal to cubic the MAPI film undergoes at around 30 C°. In comparison to our study, the MISSE film undergoes a similar temperature cycle upwards of 4,500 times over the 10-month mission, leaving thermal cycling as a possible cause of the increased surface defects we observe.

#### AM0 UV Component

Another complication is the UV component of solar radiation that is doubly strong at the ISS than on the surface of the earth. [77] UV illumination has been linked to degradation into Perovskites [78–80], specifically under ambient conditions, however, encapsulated perovskite degradation due to UV is 80% reversible under 1 Sun illumination [80].

#### High Energy Ionizing Radiation

The third complication is ionizing radiation which primarily comes from galactic cosmic rays, particles trapped in the earth's magnetic field, and solar energetic particles. For example, the proton flux for our size sample on the ISS is estimated to be  $10^9$  impacts over the 10 months. [81] Secondary particles (protons, neutrons, and heavy ions) are also generated from radiation striking an object, such as the ISS hull or the perovskite itself. High energy ionizing radiation causes damage upon deposition into a material, making it necessary to review the structure of our sample. The Perovskite film is just behind 1mm of borosilicate glass, using SRIM (Stopping and Range of Ions

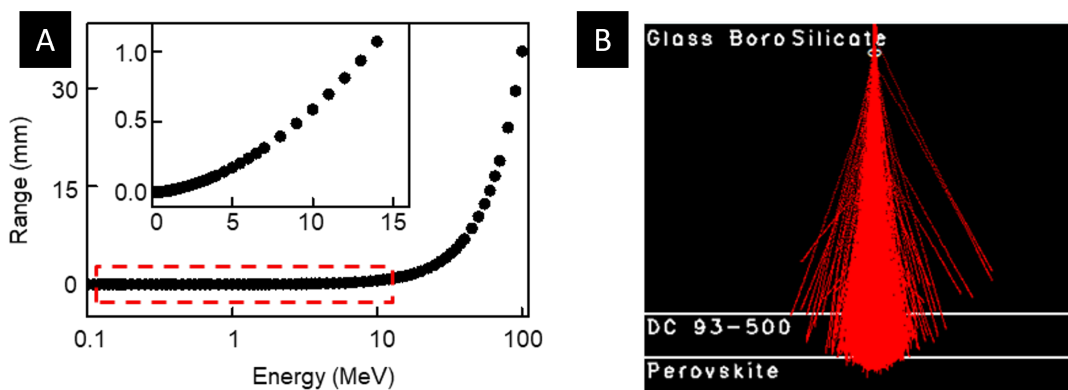


Figure 3.11: **The Role of Radiation** Results of SRIM (Stopping and Range of Ions in Matter) and TRIM (Transport of Ions in Matter) simulations. A: SRIM Penetration depth of protons in borosilicate glass as a function of energy. Inset shows the energy of protons within the 1mm thick cover glass. B: TRIM ion simulation for perovskite sample using 14 MeV protons.

in Matter) and TRIM (Transport of Ions in Matter) simulations only 11 MeV to 15 MeV have a chance of depositing in the perovskite layer. The results of the SRIM and TRIM simulations for our sample structure are shown in Fig. 3.11. Despite the high number of particle impacts possible for our sample, perovskite films and devices have proven to have a high radiation tolerance. [82–84] Kanaya and group demonstrated that 50 keV protons that stop in the perovskite layer do not significantly affect the grain size or crystal structure but do decrease electron lifetimes above  $10^{15}$  p/cm<sup>2</sup> proton fluence. The effect fast neutrons had on perovskites was studied by Paterno and the company showing that an 80-year neutron exposure on the ISS would only result in a small decrease in the short circuit current of the cell. [85]

### 3.3.4 Optical Analysis

The images in Fig. 3.10 show no discoloration in the glass for Control A, but significant yellowing is seen in the MISSE sample. This level of yellowing has been previously reported with similar soda glass samples sent to space. [60]

### 3.3.5 Confocal Analysis

Using an LSM 880 Zessis the samples were excited with a 405nm laser while collecting between 400 nm and 410 nm for one scan to get the reflection image in Fig. 3.12 A. Then by alternating beamsplitters images were collected between 490 nm 530 nm

Sample	$PbI_2$ Inclusion Area	$PbI_2$ Total Area
Control B	2,761 $\mu\text{m}^2$	24 %
Control A	50 $\mu\text{m}^2$	4.3 %
Control A (LS)	40 $\mu\text{m}^2$	4.1%
MISSE Flight	274 $\mu\text{m}^2$	12 %
MISSE Flight (LS)	80 $\mu\text{m}^2$	6 %

Table 3.2: **Non-Emissive Areas/ $PbI_2$  Inclusions** Displays the average size of the  $PbI_2$  Inclusions and total area they cover

and 700 nm to 800 nm, shown in Fig. 3.12 B and C, respectively. The collection region between 490 nm and 530 nm is to capture possible  $PbI_2$  emissions. Based on the absorption spectra in Fig. A.5 the  $PbI_2$  bandgap is within this collection region. The 700 nm to 800 nm region is to collect the emission from the  $CH_3NH_3PbI_3$  film, with its previously measured bandgap of 1.6 eV. The sample is shown in Fig. 3.12 A, B, and C is the edge of the MISSE 13 sample. The image is pockmarked with holes that are both non-reflective and non-emissive. These regions do show up in the Fig. 3.12 B image, suggesting that these non-emissive areas are  $PbI_2$  inclusions within the samples.

Moving to a more detailed analysis of the Ground and MISSE samples, Fig. 3.12 D/E/F/G display the emission maps from 405nm excitation of Control A, MISSE Flight, Control B, and Flight Post LS samples respectively. Control A has a multitude of small non emissive /  $PbI_2$  regions. Control B's map displays large connected portions of the surface of the film as non-emissive/ $PbI_2$  inclusions in contrast to the MISSE Flight map that shows small pinpricks of the area as non-emissive/ $PbI_2$  inclusions, similar to Control-A. This is likely due to the lack of the  $SiO_2$  barrier layer to prevent moisture and oxygen intercalation when sent to alph-space. Analyzing these images in Fiji using the particle analysis tool the average size of the  $PbI_2$  inclusions and the total area they cover within the sample were measured.

The statistics gathered from that analysis are shown in Fig. 3.12 H and Table 3.2. The MISSE sample's non-emissive areas/ $PbI_2$  inclusions are just over 3x smaller than Control B's non-emissive areas/ $PbI_2$  inclusions covering twice the area (24%) than that of the MISSE sample (12%). This suggests that the non-emissive areas/ $PbI_2$  inclusions in the MISSE sample are more numerous, which is backed by the data in Fig. 3.12 H. The non-emissive areas/ $PbI_2$  inclusions in Control sample A are similar to that of the MISSE sample, especially after light soaking. After the shrinking of the non-emissive areas/ $PbI_2$  inclusions in the MISSE sample, both the average size and total areal coverage percentages are similar.



### 3.3.6 Room Temperature PL and TRPL Analysis

One by one mm PL and TRPL maps with a step size of 0.2 mm with a total of 25 spots, of similar areas on both samples were taken, and the resulting data is shown in Fig. 3.13, with the statistical distributions of the observable plotted.

#### Energy

When examining the energy maps and distributions in 3.13 B, a drastic difference is seen in the PL energies. The MISSE 13 Flight sample displays a blue shift compared to Control A and B. As previously asserted and supported in Sec. 3.2.2, degradation of the perovskite structure results in a blue-shift in the bandgap of the perovskite structure surrounding the non-emissive areas/ $PbI_2$  due to the green, roughly 2.2 eV bandgap. Despite the larger areal coverage of the non-emissive areas/ $PbI_2$  inclusions in Control B, the blue shift is seen stronger in the MISSE flight sample. This may be due to the larger surface area contact of the non-emissive areas/ $PbI_2$  inclusions in the MISSE flight sample. This larger surface contact despite the larger area coverage is due to the smaller more numerous non-emissive areas/ $PbI_2$  inclusions within the MISSE flight sample. The differences between Control A and the Flight sample are drastic, likely due to the degradation caused by 10 months in space. After light soaking and the shrinking/healing of the non-emissive areas/ $PbI_2$  inclusions, the energies of the two samples are very similar. Essentially light soaking healed the sample back to its pre-flight parameters.

#### Lifetime

The single exponential decay fit analysis of the map data reveals longer lifetimes in Control B ( $\sim 6.5$  ns) versus the MISSE 13 Flight sample ( $\sim 5$  ns). This suggests that both samples have undergone similar amounts of degradation. Control sample A displays twice the lifetime of the MISSE Flight sample, reinforcing the theory that the MISE Flight sample underwent some degradation in space. After light soaking the MISSE Flight sample lifetime triples. This result is interesting as it suggests the film has healed beyond the properties of the controls.

#### Resorption Measurements

The confocal non-emissive regions in the film, reduced excitonic lifetimes, and blue-shifted center wavelength all point to an increased number of defects in the MISSE sample in relation to Control A, in addition, the TRPL data suggest the presence of additional defects in the MISSE Flight sample from its 10 months in space. To further analyze the defect mechanisms at play, resorption measurements were performed on the sample. The resorption measurement is done by collecting PL from the edge

of the sample while varying the distance of the excitation point, More details in Appendix A.2.3. Figure 3.14, displays the red shift in the samples as a function of this same separation  $d$ . This measurement is based on the total internal reflection of the perovskites emission, with that emission being reabsorbed by the film and then re-emitted. The more resorption and re-emission the further the sample redshifts, signifying shallow defects within the band-gap of the perovskite. The redshift of the samples is similar, suggesting similar defect densities within the samples.

### 3.3.7 Temperature Dependent Properties

To further identify the differences in type and number of defects in the samples temperature-dependent optical spectroscopy was performed from 10 to 300 K. Fig. 3.15<sup>6</sup> A and B display the PL Maps for Control A and MISSIE 13 Flight samples respectively, while panels D, and E display the Energy and Linewidth as a function of temperature, extracted from the PL maps. The thermal PL maps display a blue-shifting "kink" at 145 K for Control B and 55 K for the MISSE sample. The "kinks" are reflected in the center wavelength by a sudden blue shift and in the linewidth by an increase in the FWHM at the transition temperature. [86] This increase is due to the PL splitting into a double Gaussian but still being fit by a single Gaussian, extending the FWHM artificially for the 30K surrounding the transition temperature. This kink is traditional of the structural phase transition from tetragonal to orthorhombic crystal phase at 148 K, further indicated by the shift in energy displayed in panel C. [86] previously discussed in Chapter 1.1 for perovskites. The MISSE sample exhibits the interesting behavior of not phase transitioning until 55K, also indicated by the blue shift in Panel C. This result is unique in that the MAPI structural transition from Tetragonal to Orthorhombic has never been observed so low before. Surface defects present in the sample may make it necessary to remove much more of the thermal background before the Orthorhombic structure is stable, this is supported by the close ties between surface energy and the structural phase. [30, 87]

The presence of defects is backed by the large low-temperature linewidth that we see in Panel G for the MISSE Flight sample versus the Control B, 55 meV compared to 35 meV respectively. Such a large difference in the low-temperature linewidth suggests the presence of defects in the MISSE sample that are either not present in the Ground sample or present in a much lower density. After light soaking the MISSE Flight sample reverts to the typical transition temperature.

### 3.3.8 Photostability

To identify the effect of the defects on the stability of the samples under AM-1.5 illumination, both samples were exposed to AM-1.5 illumination for 15+ hours while collecting PL. The collected PL intensity as a function of time is plotted in red and black in figure 3.16 A. Both samples show an initial decrease in PL intensity to  $\sim 75\%$  initial intensity in the first 30 min, beyond this, the ground sample maintains its intensity for the remainder of the test while the MISSE sample starts increasing with time, surpassing its initial intensity at 12.5 hrs. Insets of the sample images before and after the photostability test are shown to the right of Panel A for the Ground sample and MISSE sample. The center wavelength, plotted in figure 3.16 B, Shows similar behavior for the MISSE and Ground samples, yet with different magnitudes. A blue shift in MAPI perovskite is indicative of degradation into lead iodide before complete yellowing occurs [88]. PL intensity increase over time can be a sign of defect passivisation [88], where electrons cascade into defect energy levels and become trapped, leaving the states inert, allowing for more radiative recombination.

### 3.3.9 Conclusion

Post 10-month space flight optical analysis of the MISSE sample reveals a higher number of surface defects when compared to the Control A and B samples. The low (55K), never before reported, tetragonal to the orthorhombic phase transition temperature, is most likely caused by a tensile strain applied to the film. This strain affects the surface energy and as surface energy and structural phase are closely linked this affects the phase transition. This cause and effect are supported by the large blueshift in the MISSE Flight sample caused by 10 months in space. This strain is likely healed by the light soaking-induced shrinking of the non-emissive regions, releasing the tensile strain. After the photostability measurements, Control B degraded into lead iodide while the MISSE sample remained unblemished. This degradation is attributed to the possibility of moisture ingress within the DC93-500 encapsulant of the Ground sample. Both Control B and MISSE samples were exposed to the same amount of humidity, allowing some moisture to ingress into the encapsulant, [72] however, the moisture ingress of the MISSE sample was most likely reversed due to the  $10^{-7}$  torr of the space environment and the extra barrier layer. [74] This also explains the discrepancy in the confocal images, where the large non-emissive regions in Control B can be explained by moisture degradation. The pinpricks of non-emissive regions on the MISSE sample and Control A were likely a result of synthesis. Regardless of the cause, the Perovskite thin-film survived 10 months in the space environment returning with no visual differences. The properties that most correlate to device

---

<sup>6</sup>Each data acquire was taken at the same spot on the sample, repeat scanning measurements reveal extracted vales do not differ by more that 2%

performance namely linewidth and electronic lifetime were minimally changed from the Ground control sample. The findings of this study are promising for Perovskites implementation for space-based photovoltaics.

### **3.4 Conclusion**

The application for OMHP in PV is boundless with outstanding performance both in PV efficiency and for possible space-based PV. The next steps are the testing of full perovskite cells in space. Along with the development of an in-space synthesis method for an all evaporative perovskite solar cell, allowing the printing of large-area arrays for unlimited power generation in space.

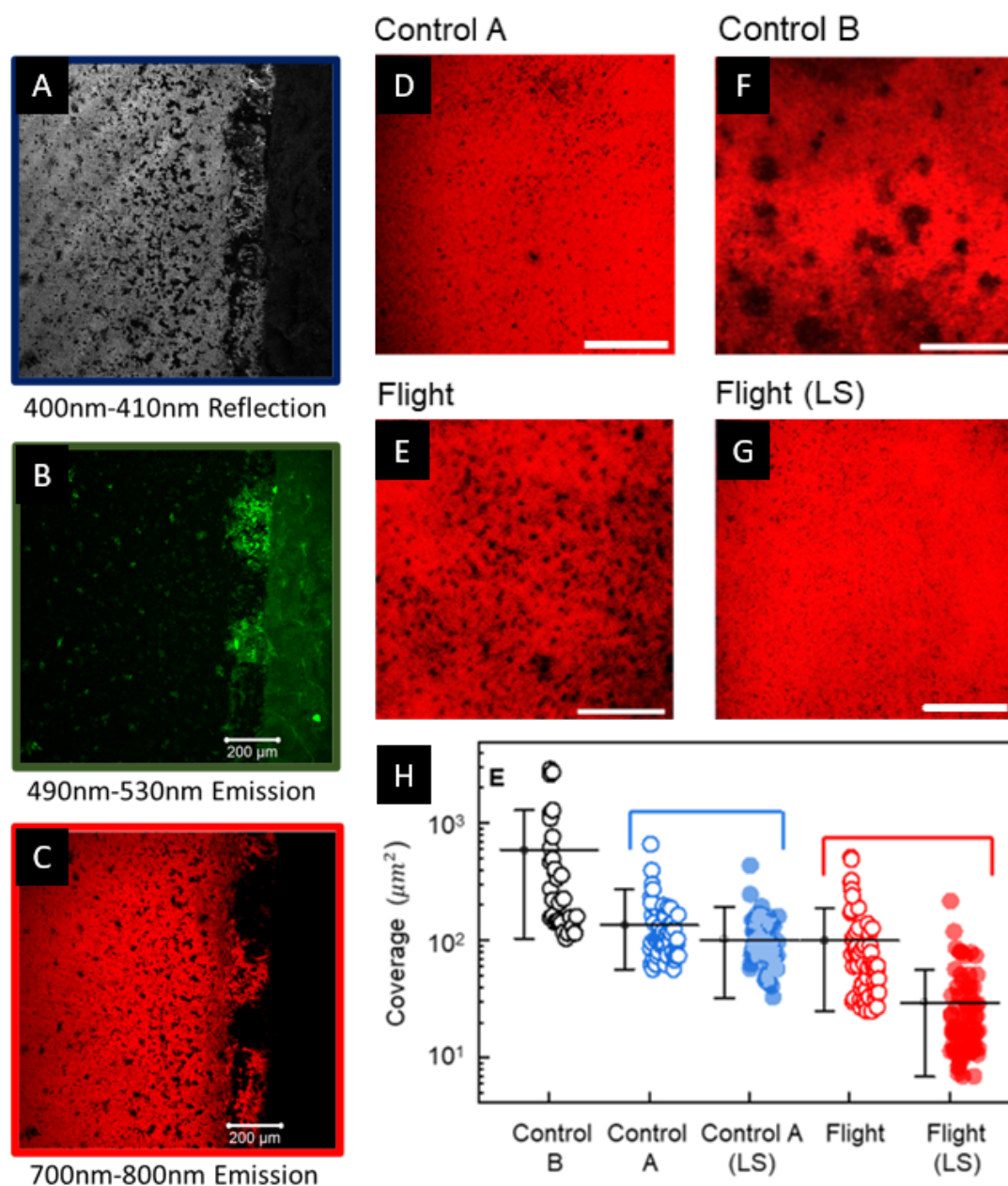


Figure 3.12: **Confocal Analysis of MISSE 13 Sample A/B/C**: Displays the 400/490/700 nm to 410/530/800 nm collection maps for the edge of the Ground Control Sample. D/E: Are the emission maps for the Ground/Emission Samples. F: Displays the statistics and averages for the  $PbI_2$  inclusions in the two samples. A,B,C images are identical in dimension and scale bars are  $200 \mu m$ . D,F,E,G images are identical in demension and scale bars are  $200 \mu m$

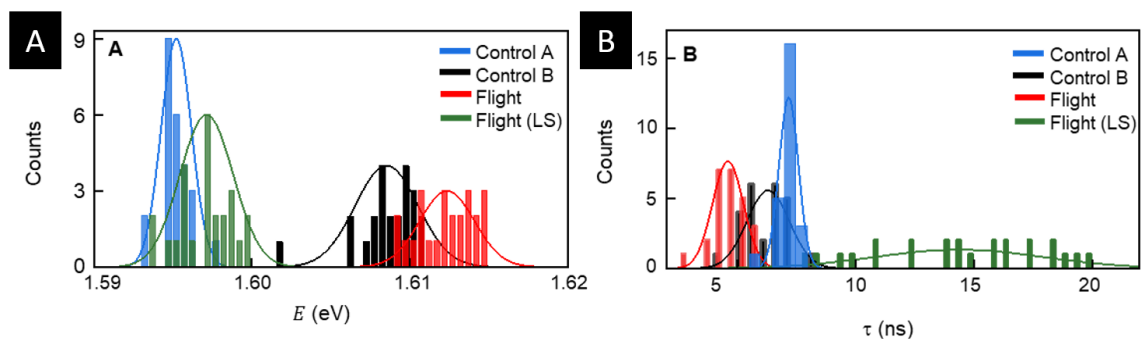


Figure 3.13: **PL and TRPL Maps A/B** Statistical distributions Energy and Lifetimes from PL and TRPL Maps.

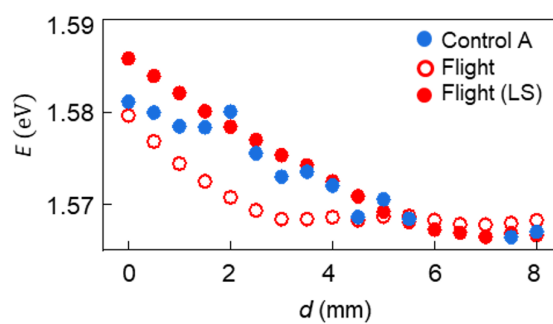


Figure 3.14: **Resorption Measurements** Redshift as a function of the probe beam distance.

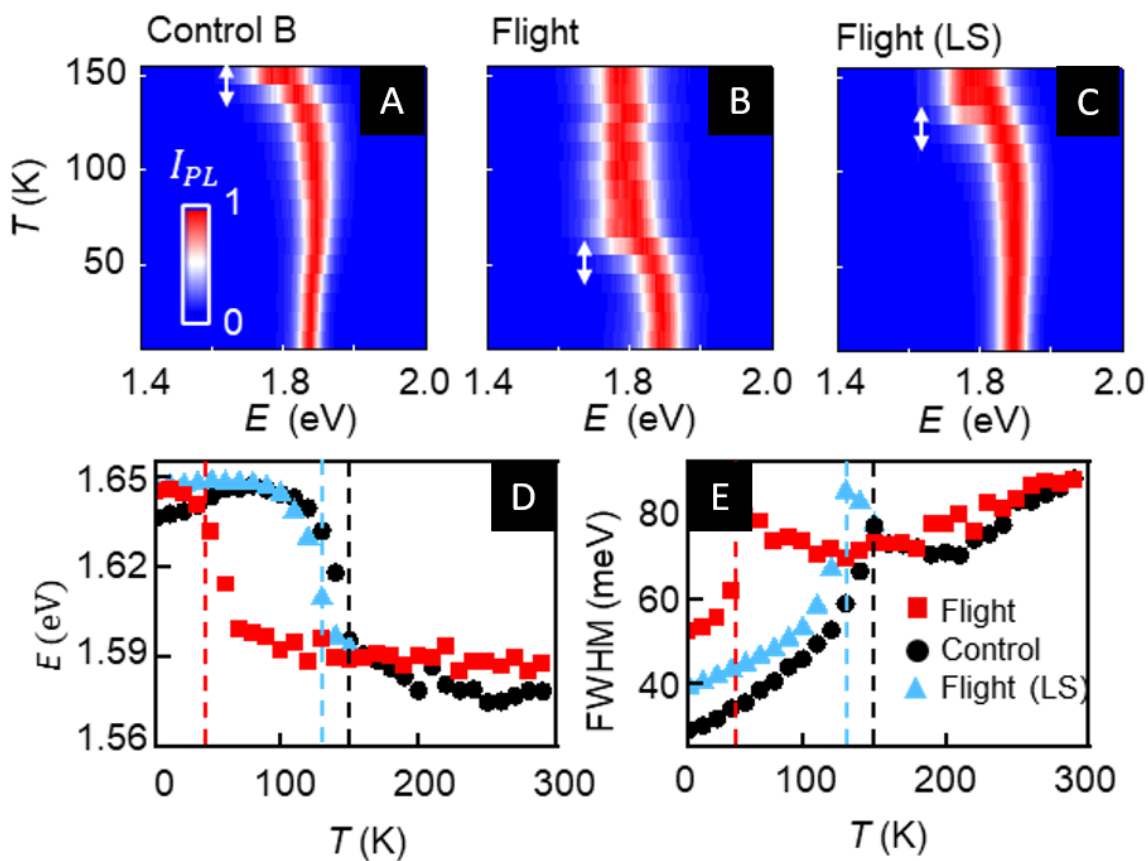


Figure 3.15: **Temperature Dependent PL** A/B: Temperature dependent PL Maps, where each temperature is a PL spectra. C: Displays the temperature dependent PL map of the flight sample after light soaking. D/E: Displays the PL-Energy / PL-Linewidth as a function of temperature. Both maps are in steps of 10K.

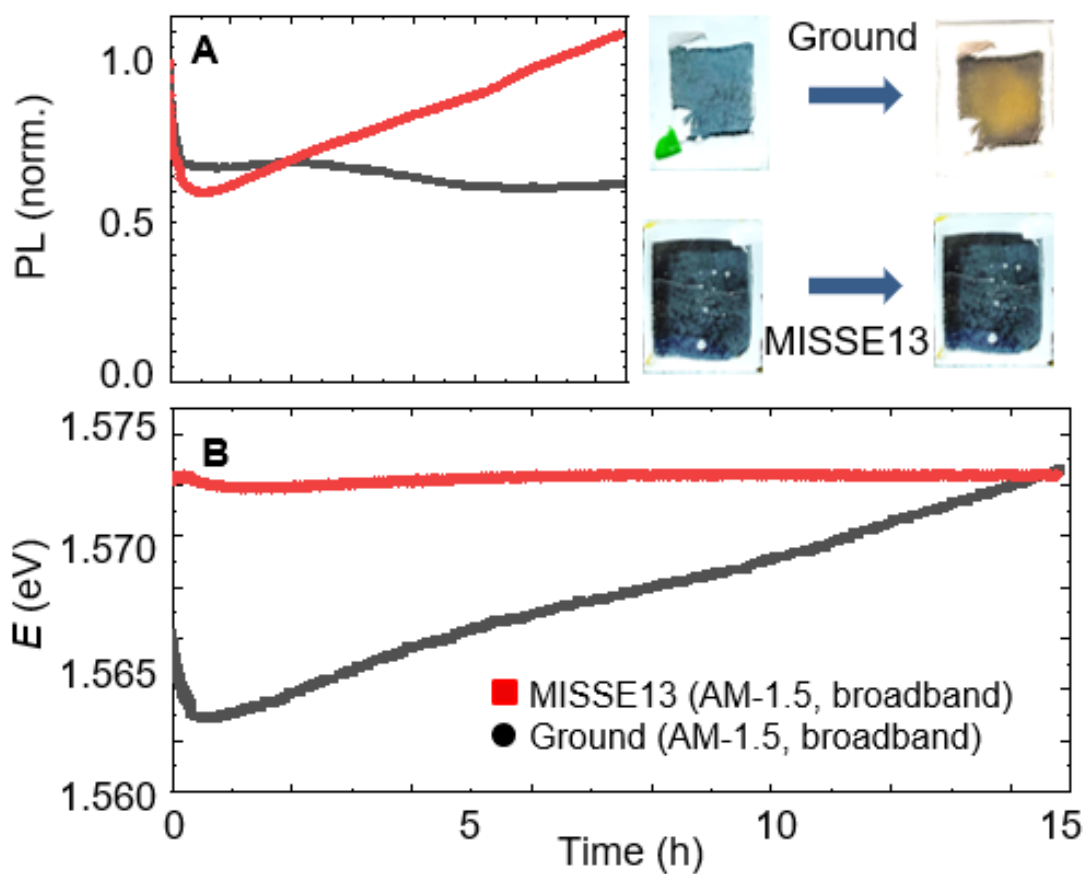


Figure 3.16: **AM 1.5 Photo-stability Test A/B**: The PL intensity/Energy as a function of time. With insets of the sample images before and after the test. Both A and B are to 15 hours.



# Chapter 4

## Charge Dynamics of 2-D Perovskites

Two-dimensional layered perovskites (2DLP) are a more recent class of OMHPs that have attracted strong interest. [89, 90] This new class of perovskite, known as 2-D Ruddlesden–Popper perovskites, has gained so much recent attention due to their stability in ambient conditions. This is due to the use of a different organic molecule used at the center of the perovskite structure, increasing inter-layer spacing, and causing quantum confinement of the layers, hence 2-D perovskites. Unlike most 3-D perovskites, the organic spacer molecules used are hydrophobic, giving enhanced stability in ambient conditions. [91]

### 4.1 Crystal Structure

A typical crystal structure, shown in Fig. 4.1 can be described by  $L_2A_nX_{3n+1}$  where L is an organic component, A a metal cation, and X a halide anion. The metal halide octahedra are arranged in planes forming layers, with the organic molecules acting as spacers in between. In this equation,  $n$  denotes the number of planes that are sandwiched between the organic molecules, and their hydrophobicity has been identified as the cause of superior environmental and moisture stability in 2DLPs.

### 4.2 Effect of Quantum Confinement

2DLPs have additionally demonstrated improved optoelectronic properties compared to their 3D counterparts, which include high photoluminescence (PL) quantum yield, attributed to their higher exciton binding energies due to stronger quantum confinement. This in turn leads to the formation of stable excitons at room temperature,

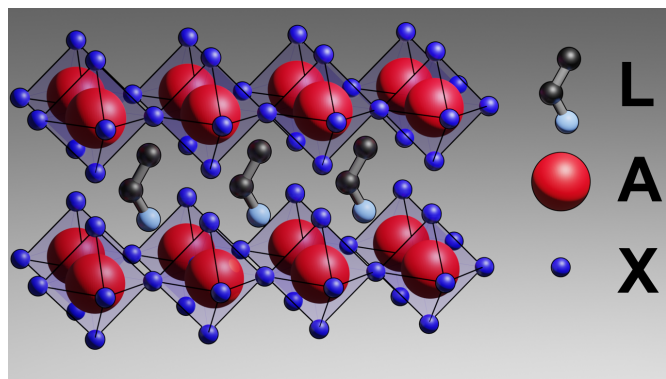


Figure 4.1: **2DPL Crystal Structure** Example of the  $L_2A_nX_{3n+1}$  where  $n$  is the number of layers in between the planes of organic molecules.

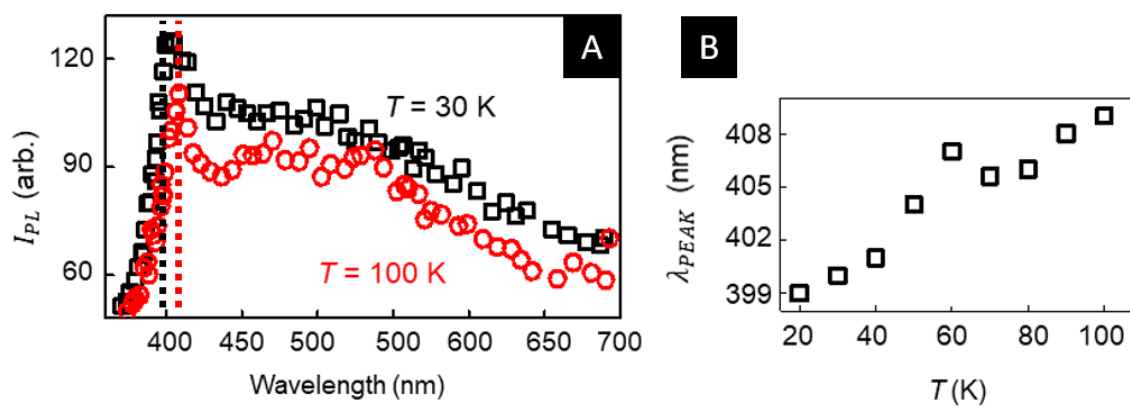


Figure 4.2: **2DLP Perovskite Emission** A: PL of undoped 2DLP at different temperatures. B: Peak wavelength of BE emission red-shifting with decreasing  $T$ .

making 2DLPs suitable candidates for light-emitting devices (LEDs), lasing, and polariton applications [91]. An example of the Band Edge (BE) emission of a  $Ea_2PbBr_4$  2DLP is shown in Fig. 4.2 A. Where the dashed lines show the centers of the BE emission at different temperatures. Fig. 4.2 B, displays the movement of the BE with increasing T displays a redshift with increasing temperature this is opposite of perovskites traditional blueshift due to inverse band ordering. Both exciton binding energy and band gap can be tuned by varying  $n$ . [92]

### 4.2.1 Self Trapped Excitons

Another interesting aspect is the presence of self-trapped excitons (STE) in 2DLPs. [8,19,93] Large exciton binding energies and strong exciton-phonon coupling promote lattice distortions leading to the formation of these states that exist within the band gap.<sup>1</sup> Energy transfer pathways allow photo-excited states to undergo fast relaxation to ensembles of STEs, resulting in broadband emission in the visible spectrum with possible applications in wide band light sources, such as white light LEDs. [92] The broadband emission of these ensembles of STEs can be seen in our  $Ea_2PbBr_4$  samples emission in Fig. 4.2 A, where the lower energy peaks in the spectra are attributed to ensemble STE emission.

## 4.3 Manganese Doping in 2D Perovskites

Doping in 2DLPs, specifically substituting  $Mn^{2+}$  for  $Pb^{2+}$  in the octahedra, results in further improvements to their optoelectronic properties. [18,94] The strong interactions between the quantum confined host carriers and the dopants lead to efficient energy transfer (ET) [95] and increased PLQY, at both the band edge and the visible region through  $Mn^{2+}$  emission [96,97] setting the stage for high efficiency, dual-colored LEDs [41,98]. Despite these improved qualities, the underlying ET mechanisms are not completely understood, although various routes have been proposed, including transfers assisted through STEs [99], defect-related trap states within the band gap [99], and hot excitons. [100] Insights into the roles played by these competitive ET pathways will pave the way for improved material design thus enhancing light emission properties. They may also provide new avenues of research, such as optically manipulated magnetization [101–105] as observed in Mn-doped II-VI nanostructures.

<sup>1</sup>STE's differ from polarons in that while a polaron does create a lattice distortion, the photon - phonon interaction is strong enough in 2-D halide materials that the excitation is trapped by the resulting lattice distortion and is accompanied by new covalent bonds only possible while in the excited states.

## 4.4 Authors Work: Mn Doped 2DLP Energy Transfer Dynamics

In this work  $Mn^{2+}$  doped ethyl ammonium lead bromide  $Ea_2PbBr_4 : Mn^{2+}$  were studied, to investigate the role of STEs in host-to-dopant ET in the temperature range 20 K - 100 K. Focus was placed on this regime because even though activation energies of various ET pathways have been extrapolated to be a few meVs [99], measurements have largely been carried out above their corresponding thermal scale. Consistent with previous reports, this work confirms that for temperature  $T > 100$  K, PL only consists of  $Mn^{2+}$  emission [100]. However, for  $T < 100$  K, 2DLP excitonic emission as well as the STE emission is observed, accompanied by reduced  $Mn^{2+}$  PL, indicating a complex pathway different from the ones previously reported, dominated by ET from 2DLP to  $Mn^{2+}$  dopants via STEs. This process involves a very low potential barrier, whose magnitude is dependent on the doping concentration, and at higher  $Mn^{2+}$  concentration, higher activation energies indicate defect states come into play, successfully competing with STEs for ET both from the band edge to STE states, and from STE to  $Mn^{2+}$ .

### 4.4.1 Materials and Synthesis

2DLP  $EA_2PbBr_4 : Mn^{2+}$  systems were synthesized following a previously reported method. [99] Herein, 2D single-layered  $EA_2PbBr_4$  were fabricated via antisolvent precipitation. The samples for this work were synthesized by, taking  $PbBr_2$  (0.10 mmol) and EABr (0.30 mmol) dissolved into 200  $\mu$ L DMF to make the precursor ink. Then, the precursor ink was added to 10 mL of toluene under vigorous stirring. The DMF rejects the toluene and the constituents dissolved within form crystals. The crystals were separated with centrifugation at 6000 rpm for 5 min and washed once with toluene under sonication. At last, the powder was collected by centrifugation and dried in a vacuum oven (60 °C) overnight.

Similar to a standard undoped system,  $Ea_2PbBr_4 : Mn^{2+}$  is almost the same as that of undoped  $EA_2PbBr_4$  except replacing the desired amount of  $PbBr_2$  with  $MnBr_2$ . For doped  $Ea_2PbBr_4 : Mn^{2+}$ , the final molar ratio is given by equation 4.1. [99]

$$n_{EABr} / (n_{PbBr_2} + n_{Mn^{2+}Br_2}) \quad (4.1)$$

2DLPs doped with two different concentrations of  $Mn^{2+}$  (2% and 7%) were used, chosen based on the highest quantum yield enhancements when compared to the undoped samples. The ratios of constituents used are shown in Table 4.1.

For example, for the synthesis of  $EA_2PbBr_4 : 2\%Mn^{2+}$ , 0.30 mmol EABr mixed with 0.095 mmol  $PbBr_2$  and 0.005 mmol  $MnBr_2$  were dissolved in 200  $\mu$ L DMF, the

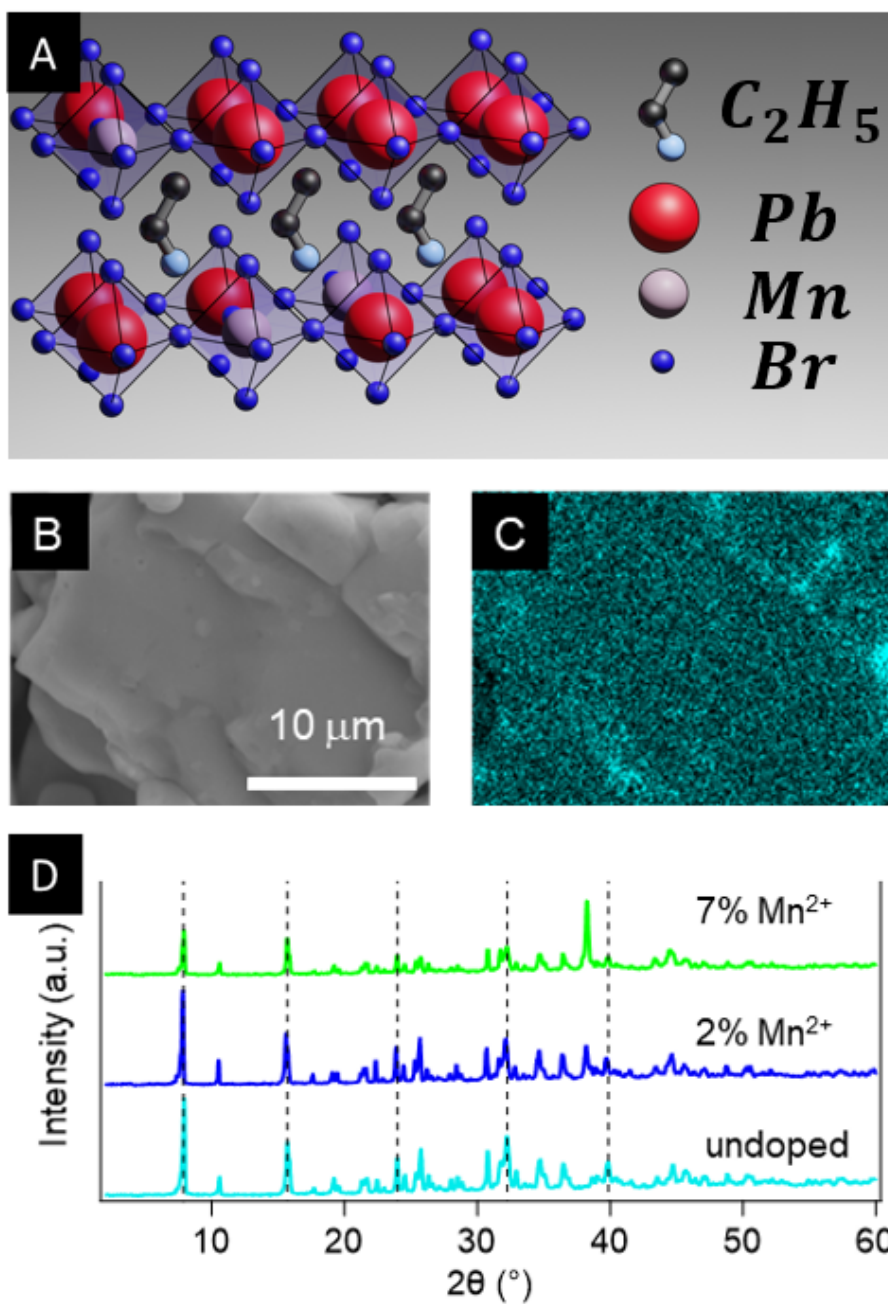


Figure 4.3:  $C_2H_5PbBr_4 : Mn^{2+}$  Sample Structure A: Schematic of  $C_2H_5PbBr_4$  with  $Mn^{2+}$  dopants substituting for  $Pb^{2+}$ . B: SEM image of  $EA_2PbBr_4:Mn^{2+}$  C: EDS mapping of  $Mn^{2+}$  showing uniform dopant distribution within the SEM image. D: Powder X-ray diffraction (PXR) of  $C_2H_5PbBr_4$  with different  $Mn^{2+}$  dopant concentrations.

Sample	Molar Feed Ratio ( $MnBr_2/PbBr_2$ )	% $Pb^{2+}$ Content	% $Pb^{2+}$ Error	% $Mn^{2+}$ Content	% $Mn^{2+}$ Error
Pure $EA_2PbBr_4$	0/1	100	6	0	0
$Ea_2PbBr_4 : Mn^{2+}$ 2%	1/19	98	5	1.8	0.1
$Ea_2PbBr_4 : Mn^{2+}$ 7%	1/9	93	5	7.2	0.3

Table 4.1: **Doping concentrations of  $Mn^{2+}$**  Relative to the sum of  $Pb^{2+}$  and  $Mn^{2+}$  ion content, of undoped and Mn-doped  $EA_2PbBr_4$  with differing molar ratios of Mn/Pb. Measurement were made using ICP-OES.

following procedure is the same to that of pure  $EA_2PbBr_4$ . Fig. 4.3 A, is a schematic of the 2DLP crystal, where the Pb-Br octahedra form the layers, connected through the ethyl ammonium chains. Here, however,  $Mn^{2+}$  substitutes for  $Pb^{2+}$  in the planes. Fig. 4.3 B shows the morphological characteristic of the 2DLP using scanning electron microscopy (SEM), where uniformly folded and layered structures, indicative of the 2D nature can be observed. Using energy dispersive spectroscopy (EDS), shown in Figure 4.3 C, the uniform and continuous distribution of  $Mn^{2+}$  throughout the 2DLP structure was confirmed.

#### 4.4.2 Room Temperature Dynamics

Room temperature photoluminescence (PL) spectra, shown in Fig. 4.4, demonstrates efficient incorporation of the  $Mn^{2+}$  dopants with strong emission centered around 610 nm from the d-d spin forbidden transition of the 5d energy levels ( ${}^4T \rightarrow {}^6A$ ), and as expected, no other emission is observed. The absence of any PL from the band-edge confirms the uninhibited energy transfer between the host and the dopant ions. It is also interesting to note the absence of PL from STE states, an optical characteristic of undoped 2DLPs, is attributed [99] to an ET pathway between the 2DLP and the dopants occurring through the formation of intermediate trap sites on the picosecond scale.

#### 4.4.3 Cryogenic Photodynamics

PL emissions between 20 – 100 K in two different samples with 2% and 7% doping, where the numerical values are representative of the Mn precursor added in the synthesis step, are discussed next. Fig. 4.5 A and B are maps of the PL intensity of the 2% and 7%  $Ea_2PbBr_4 : Mn^{2+}$  samples respectively, plotted with temperature  $T$  and emission wavelength  $\lambda$ . The direct bandgap emission from excitonic recombination at the band edge (BE) is visible around 405 nm (dashed arrow). Between 20 K – 100 K, a side band emission in the region 550 – 600 nm is also observed (solid arrow), arising due to STE emission. This band disappears by  $T = 100$  K for both doping

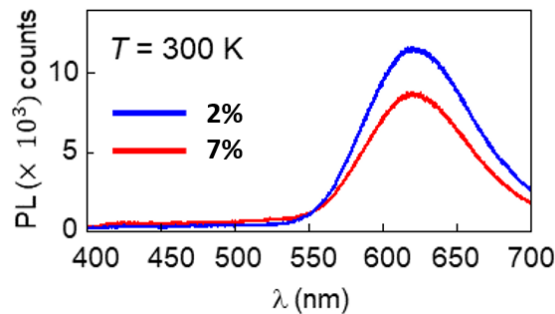


Figure 4.4: **Room Temperature  $\text{C}_2\text{H}_5\text{PbBr}_4 : \text{Mn}^{2+}$  Photoluminescence** PL emission from the 2% and 7% Mn Doped 2DPL samples at room temperature.

concentrations and does not re-emerge all the way to room temperature. The PL spectrum at  $T = 30$  K, in Fig. 4.5 C, highlights the three distinct regions showing emission corresponding to the direct BE, the side band from STEs, and the  $\text{Mn}^{2+}$  dopants.

Also shown are the fits to these separate bands from which we extract the emission peak  $\lambda_{Peak}$  and the integrated intensity  $I_{PL}$  plotted in the following panels in Fig. 4.5. In Fig. 4.5 C  $\lambda_{Peak}$  shows a red-shift with increasing  $T$  for both 2% (solid symbols) and 7% (hollow symbols) samples. OMHP semiconductors emission, in the bulk and low dimensional variants, typically blue-shift with increasing  $T$ , arising from the ‘inverted’ arrangements of the conduction and valence bands. For layered structures, spectral shift with  $T$  is dependent on the value of  $n$ , the number of inorganic layers between the organic cations, and red-shift is indicative of  $n = 1.16$ . In comparison the following panels in Fig 4.5 D,  $\text{Mn}^{2+}$  emission red-shifts with decreasing  $T$ , which has been attributed to enhanced ligand field strength due to the contraction of the octahedra as per earlier reports. [106] STE emission follows the same trend as  $\text{Mn}^{2+}$ , possibly due to the spectral overlap of the two bands.

#### 4.4.4 Energy Transfer Dynamics Calculations

The spectral shifts mostly confirm expected results, but the PL intensity  $I_{PL}$  of the BE, STE, and  $\text{Mn}^{2+}$  emission bands plotted in Fig. 4.6 D, E and F respectively, offer important insights into the ET pathways. Contributions from both BE and STE  $I_{PL}$  decrease with increasing  $T$ , while that of  $\text{Mn}^{2+}$  concurrently increases. From this correlation, it is evident that the relative increase in the Mn dopant emission occurs through ET from both the STE band and directly from the BE. Consequently, ET for  $T < 100$  K can be modeled as consisting of two pathways:

1. one allowing direct ET from the band edge to the  $\text{Mn}^{2+}$  band

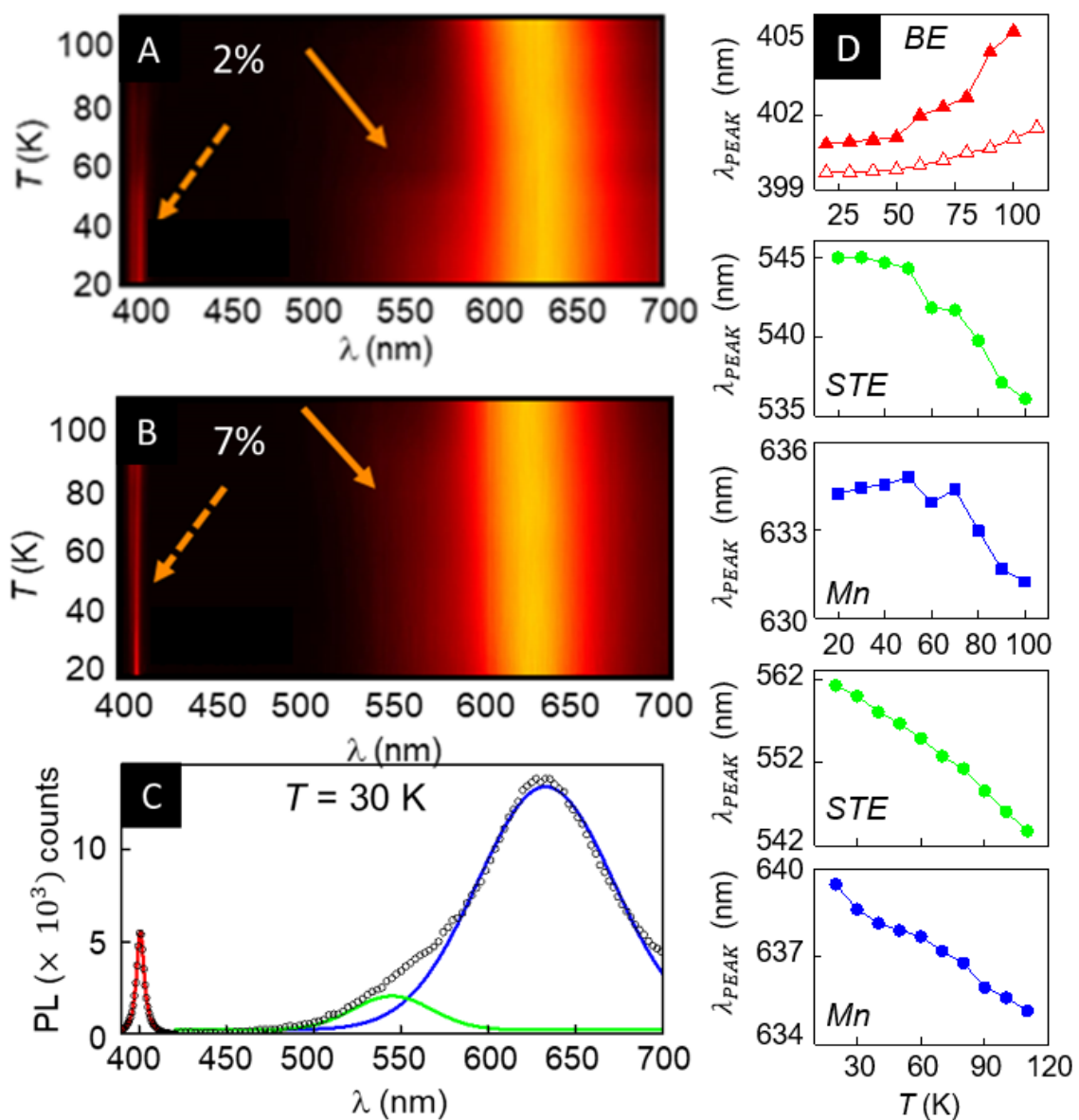


Figure 4.5: **Temperature Dependent  $C_2H_5PbBr_4 : Mn^{2+}$  Photoluminescence**  
 A/B: Temperature dependent PL Map for the 2% and 7% Mn Doped 2DLP Samples.  
 C: PL Spectra of the same sample at 30 K showing the Band Edge emission (red), the self trapped exaction's (green), and the  $Mn^{2+}$  emission (blue).  
 D: In descending order  $\rightarrow$  Movement of Band Edge (red) peak with temperature (Solid 2%, hollow 7%). Movement of 2% doped 2DLP STE (Green) followed by Mn(Blue). Then Movement of 10% doped 2DLP of STE followed by Mn.



2. the second allowing ET to the  $Mn^{2+}$  band through STEs

A simple representation of this is shown in Fig. 4.6 A,  $k_1$  is the transfer rate from the band edge to the STEs per excited charge carrier,  $k_2$  is the transfer rate constant from BE to the dopant energy levels and  $k_3$  is the energy transfer rate constant from the STE band to the dopants.

Several relations can be extracted between these rates. Beginning with the relaxation dynamics of the excited state carriers in the BE using time-resolved photoluminescence (TRPL). The corresponding average lifetimes extracted using a double exponential fit to TRPL data, Fig. 4.6 B, is around 230 ns for the entire range of  $20\text{ K} < T < 100\text{ K}$ , Fig. 4.6. Such a short recombination lifetime is a result of the heavy atom effect observed in chloride-based perovskites, along with the concurrent energy transfer to the STE and  $Mn^{2+}$  energy bands. The average recombination rate  $k_{Tot}$  between 20 – 100 K, determined from TRPL curves is  $43 \times 10^8 s^{-1}$  and can be expressed as:

$$k_{Tot} = k_{exc} + k_1 + k_2 \quad (4.2)$$

Where  $k_{exc}$  is the direct recombination rate per exciton. Now, assuming negligible non-radiative recombination due to the high quantum efficiency in 2DLP, we get,

$$k_1 N_{BE} - k_3 N_{STE} \propto N_{STE} \quad (4.3)$$

$$k_2 N_{BE} - k_3 N_{STE} \propto N_{Mn} \quad (4.4)$$

where  $N_{BE}$ ,  $N_{STE}$ , and  $N_{Mn}$  represent the integrated charge carrier density of the BE, STE, and Mn bands, respectively. Solving the above, we get

$$k_1 + k_2 \propto \frac{N_{STE} + N_{Mn}}{N_{Be}} \quad (4.5)$$

Following the same logic for energy transfer to Mn dopant from BE and STE, we get,

$$k_1 N_{BE} = A * N_{STE} + k_3 N_{STE} \quad (4.6)$$

From eq. 4.6 we get,

$$\frac{A_1 + k_3}{k_1} = \frac{N_{BE}}{N_{STE}} \quad (4.7)$$

and each of the rates can be expressed using the well-known Arrhenius equation

$$k_{1,2,3} = a_{1,2,3} e^{\frac{\Delta E_{1,2,3}}{k_b T}} \quad (4.8)$$

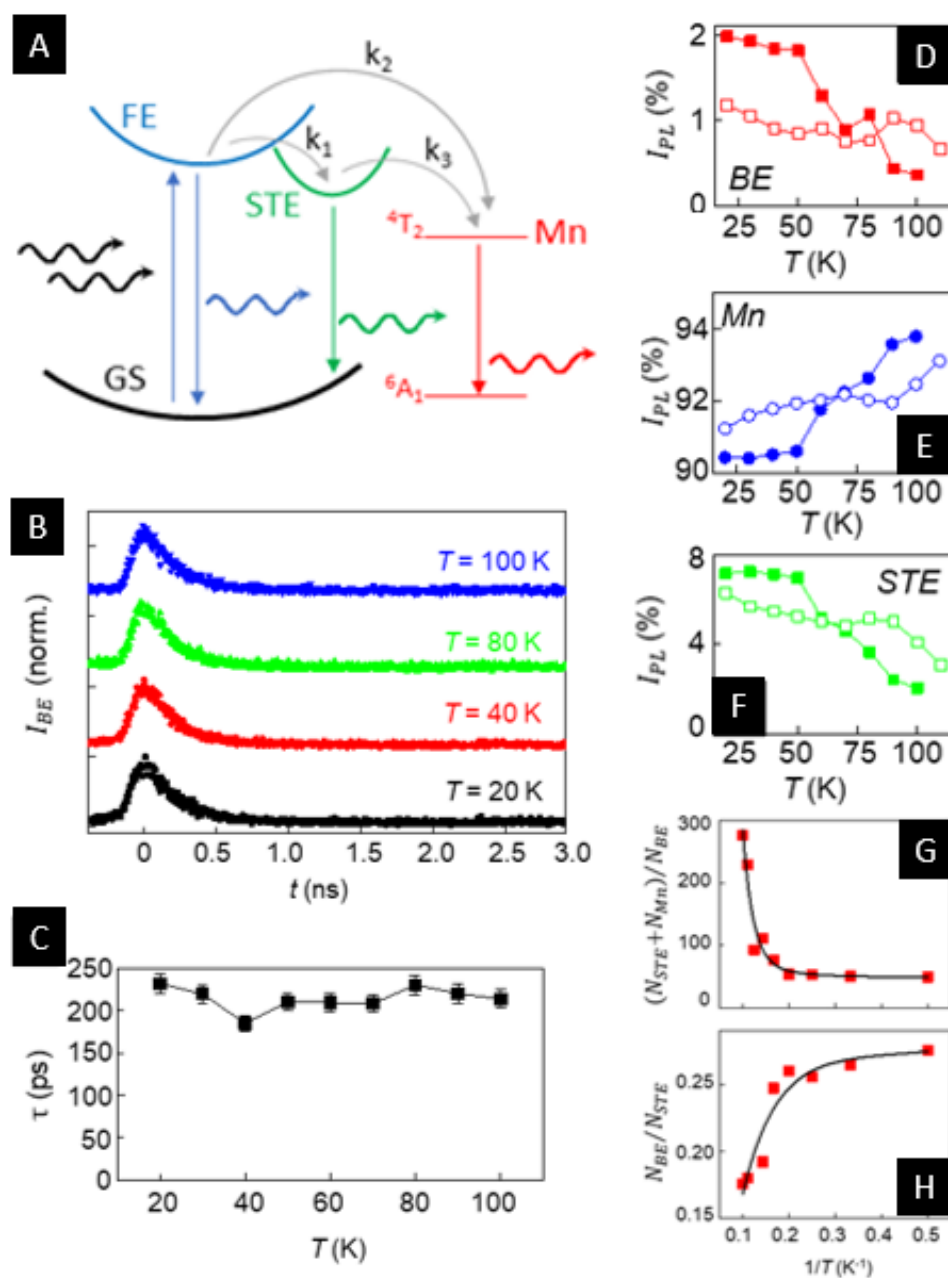


Figure 4.6: **Temperature Dependent Mn Doped 2DLP TRPL and PL Intensity Trends** A: Graphic of energy transfer dynamics in the  $C_2H_5PbBr_4 : Mn^{2+}$  2DIP samples. B/C: TRPL spectra / extracted single exponential lifetimes with temperature. D/E/F: PL intensity trends of  $C_2H_5PbBr_4 : Mn^{2+}$  2DIP samples with temperature. (Solid 2%, hollow 7%) G/H: Plots fit with eq. 4.4 and eq. 4.6 to extract activation energies.

Doping Concentration	$\Delta E_1$	$\Delta E_2$	$\Delta E_3$
2%	8.8 meV	39 meV	4 meV
7%	12 meV	31 meV	2 meV

Table 4.2: **Activation Energies** Activation energies extracted from population fits.

where  $\Delta E_{1,2,3}$  is the activation energy corresponding to  $k_1, k_2, k_3$  respectively, and  $K_B$ , the Boltzmann constant.

Using the equivalence that the integrated charge carrier densities are proportional to the integrated PL intensities, the ratios  $N_{STE}/N_{Mn}$  and  $N_{BE}/N_{STE}$  varying with  $1/T$  are plotted in Fig. 4.6 G and H and fit the data using Eq. 4.4 and Eq. 4.6, respectively. From the fits, we derive the activation energies for the various energy transfer routes. Their values are summarized in Table 4.2 and from these, we can make the following points.

The activation energies  $\Delta E_1$  and  $\Delta E_2$  relate to ET from the BE, and given that the quantitative values correspond to thermal scales  $\geq 100$  K, it explains why no change in the excitonic recombination times over the range 20 K – 100 K is observed. Further, the same scale set by  $\Delta E_1$  is the reason why BE emission quenches around  $T \approx 120$  K for both doping levels, as seen in Fig. 3D.  $\Delta E_2 \gg K_B T$  for not only the temperature range of these measurements but even at ambient temperatures, so it can be concluded with certainty that there is a negligible direct energy transfer from the BE to the dopants. The main ET route is therefore from  $BE \rightarrow STE$  followed by  $STE \rightarrow Mn^{2+}$ . Comparing the activation values for the two different doping levels reveals additional insights.  $\Delta E_2$  is lower for the sample with higher doping, while  $\Delta_1$  increases. This possibly results in a slightly larger proportion of direct ET from  $BE \rightarrow Mn^{2+}$ , but these changes in activation energies are not large enough to make ET from  $BE \rightarrow Mn^{2+}$  the predominant pathway. Further, the data in Fig. 2D and 2E also show that the relative contributions of BE and STE PL are smaller in the 7% sample, to begin with, and vary less with T, possibly due to the substantially low value of  $\Delta E_3$  in the 7% doped sample, which is comparable to the thermal energy even at temperatures as low as 20 K. These changes in the activation energy possibly arise from the larger distribution of trap states in the sample with larger doping owing to greater lattice distortion from the size mismatch between Pb and Mn ions, as well as from the higher density of doping-related defects states.

## 4.5 Spin Dynamics

Lastly, the focus is placed on different aspects of transition metal dopants such as  $Mn^{2+}$  in semiconductors beyond their roles related to luminescence. Strong sp-d exchange coupling between these discrete magnetic moments and the host carriers,

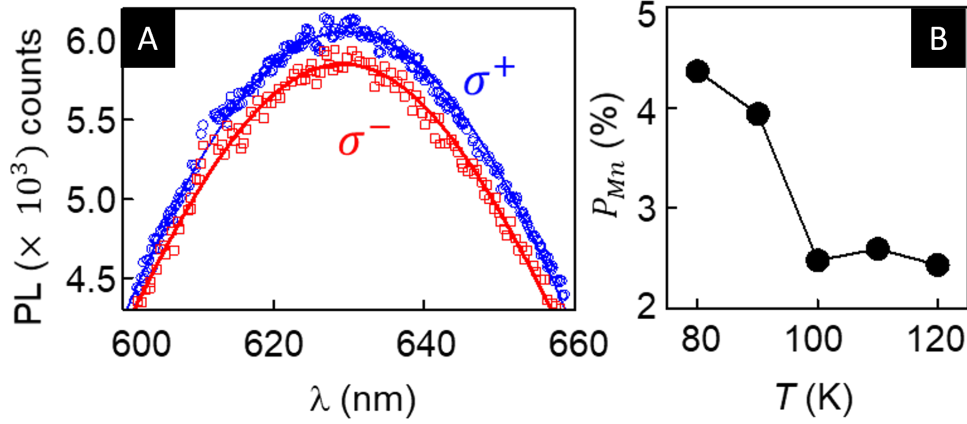


Figure 4.7: **Polarisation Dependent Spectroscopy** A: Left (Red) and right (Blue) circularly polarized emission from  $Mn^{2+}$  dopants. B: Total polarisation of  $Mn^{2+}$  emission as a function of temperature.

particularly in quantum confined structures, allow magneto-optical modulations that can lead to magnetic polarons, giant Zeeman effect, and carrier-mediated ferromagnetism [107,108], which in turn drive applications ranging from spin-filtering [109] to magneto-optical gating [110] and quantum information processing [111,112]. While most of these exciting properties have been investigated in II-VI and III-V materials, the high spin-orbit coupling (SOC) in OMHPs indicates these class of compounds have considerable potential as candidates for similar phenomena [113,114], where strong SOC allows the bright host exciton with  $\Delta J \pm 1$  to populate the lowest spin state in  $Mn^{2+}$  ions [115]. Using polarization-resolved spectroscopy, spin-polarized  $Mn^{2+}$  emission in the absence of an external magnetic field in the 2DLPs is demonstrated.

On exiting the 2DLP using left circular polarized light (designated  $\sigma^-$ ) at 380 nm, and analyzing the  $Mn^{2+}$  emission centered at 610 nm using circular polarization spectroscopy, a 4% right circular polarization ( $\sigma^+$ ) at  $T = 80$  K is observed, shown in Fig. 4.7 A. Note the  $Mn^{2+}$  emission is polarized opposite to that of the excitation light. The polarization value  $P_{Mn}$  drops to 2.4% by  $T = 120$  K, plotted in Fig. 4.7 B, and the fact that it persists this far implies the ET rate is faster than the spin dephasing rate. The origin of this polarized emission is not the same as that in diluted magnetic semiconductor nanocrystals, where similar spin-polarized emission has been observed in a high magnetic field [114]. While the exact mechanism behind this spin-polarized emission is not fully understood yet, one possibility is the exchange interaction between the excited  $Mn^{2+}$  d-electron spins and optically injected sp-exciton spins. Theoretical studies have shown that off-diagonal terms in the sp-d exchange interaction term can facilitate simultaneous spin-flips and spin transfer in Mn-doped OMHPs [116,117], and further investigations following these initial results

will undoubtedly allow insights into the detailed nature of these observations.

## 4.6 Conclusion

In conclusion, while doping is a very powerful tool for tuning functionalities in semiconductors, ranging from 3D to all other low-dimensional variants, OMHPs are relatively new entrants in this arena, and their properties are still in the process of being characterized to the full extent. In this context, our findings clarify significant aspects of energy transfer in doped 2D OMHP compounds, establishing the central role played by self-trapped excitons. STEs are emissive at low temperatures and are the main route of ET from the band edge to the dopants, while there is almost no ET directly from the band edges to the  $Mn^{2+}$  ions, which is also supported by relative magnitudes of the activation energies derived from spectral analysis. Varying the dopant concentration influences these energies and consequently, enhance ET from STEs to the dopants. However, despite the negligible direct ET from the band edge excitons to  $Mn^{2+}$ , the host-dopant exchange interaction is strong enough to allow optically polarizing of the dopant spins via band gap excitation. This is a most exciting observation, indicating the possibility of harnessing spin-charge couplings and tunable magneto-optical effects in OMHPs.

# Chapter 5

## Zero Dimensional Colloidal Perovskite Quantum Dots

The main drawback to wide-spread commercialization is perovskite thin-film stability in ambient conditions, chemically degrading under exposure to heat, moisture, and oxygen in a matter of hours to days. [71, 118–122] A possible pathway to perovskite stabilization comes in the form of PQDs. These PQDs retain the composition-based tunability of the thin film perovskites with the addition of size-controlled bandgap tunability. [123, 124] This reduction in size and dimensionality results in an increase in the surface-to-volume ratio of the perovskites, allowing the direct study of their surface interactions, often leading to a better understanding of bulk mechanics. In addition, these PQDs are more stable than the perovskite thin films due to the coating of functionalizing ligands on the PQD surface that help block exposure of the perovskite core to moisture and oxygen. [125] While a perovskite thin film will become fully non-emissive in only hours to days in ambient conditions, a PQD sample will remain emissive for months to years depending on the stabilizing properties of the PQD's functionalizing ligands. [8, 13, 125]

### 5.1 Effect of Quantum Confinement

Traditionally Quantum Dots are semiconductor nanoparticles whose diameter approaches the bohr radius of the semiconductor material. This causes quantum confinement of the electronic energy levels of the system leading to optical and electronic properties separate from that of the bulk material. This confinement works in the same way as an infinite square well example, from intro quantum mechanics.

## 5.2 Effect of Ligands

The primary purposes of a ligand in conjunction with colloidal QD systems are to:

1. Surface Passivisation
2. Controlled Growth
3. Surface Energy Manipulations

### 5.2.1 Surface Passivisation

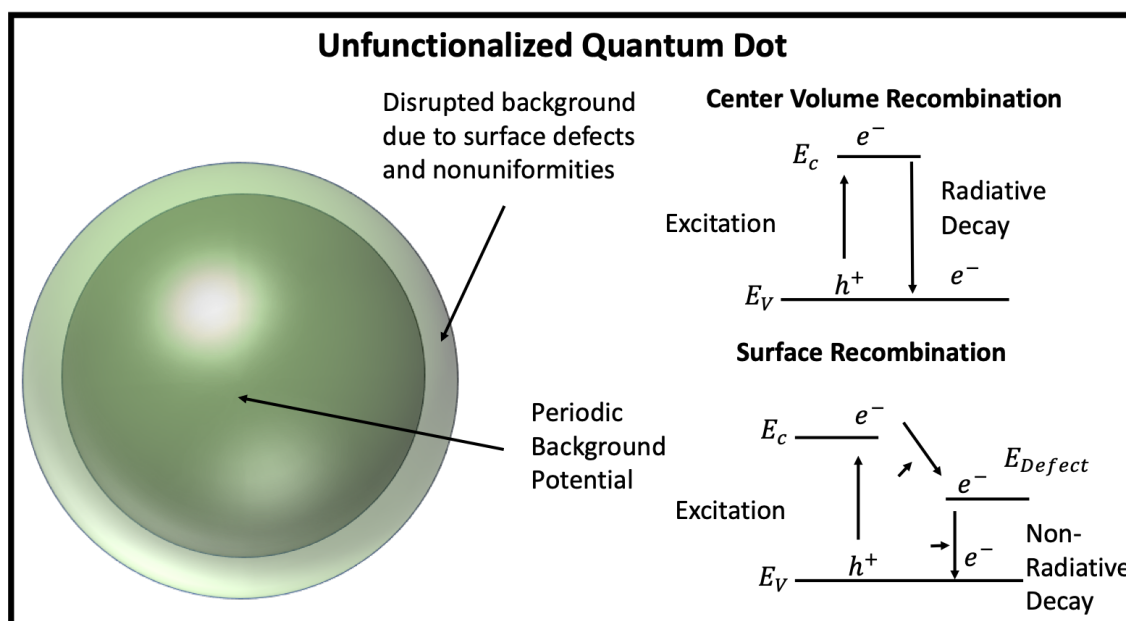


Figure 5.1: **Quantum Dot Dynamics** Cartoon depiction of an unfunctionalized Quantum Dots and the accompanying states on the Left and a depiction of the effect on surface potential of Quantum Dots.

A basic QD with no ligands or an unfunctionalized QD can be broken down into two separate regions, the center volume and the surface volume. In the center volume of the QD, Shown in Fig. 5.1, there exists a periodic background potential with, in an ideal case, no defects to subtract from radiative recombination. However, at the surface, the sudden abrupt termination of the periodic potential induces surface defects which cause trap states. As shown in Fig. 5.1 these surface defects act as favorable nonradiative recombination routes for excited electrons. When a QD functionalizes onto the surface it has an effect on the local background potential near

the connection site and will remove that defect energy level, thus passivating that surface trap state.

### Measuring Passivation

Measuring the Optical Quantum Yield of a QD system, in solution is normally an accepted measure of determining how well passivated your QD surface is. Quantum yield is a measure of how many photons are emitted divided by how many photons are absorbed, as shown in Equation 5.3.

$$QY = \frac{PhotonsEmitted}{PhotonsAbsorbed} \quad (5.1)$$

### 5.2.2 Controlled Growth

The ligands themselves impact the PQD size by altering synthesis conditions and the PQD's core surface energy. Size and thus band gap-controlled synthesis of PQDs has been demonstrated by altering the concentration of (3-Aminopropyl)triethoxysilane (APTES) ligand used during synthesis. [126]

### 5.2.3 Surface Energy Manipulations

In addition, Ghosh and group have previously demonstrated the abilities of certain ligands like APTES to arrest our organic  $CH_3NH_3PbBr_3$  PQDs tetragonal to orthorhombic phase transition below 110 Kelvin by significantly altering the PQDs surface energy. [30] Swarnkar et. al. recently demonstrated that stabilizing the  $\alpha$  - crystal cubic phase in their inorganic  $CsPbI_3$  PQDs significantly increased their effectiveness as room temperature stable photovoltaic cells. [127] This is because perovskite's most appealing PV and LED absorption/emission properties exist in its cubic phase. The stabilization of our organic APTES functionalized PQDs cubic phase at low temperatures has made them a stronger candidate for low-temperature optoelectronic applications such as space-based photovoltaics however, there are still hurdles to overcome.

## 5.3 Authors Work: Effect of Conductive Ligands on PQD Properties

While alkoxy silane ligands like APTES have proven to control both the size and surface energy of organic PQDs while also maintaining high stability, [126] the main drawback to using long-chain saturated hydrocarbons and alkoxy silanes like APTES is that as insulating ligands they confine the PQDs electron wavefunction to within



the PQD. This severely limits the charge transfer capabilities of an APTES-PQD-based device, thus limiting their effectiveness for applications in photovoltaics or light-emitting diode devices.

Recent steps have been taken investigating the use of hybridization of Aromatic capping ligands in conjunction with olic acid ligands to both stabilize and increase inter-QD charge transfer and have demonstrated promising results. [20, 128] Herein is an in-depth study of the hybridization of two different conducting capping ligands: Benzoic acid (BA) and Phenylacetic Acid (PAA) with Benzylamine (BZA) and Iso-propylbenzylamine (IPBZA) is presented. It is demonstrated through concentration-dependent photoluminescence (PL) and time-resolved photoluminescence (TRPL) spectroscopy that while BA as a fully conjugated capping ligand is the most conductive, PAA outperforms BA at lower concentrations making it a strong candidate for photovoltaic or LED applications. In addition through temperature-dependent spectroscopy, it is shown that 4 different combinations of ligands, BZA-BA, BZA-PAA, IPBZA-BA, and IPBZA-PAA arrest the tetragonal to orthorhombic phase change at low temperatures and that the ligands involved play important roles in affecting the PQDs' lifetimes with temperature. Also, we uncover a possible connection between increased room temperature QY and a decrease in defect states at cryogenic temperatures.

### 5.3.1 Materials and Synthesis

Methylammonium lead bromide quantum dots ( $CH_3NH_3PbBr_3$ ) PQDs were synthesized following a previously reported procedure with the addition of the previously mentioned aromatic ligands. [129, 130] A precursor solution consisting of  $PbBr_2$ , MABr, BZA or IPBZA, and BA or PPA dissolved in N, N-dimethylformamide (DMF) was injected into toluene. The colloidal (BZA/IPBZA)-(BA/PAA)-MAPbBr<sub>3</sub> QD solution was then purified using centrifugation and cotton-plug filtration. Optimization of PQDs with the highest QY was determined by adjusting BZA/IPBZAA and BA/PAA concentrations discretely. Concentrations used were 1:10 for BZA-BA and BZA-PAA and 1:4 for IPBZA-BA and IPBZA-PAA. A schematic of each resulting species, BZA-BA, BZA-PAA, IPBZA-BA, and IPBZA-PAA is shown in Fig. 5.3 with an average diameter of each PQD being 6nm. [128] Combinations of the capping ligands BZA and IPBZA with the acids BA and PAA were used to promote electron donation from the acid to the capping ligand. This leaves the positively charged acid to bind to negative sights on the perovskite while the now negatively charged capping ligand binds to positively charged sights on the perovskite.

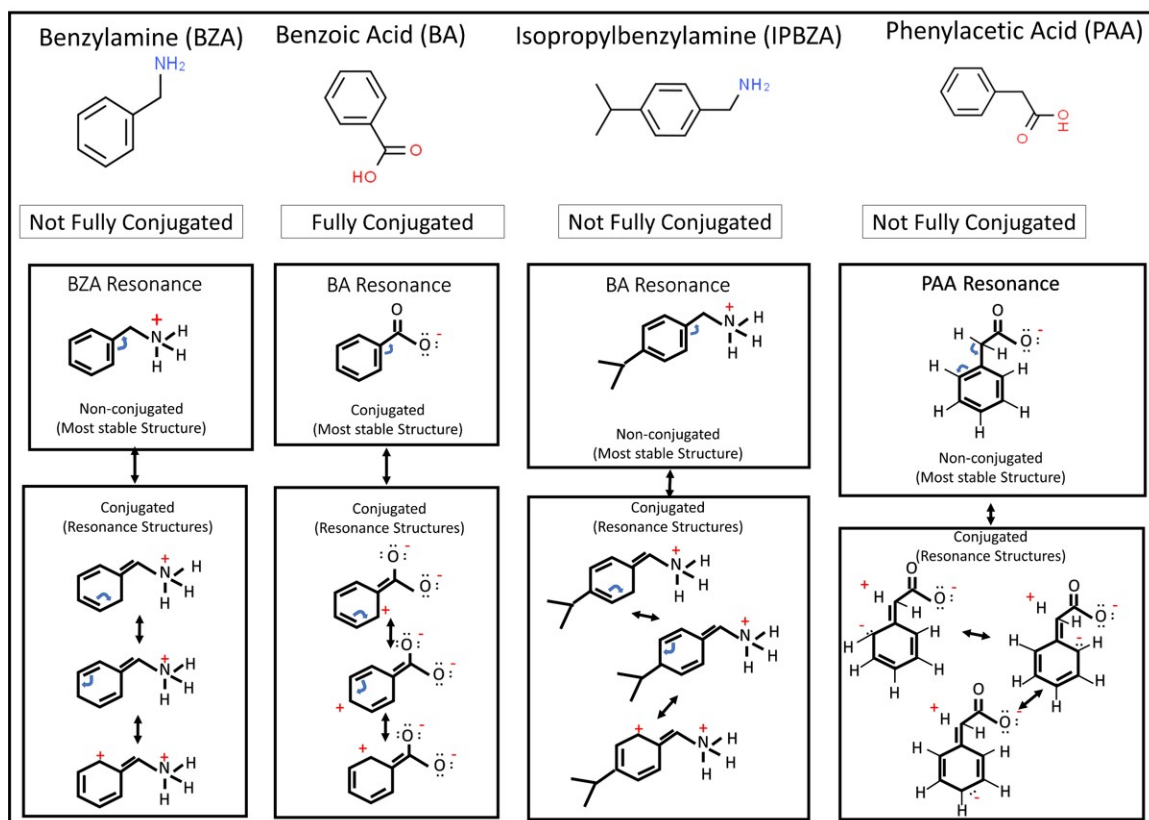


Figure 5.2: PQD Species Room Temperature Characteristics.

### 5.3.2 Ligand Dynamics

In this study aromatics ligands, benzylamine (BZA), Isopropylbenzylamine (IPBZA), benzoic acid (BA), and polyphosphoric acid (PPA) ligands, shown in Fig. 5.2 are used to increase the conductivity of our organo-metal halide PQD films. All these aromatic ligands are all to some degree conducting but each has relative differences between them based on whether the ligand itself is conjugated. An aromatic ligand is considered most conductive when it is fully conjugated, meaning the ligand contains alternating single and double bonds throughout the entire structure. These alternating single and double bonds within the aromatic ligand allow the delocalization of charges to the ligands' benzoic position, increasing conductivity through the ligand. In addition for a ligand to be fully conjugated all of its thermal resonance structures also must be conjugated, not just its most energetically favorable state. Fig. 5.2 displays the different ligand resonance structures for each ligand along with its most stable energy state below its base structure. BA exists as the only fully conjugated ligand in our batch with all its energy states being conjugated. BZA and PAA are partially conjugated with their lowest energy state being non-conjugated and their other 3 states being conjugated. IPBZA is fully not conjugated as non of its thermal resonance states are conjugated.

### 5.3.3 Room Temperature PL

The functionalization quality of each PQD species was identified using Quantum Yield (QY) measurements, discussed in more detail in 5.2.1 earlier in this chapter and in Appendix. QY is used to determine the number of photons a PQD emits divided by the number absorbed. Surface defects and nonuniformities during the PQD synthesis contribute to the increase in surface defects in the PQD electrical structure leading to nonradiative recombination. Such nonradiative recombination leads to decreases in LED or photovoltaic efficiencies. QY is used as a measure of how well each ligand passivates these trap states, the more passivated a quantum dot's surface is the higher the quantum yield. [3,131] QY measurements were performed on identically spin-coated PQD samples of all four different species. The samples were fabricated by dynamic drop-casting of 2mL of PQD solution at 5mol/L in toluene over 2 min spinning at 2000 RPM. A continuous-wave 405nm laser was used for excitation while an optical integrating sphere was used for collection. Each PQDs QY is shown in Fig. 5.3, inside the schematic diagram of each ligand structure, while their photoluminescent profiles are shown in Fig. 5.3 A, with the spectra offset by their relative QY intensity. Using solely QY as the metric, BZA-PAA appears to have the most surface states passivated while IPBZA-BA appears to have the least suggesting that both PAA and BZA outperform their counterpart's BA and IPBZA at passivating surface states during synthesis. The center wavelength and FWHM of

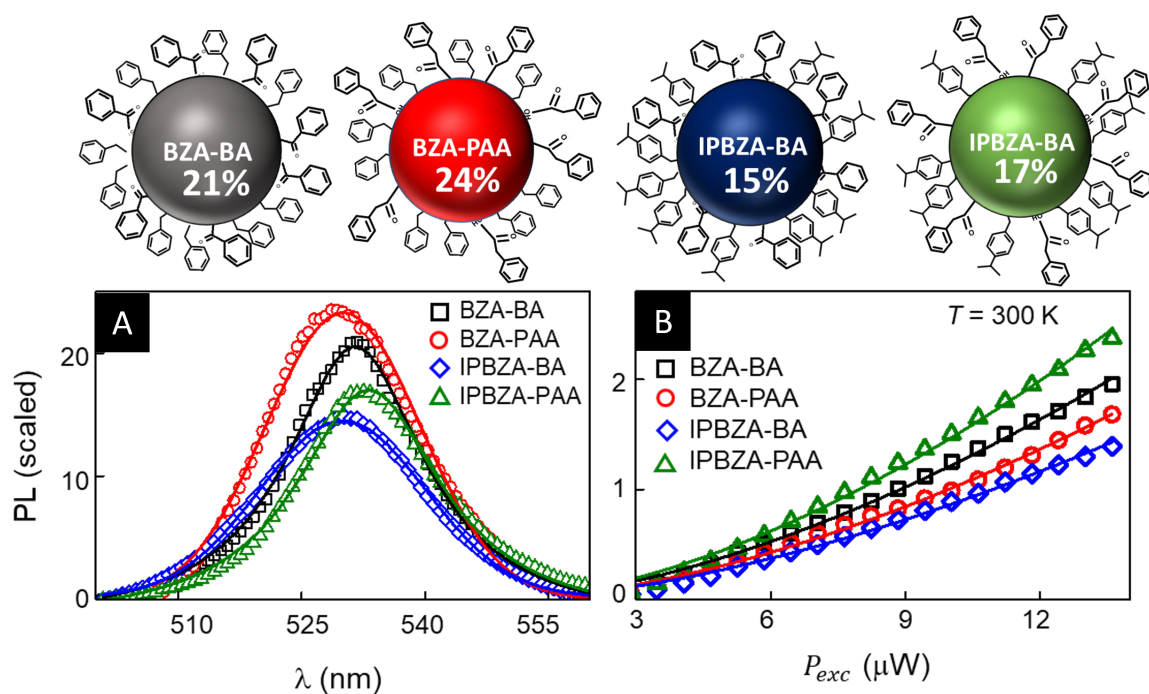


Figure 5.3: **PQD Species Room Temperature PL.** Upper Half: Displays the PQDs studied with their ligand combinations. The percentages inside the PQD – Ligand schematics are their optical quantum yields. A: Displays the PL spectra for each PQD species with the peaks offset to match their solid-state quantum yields. B: Displays the PDPL of each PQD species at room temperature.

each species, extracted using a single Gaussian fit are 531nm, 530nm, 530nm, and 533nm, and 85meV, 100meV, 110meV, and 87meV for BZA-BA, BZA-PAA, IPBZA-BA, and IPBZA-PAA respectively. The differences in center wavelength and FWHM are likely due to slight differences in their synthesis.

To further understand the effect the conducting ligands have on the PQDs, Power Dependent PL (PDPL) measurements were performed at room temperature with the results shown in Fig. 5.3 B. The resulting data fit with the power-law  $I_{PL} = aI_{ex}^K$  where  $a$  is a normalization constant and  $K$  is the power dependence. For a direct bandgap semiconductor, it is known that a  $K < 2$  signifies free charge carrier recombination and that  $K \leq 1$  signifies bound exciton recombination while  $2 < K < 1$  represents a mixture of both bound and free recombination. [30] The  $K$  values for our 4 PQD species were  $\approx 1.5$  signifying the existence of both free and bound recombination with the PQD film. We believe this result is unique as others have all reported linear or sub-linear power dependencies in the past for organic perovskite quantum dots. [30, 132]

### 5.3.4 Conductive Ligand's Effect on PQD Lifetime

It now becomes important to discuss to what degree these PQD species are conductive and what effect, this generation of free charges in the PQD ensembles has on the electronic lifetimes by comparing and contrasting the TRPL spectra of BZA-BA PQDs in solution and when spin-coated into a film on glass, shown in Fig. 5.4 A. These measurements were carried out in a traditional TRPL setup with a pulsed 430nm laser at a rep rate for 5.56 MHz for the grey curve and 77.7MHz for the red curve. When examining the long components of the double exponential fit for the TRPL data we observe a long lifetime of 46.9 nanoseconds (ns) while in solution but a short lifetime of 5.35 ns when spin-coated into a dense film. We believe this to be because when the PQDs are suspended in the toluene they exist in an infinite potential well state, that is there exists little to no interaction between the neighboring dots as the toluene acts as the infinite potential barrier. This allows the characterization of PQDs as an ensemble of isolated dots as compared to when in a spin-coated or drop cast film where interaction becomes possible. Thus when the PQDs are in the film they interact in the form of direct PQD to PQD electron transfer. This theory is further backed by no evidence of Foster Resonance Energy Transfer (FRET) as seen in Fig. 5.4 B/C. The measurement involves performing lifetime measurements on sections of the PL spectra using the addition of a monochromator before time-resolved collection. In our case, we have isolated sections of the curve between 520nm and 540nm going in 5 nm steps. If FRET was occurring within the film the variation in a lifetime from the short wavelength, 520nm to long-wavelength 540nm of the PL spectra would be on the order of the differences between the in solution and film lifetimes. Instead, we see an average lifetime change of 0.6 ns as we sweep from 520nm to 540nm showing

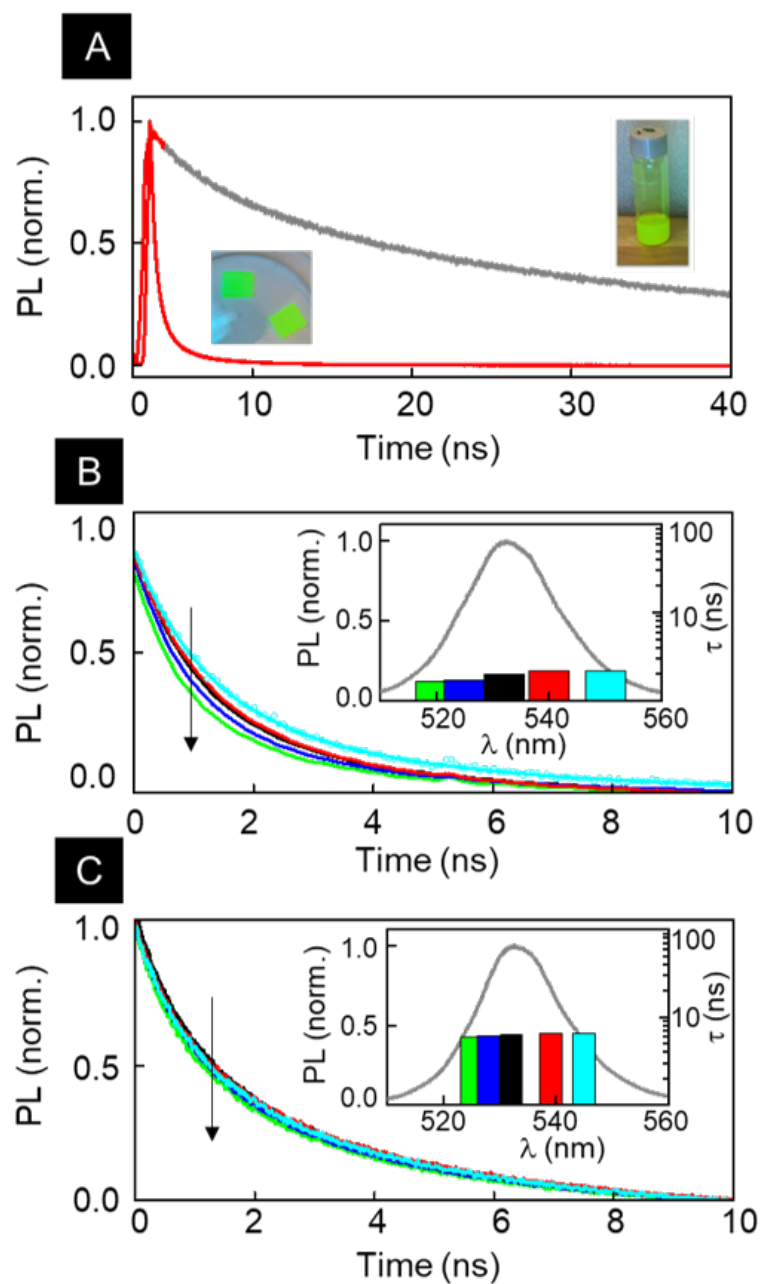


Figure 5.4: **PQD Species Room Temperature TRPL** A: TRPL Spectra for the BZA-BA PQD solution (Grey) and solid state thin film (Red), with insets of each displayed. Solid PQD films are 1/2" by 1/2" and PQD solution is a 1 1/2" tall 10  $\mu$ L vial. B/C: Spectrally Resolved TRPL for BZA-BA/IPBZA-PAA solid state thin films.

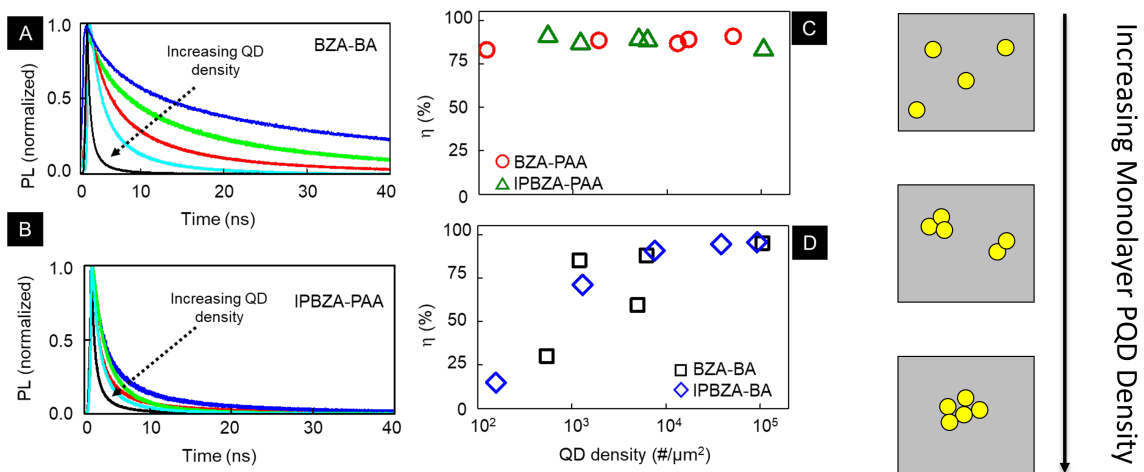


Figure 5.5: **PQD Charge Transfer** A/B: TRPL curves with increasing PQD density for BZA-BA/IPBZA-PAA. C/D: Calculated charge transfer efficiencies as a function of PQD density. Right: Diagram of increasing PQD density.

little to no evidence of FRET.

To further investigate these phenomena TRPL measurements were conducted on all four PQD species in solution and on 2uL drop cast films to facilitate a sample with spots of differing concentration. The resulting TRPL decay profiles for the BZA-BA and IPBZA-PAA species are shown in Fig. 5.5 a)-b). The Pink color curve signifies the in-solution lifetimes while the rest are at different spots in the sample in generally decreasing concentration, estimated using PL intensity. All curves were fit to a double exponential decay function where the short lifetime is  $\tau_1$  and the long component represents the  $\tau_2$ . The large 46 ns and 52 ns long lifetimes components of the solution versus the 5.3ns and 10ns long lifetime components of the most concentrated parts on the PQD films suggest that significant charge transfer is taking place. It appears the conducting aromatic ligands are encouraging inter quantum dot charge transfer, increasing as the concentration of PQDs increases. The BZA-BA species shows a strong lifetime dependence on concentration while the IPBZA-PAA species shows little dependence. To further analyze this difference in the PQD species charge interactions, the PQDs lifetimes were converted to arbitrary charge transfer efficiencies (E) through the equation 5.2

$$E = 1 - \tau_{Avg-Film} / \tau_{Avg-Solution} \quad (5.2)$$

Where  $\tau_{Avg-Film}$  and  $\tau_{Avg-Solution}$  are the average lifetimes of the TRPL curves in Fig. 5.5 A/B. The resulting charge transfer efficiencies are plotted in Fig. 5.5 C/D) as a function of PQD density. At high density, the BA species outperforms the PAA

species, likely due to the fact that BA is a fully conjugated ligand, whereas PAA is only partially conjugated. In addition, the species containing BA show a large change with concentration while the PAA species are uniform throughout almost all concentrations. We speculate this is due to the structure of the BA and PAA ligands. The BA ligand while more conductive is shorter than PAA and may have less overlap with BA ligands of other PQDs as the concentration decreases. It is possible that due to the PAA ligand having the additional hydrocarbon link and therefore being longer, it maintains better contact with other PAA ligands and thus maintains higher charge transfer efficiencies at lower concentrations.

### 5.3.5 Temperature Dependent Electronic Behaviour

To identify the differences in the PQD surface energy engendered by the different functionalizing ligands temperature-dependent PL measurements were performed from 290 Kelvin (K) to 20K in 10K increments. Fig. 5.6 A, displays the temperature-dependent spectra as a PL map. Both PL and TRPL measurements were done simultaneously with a power density of  $100 \text{ Watts}/m^2$  and a rep rate of 19.5 MHz. We start with the BZA-BA species and see that center wavelengths redshift with decreasing temperature, opposite to that of most known semiconductors. This difference is attributed to perovskites reversed band contributions [4], with a p dominant conduction and an s dominant valence band. [16] It is interesting to also note that from 290K to 90K a 40meV red-shift in energy is seen while from 90K to 20K a 100meV red-shift is seen.  $CH_3NH_3Br_3$  traditionally transitions from its  $\alpha$ -cubic phase to its tetragonal phase at approximately 220K [30] however due to the similarities in the two phases no difference is traditionally seen in the PL spectra. As  $CH_3NH_3Br_3$  continues to cool towards 20 K it will typically undergo a phase change at 110K from the tetragonal to orthorhombic crystal phase. As this change is significantly more drastic a change is seen in the PL spectra with a higher energy peak forming at 485nm. [30] However, no higher energy peak at 485nm was seen in our spectra however a shift in the slope of the wavelength change was seen at 90K. This suggests a full arresting of the orthorhombic phase in the BZA-BA species, similar to APTES in the previous study by our group. [30]

Next, the line shape of the PL spectra below 200 K are examined. In Fig. 5.6 B three waveform cuts from the PL map in Fig. 5.6 A are displayed. At 150K we observe a broad peak, similar to the room temperature peak. At 90 K a narrow Gaussian with a small lower energy tail starts to form. At 30 K this higher energy Gaussian forms completely. With this splitting of the Gaussian into two, it is not advised to use the traditional single Gaussian fit so instead a double Gaussian fit is used. The higher energy peak is dubbed "Main" while the larger FWHM peak is "Defect". Fig. 5.6 displays that both the main and defect peaks are redshifting with decreasing temperature. In Fig. 5.6 D the main peaks FWHM bottom out



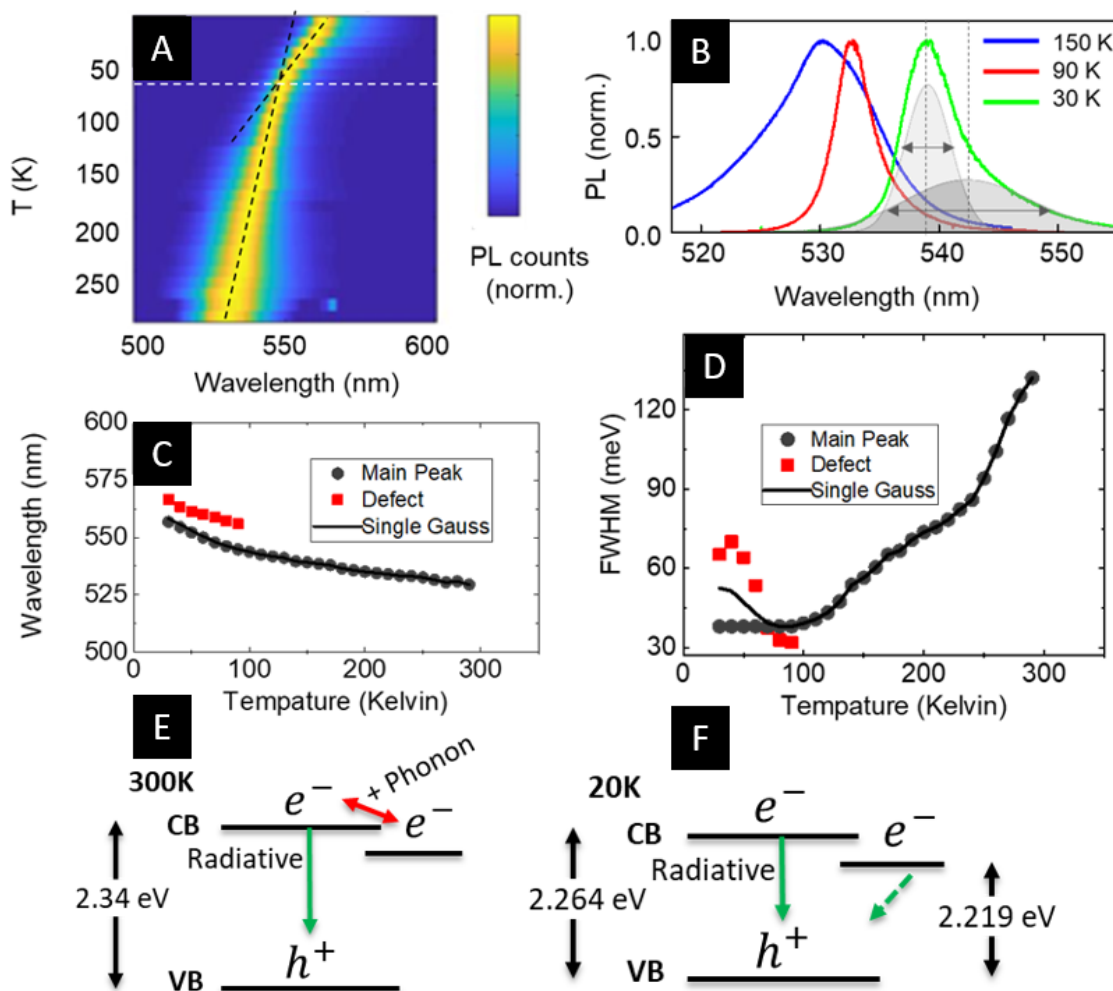


Figure 5.6: **Temperature Dependent PL** A: BAZ-BA PL map. B: Spectra of BZA-BA at 150K, 90K and 30K. C/D Energy and linewidth dynamics respectively. E/F: Energy diagram at 300K/20K.

while the defect peak continues to rise with decreasing temperature. *It is proposed that interaction of the excited electron with the PQDs surface trap states at room temperature.* [133] Once excited the electron can jump from the conduction band to the trap state and then back to the conduction band with its transition energy being provided from phonons resulting in a longer lifetime, and the energy schematic of this is shown in Fig. 5.6 E. However, once the temperature drops below the gap between the conduction band and this defect energy level, the electron can no longer freely move between the CB and the defect level resulting in radiative emission at lower energy than the band gap, this is shown in Fig. 5.6 F. With this crossover happening at 80K using the well-known formula  $K_bT$  places the trap state energy at 6.8meV below the conduction band.

By examining the remaining 3 species PL maps in Fig. 5.7 A/B/C a similar trend appears, with the kink at 90K and the emerging of a lower energy defect peak. By resubscribing to the idea that the better passivized the PQDs are the fewer trap states they have then the FWHM increase from 80K to 20K acts as a good indicator of how many trap states are active at low temperatures. Fitting the curves in Fig5.6 A and 5.7 A/B/C we see a FWHM increase of (.3 meV/Kelvin) for BZA-BA, (.14meV/Kelvin) BZA-PAA, IPBZA-BA (.75 meV/Kelvin), IPBZA-PAA (1meV/Kelvin). Comparing this to room temperature QY intensities an interesting but somewhat obvious connection between the QY and PQD functionalization quality emerges, suggesting that better passivized QD's removes more of these trap states.

Moving on to the change in the lifetime as a function of temperature shown in Fig. 5.7 D/E, all species show varying changes with temperature but on average show a decrease in lifetime with temperature, after the 150K point. PQD's tend to have lifetimes that decrease with temperature, opposite to the expected result of increased lifetimes due to more pure excitonic recombination. This is due to the proposed mechanism of defect, conduction band coupling that can increase the lifetime in perovskites. BZA-BA and BZA-PAA have similar trends to one another in that they show small changes in their respective lifetimes. While the magnitude of IPBZA-BA and IPBZA-PAA lifetimes are different their behaviors with temperature are similar, with little change until 100K-150K then a sharp decrease.

## Phonon Energies

Using the Gaussian fit extracted FWHM vs. temperature data from 250 K to 100 K and fitting them with the equation  $\Gamma(T) = \Gamma_0 + \Gamma_{op} \exp(\hbar\omega/k_bT - 1)$  the phonon energies ( $\hbar\omega$ ) for each PQD species can be extracted. [133] Where  $\Gamma_0$  is the in-homogeneous broadening and  $\Gamma_{op}$  describes the exciton- optical phonon contributions to the spectral broadening where the specific phonon energies are described by  $\hbar\omega_{op}$ . Longitudinal optical phonon energies ( $\hbar\omega_{op}$ ) extracted from fits were  $26.1 \pm 3.2$  meV for BZA-BA,  $24.0 \pm 1.5$  meV for BZA-PAA,  $12 \pm 4.5$  meV for IPBZA-BA, and  $20 \pm 1$  meV for

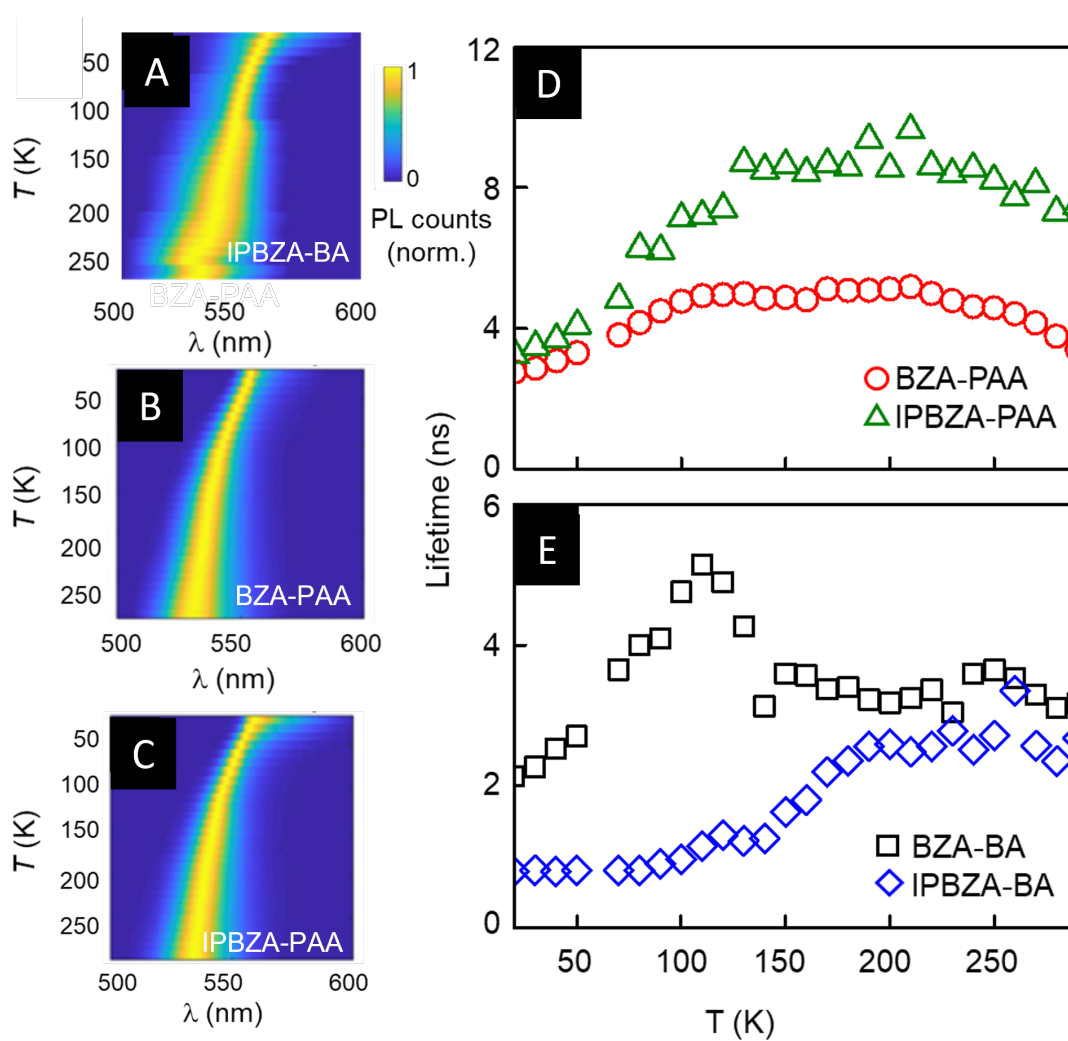


Figure 5.7: **Temperature Dependent PL & TRPL** A/B/C: Temperature dependent PL maps of IPBZA-BA/BZA-PAA/IPBZA-PAA. D/E: Lifetime dynamics of the PPA/BA species.

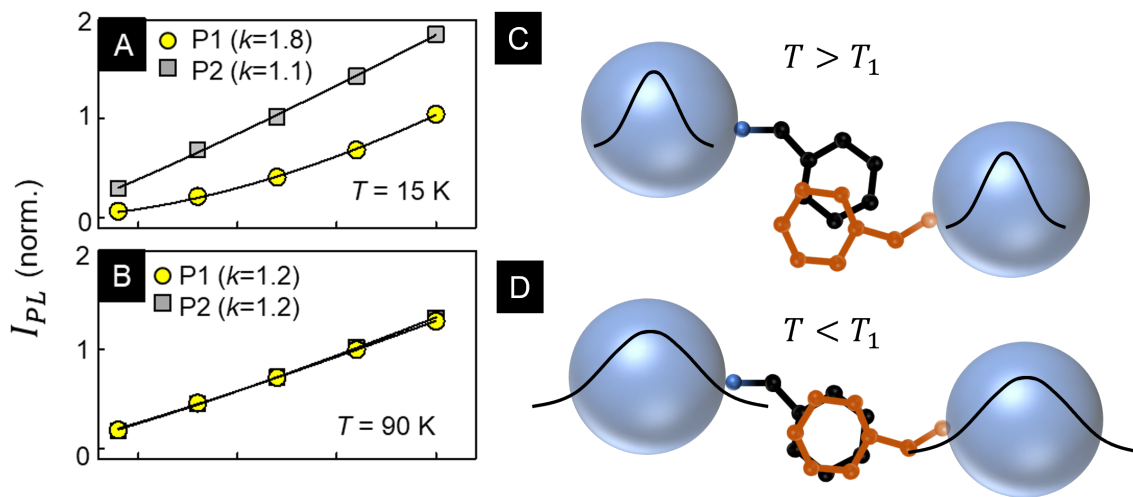


Figure 5.8: **Cryogenic Free Charges** A: Temperature Dependent PL Map, B: Spectra of BAZ-BA at 150K, 90K and 30K, C/D: Wavelength/FWHM shift with temperature of BZA-BA. E/F: Energy level diagram of PQD at 300K/20K.

IPBZA-PAA.

### Delocalisation of Charge

In addition to the TDPL and TDTRPL measurements, PDPL series were also conducted on a BZA-BA film at different temperatures shown in Fig. 5.8 A/B. The data shows power dependencies at 15/90 K in Fig. 5.8 A/b, respectively, with power fit, extracted  $K$  values inset. Yellow represents the main peak in Fig. 5.7 A, while the grey curve is the defect emission. At 90 K both peaks show relatively bound recombination while moving to 15 K we see no change in the defect peak recombination and a completely free charge recombination in the main peak. We speculate that at room temperature, the ligands overlap somewhat causing a small delocalization of charge, while below some temperature  $T_1$  the ligands snap together forming a ligand condensate allowing a strong delocalization of charges.

## 5.4 Conclusion

The data shown displays a high conductivity for all aromatic ligand - PQD species in this paper, with BA showing the highest conductivity but PAA showing more consistency across different concentrations. In addition, PL and TRPL spectra reveal that the ligands used are arresting the orthorhombic phase of the PQD ensemble, maintaining the highly attractive qualities of the cubic and tetragonal phases. In

addition, a connection is demonstrated between the functionalization quality of the PQDs and the density of trap states at low temperatures. The varying lifetimes with temperature suggest that different aromatic ligand combinations would be beneficial for different applications. For PQD films to be used for Photovoltaics or LEDs BZA-BA as the most conductive species would be the strongest candidate however if degradation is expected, BZA-PAA may be more beneficial as the longer PAA ligands may maintain higher conductivity during a decrease in concentration due to degradation in the film. For space-based photovoltaics, a consistent electron lifetime and an arrested orthorhombic phase are highly beneficial for strong operation making BZA-PAA a strong candidate.

# Chapter 6

## PQD Single Photon Emitters

Many current and developing quantum-based technologies and experiments rely on the controlled generation of single photons. [2] The last 10 years have seen an increase in single-photon emitting materials from optically active defects in Diamond, 2 Dimensional materials to individual colloidal quantum dots. From these materials coherent single-photon operation has been seen at cryogenic temperatures however, room temperature operation is incoherent. Recent inorganic colloidal PQD have demonstrated their ability to act as highly pure single-photon emitters at both cryogenic and room temperatures placing them on the list of possible coherent single-photon emitters (SPEs). What makes perovskite different from other SPE systems is the tunability across the entire visible spectrum through chemical and morphological manipulations.

### 6.1 Quantum Emitter Basics

Despite the myriad of SPE technologies they all work relatively the same, in the imitation of a two-level atomic system. This is similar to the photoluminescence process detailed in Appendix A.2. In this imitation of a two-level system, an electron is excited from some ground state ( $\langle 1 \rangle$ ) to an excited state  $\langle 2 \rangle$ . After spending some amount of time in this excited state the electron relaxes from the  $\langle 2 \rangle \rightarrow \langle 1 \rangle$  emitting a photon equal to that of the energy gap between  $\langle 1 \rangle$  and  $\langle 2 \rangle$ . For a quantum emitter to act as a good SPE it needs three things.

1. Suppressed Multi-Exciton Emission
2. Reliable Generation of Single Photons
3. Photons generated are Indistinguishable

### 6.1.1 Photon Purity

Within electronic systems, there is always the possibility of multi-photon generation. In which, upon being excited the system will emit two photons at once instead of two. Single photon systems need to produce only one photon at a time, Under measurement, this is metric is known as photon purity. This is measured as an inverse percentage, meaning the closer to zero the better. The gap between the dip at zero time delay and 0 is the photon purity.

### 6.1.2 Repetition-Rate

Many applications for SPEs will require not just pure single-photon emission but consistent emission as well. Most applications require a rep-rate of  $10^6$  photons per second. This translates to a 1 milisecond excitonic lifetime, assuming a quantum yield of 100%. The lifetime of typical solid state emitters are less than 1 millisecond, typically on the order of 1 to 10 ns. It then becomes a matter of ensuring reliable generation. The metric for this will be the excitonic lifetime of the system,  $\tau$ .

### 6.1.3 Indistinguishabilty

In an SPE system, the indistinguishability of an emitter is determined by its linewidth, in comparison to its lifetime-limited linewidth, as discussed in Appendix ???. Making the metric of indistinguishably the emitters linewidth  $\lambda$ , compared to its lifetime-limited linewidth,  $\frac{\hbar}{2\tau}$ . Some SPE systems do not require indistinguishable photons, however, what typically causes distinguishability in an SPE system (defects, stray charge interactions and phonons) can also limit its effectiveness in other areas. That is why decreasing linewidths to as little as possible is beneficial to an SPE system.

## 6.2 State of SPE Research

For a quantum emitter to act as an SPE its emission needs to be either spatially or spectrally isolated from other emitters, this limits most bulk semiconductors as candidates as there is too high of a chance to emit more than one photon at a time. This leaves:

1. Defects in Crystals
2. Strain Induced Quantum Dots
3. Epitaxial Grown Quantum Dots
4. Colloidal Quantum Dots

Sample	Oper. Temp	CP	Operation Energy	$G_2(0)$	$\lambda / \frac{\hbar}{2\tau}$
Defects in h-BN	300K	No	530 nm - 760 nm	.27	$4\mu\text{eV}/30\text{meV}$
Strain Induced 0-D States (WS2)	4K	Yes	760 nm - 820 nm	.1-.2	$.84\mu\text{eV}/33\text{meV}$
Self-assembled QDs (InAs/GaAs)	4K	Yes	885 nm - 950 nm	.02	$1\mu\text{eV}/10\mu\text{eV}$
Colloidal QDs (PQDs)	4K	Yes	410 nm - 900 nm	.01	$10\mu\text{eV}/100\mu\text{eV}$

Table 6.1: **Sate of SPE Technologies [2]** Table listing the current values of SPE technologies including: Operation Temperature, Operation Wavelength, Photon Purity and Lifetime Limited Linewidth.

The energy levels for these systems are generated through quantum confinement.

**1) Defects in Crystals:** A defect in a crystal will cause an interruption in the crystal lattice and can cause energetically deep or shallow levels in the bandgap of that material. This can lead to a delta potential of an infinite potential well that can confine an electron within a system. This system is typically fed by actively exciting the host crystal's VB to CB transition and letting this defect trap an electron. However, direct excitation of a VB to Defect transition has been observed. The most common example of this type is optically active defects in diamonds. [2]

**2) Strain Induced Quantum Dots:** Are typically fabricated by straining a monolayer Transition Metal Dichalcogenide (TMDC) allowing localized confinement of the electrons in the mono-layers semiconducting energy levels due to the strain induce change in band-structure to generate small areas in which an electron can be confined. The easiest generation of this was demonstrated by draping a semiconductor monolayer atop a set of regular occurring micron-sized plasmonic pillars. [134] The TMDC monolayer atop the pillars becomes confined and acts as a single-photon emitter. This has also been achieved by draping monolayer TMDCs atop holes in a substrate.

**3) Epitaxial Grown Quantum Dots:** These dots are grown through precise layering techniques, building up the structure of a device atom layer by atom layer. Due to this meticulous synthesis, they are the most coherent quantum emitters to date, achieving uncertainty-limited linewidths. [135] In addition, the dots are often built into diode structures allowing electrical tuning through a stark shift. However, these devices can be cost-prohibitive to manufacture, requiring millions in equipment and years of fabrication experience.

**4) Colloidal Quantum Dots:** Are dubbed this due to their simple, low temperature, wet bench synthesis, often requiring few steps and materials to fabricate. The two most common types of colloidal quantum dot systems are II-IV core-shell and perovskites.

The current performance of these technologies is summarised in Table 6.1. Table 6.1 uses the three metrics discussed earlier: Photon Purity ( $G_2(0)$ ), Rep rate ( $\tau$ ) and linewidth/uncertainty limited linewidth  $\lambda / \frac{\hbar}{2*\tau}$ , along with the added metrics of controlled placement (CP), and operation temperature and wavelength.



## 6.3 Core Shell Colloidal Quantum Dots

Core-shell quantum dots are the most commonly used, specifically cadmium selenide (CdSe) / cadmium sulfide (CdS) core-shell quantum dots. Both the CdSe and CdS layers being semiconductors they both can absorb and emit light greater than or equal to their bandgap, however, when this structure is shrunk to nano-scales, approximately 6 nanometers (nm) for the CdSe core quantum confinement takes over. The energetics of the two materials is such that the CdS confines the electrons in the CdSe core, to the core itself. Similar to the CdSe/CdS structure is that of cadmium selenide (CdSe) / Zinc sulfide (ZnS) sharing many of the same characteristics. Similar to most quantum dots the emission wavelengths of the dots are size-tunable.

### 6.3.1 Progress to date

The first colloidal quantum dots demonstration as an SPE was done by Messin *et al.* in 2000 using the CdSe/CdS structure opening the door for the next 20 years of research into these dots as a single SPEs. [136] In 2001 Messin and group continued their work in demonstrating that their CdSe/CdS structure could produce single dots that had photon purities over 90% under continuous-wave excitation with lifetimes of 20 ns, improved from their previous reporting. [137] The year 2004 saw two demonstrations of colloidal CdSe/ZnS as room temperature SPEs. Brokmann et al showed that these dots when tuned into resonance with excitation light, could act as a highly Pure emitter with photon purities of .04. [138] Adding to this discovery, Brookman and group followed up with an additional demonstration of these emitters colloidal CdSe/ZnS, now specifically focusing on the emission intermittency in the dots due to Auger recombination, also known as "Blinking". [139] The demonstration of the limitations in these dots due to blinking inspired research into its mitigation, specifically by surface modification. Yuan and the group demonstrated the ability to manipulate the on-off times of the blinking within the CdSe/ZnS quantum dots by changing the ligands that fictionalize the shell of these core-shell dots. [140] They demonstrated blinking suppression of up to 18% from their modifications. The spectral diffusion in the CdSe/ZnS was investigated in 2008 by Coolen and the group using a technique called photon correlation Fourier Spectroscopy. The measurement is similar to the anti-bunching measurement previously discussed but with the addition of a variable path length to one of the detectors. The addition of small path lengths corresponds to an increase in the temporal sensitivity of measurements on the system. Through this technique, they measured a linewidth of  $6.4 \mu\text{eV}$  for these dots with spectral diffusion of  $4 \mu\text{eV}$ . [141] 2009 saw a branching out of the types of colloidal dots core-shell dots studied for SPEs. Spinicelli and the group demonstrated that in core-shell CdSe/CdS dots, larger CdS shells around the CdSe cores would reduce the blinking in the dots. Using the thickness as a tunable parameter, they were able to uncover infor-

mation about the different decay paths in these dots. [142] A conference publication in 2011 demonstrated the tunability of these SPE's by the demonstration that dot-in-rod CdSe/CdS heterostructures acted as polarized single-photon emitters. [143] The heterostructures are a simple CdSe core inside a CdS "shell" that is elongated like a magnetic stir bar, commonly used in chemistry. These dot-in-rod shape gives rise to polarization dependent emission due to changes to the dot's confinement with lateral directions. The paper also demonstrated the use case for colloidal CdSe/CdS SPEs for applications in quantum cryptography. Another issue, aside from spectral fluctuations and blinking is the dot's photo-stability under irradiation. This problem was tackled by Negele and group by encasing the CdSe/CdS dots in a polymer matrix, extensively making the structure CdSe/CdS/PMMA. They displayed that this photo-stabilizes the dots at higher powers than before without affecting the photon purities of the dots themselves. [144] 2017 saw the most recent publications using CdSe/CdS dots for SPE's. Lin demonstrated electrically driven CdSe/CdS dots imbedded in a diode structure with near-perfect antibunching. [145] This, coupled with new InP/ZnSe structures with greatly increase shell size by Chandrasekaran and group showing almost 100% blinking suppression, shows that these core-shell structures are moving towards high photon purity SPE's with reliable emission. [146]

### 6.3.2 Auger Recombination in Core-Shell Nonstructures

One of the downsides to using these Core-Shell structures for SPE's is the tendency of the system to undergo blinking or the change from an emissive to non-emissive state on time scales of seconds. This blinking effect in these dots has been attributed to a process known as Auger recombination due to the generation of biexcitons in the quantum dots. Auger recombination occurs when instead of the recombining pair emitting a photon the recombination energy is donated to the other electron or hole, kicking it higher into the conduction band or lower into the valence band, for electrons and holes respectively. This Auger recombination happens on the timescale of 100's of ps while the radiative lifetime of these emitters, on the order of 10's of ns. Auger recombination in nanocrystals that approach their host materials bohr radius have high probabilities of auger recombination when a biexciton is generated due to the reduced dimensionality of these structures. This process becomes an issue when one of the charges, electron or hole, is ejected from the dot. This can happen in two ways, the electron is ejected from the dot into the shell of the core/shell quantum dot, or the hole is ejected into the shell. Both processes result in non-emissive states within the dots until the charge makes its way back to the dot. This limits the application of these dots' uses for quantum technologies as reliable on-demand generation is a requirement for all applications of these emitters.

As mentioned in the previous section, action has been taken over the last two decades to arrest this ionization to achieve a blink-free core-shell single quantum

dot. Yuan and the group demonstrated that by varying the ligands fictionalized to the surface of the quantum dot shell they could tune the on-off times of these dots. [140] The modifications of the ligands altered the surface energy of the dots' shells leading to changes in the duration the ionized electrons or holes were trapped within the shells. The greatest breakthrough was shown recently with 99% blink-free emission for InP/ZnSe core/shell quantum dots with large shells by Chandrasekaran and group. [146] While the time trace does show some on-off periods they are two orders of magnitude shorter than the previous dots, with 99% of the measurements occurring during an "on" period. This discovery shows significant improvement from previous technologies.

### 6.3.3 Enhanced light-matter coupling

As previously mentioned, an important parameter in SPE operation is the count rate of the emitters. It is generally agreed that a count rate of  $10^6$  photons per second is the minimum threshold for most SPE applications. A count rate of  $10^6$  photons per second corresponds to a 1 ms radiative lifetime with a 100% quantum yield. A 100% quantum yield corresponds to for every photon entering the system a photon is emitted from the system. The majority of the emitters we have currently looked at have radiative lifetimes of 10 to 20 ns but do not possess quantum yields of %100, meaning they require modification to be applicable. These modifications are made by increasing the localized electric field around the SPE to increase photon absorption. This has been achieved through the coupling of the emitters to gold substrates, plasmonic nanoparticles, and semiconductor micro-cavities.

Interaction with a gold surface was studied by Vion and group [147], and they systematically varied the coupling distance between the array of single particles and the gold surface. They demonstrated significant count rate enhancement with varying distances and significantly advanced the field for SPE operations.

## 6.4 Perovskite Quantum Dots

The next material under study for colloidal quantum dot single-photon emitters is perovskite. Perovskites have been under heavy study for the last 12 years due to their potential as low-cost, solution-processed photovoltaics. [82]

### 6.4.1 Tunability of Perovskites

The tunability of perovskite quantum dots comes from changing either their composition, specifically the halides used in the crystal structure or their size to increase or decrease quantum confinement. Offering an added advantage to perovskite quantum dots as SPE's with two bandgap tunable parameters instead of one.

### 6.4.2 Progress to date

Perovskite quantum dots were first demonstrated as SPE's in 2015 by Park and group using inorganic  $CsPbI_3$  PQDs. [34] They demonstrated at room temperature high photon purities of .06 in contrast to the fewer advantages of the large linewidth of 90 meV compared to the natural thermal decoherence linewidth of 25 meV. The second demonstration of PQD SPE's was shown in 2015 by Hu et al using  $CsPbBr_3$  quantum dots [148], showing a photon purity of .06, with a room temperature linewidth of 85 meV, almost identical to the demonstration of the  $CsPbI_3$  PQDs. Both dots also show the blinking effect that has been seen in core-shell colloidal quantum dots. However, the Blinking effect was reduced in the  $CsPbBr_3$  PQDs to the  $CsPbI_3$  PQDs. The issue of blinking in PQDs was addressed in a 2016 publication that demonstrated single-photon emission in mixed (Cl/Br) PQD's. [149] The dots showed worsened photon purities of 0.3 and a cryogenic linewidth of 1meV compared to the lifetime limited linewidth of 0.01meV. Despite the decoherence within this system, the PQDs demonstrated no blinking over a 1-minute time scale, a significant improvement from the previous two PQD SPE demonstrations. The next demonstration of PQD SPE's came in 2018 by Trinh et al. demonstrating the SPE qualities of  $FaPbBr_3$  PQDs, demonstrating of photon purities of .03 and linewidths on 100 meV at room temperature. [150] These results are similar to the previous two publications in 2015 on single halide PQD, including the blinking behavior. The most recent publication came by Utzat and group in 2019 with demonstrations of photon purities of .04, similar to previous results. [33] The advancement came with a demonstration of a cryogenic linewidth of 100  $\mu$ eV compared to the lifetime limited linewidth of 10  $\mu$ eV, attributed to better fabrication and passivation techniques developed for these PQDs in recent years.

## 6.5 Authors Work: Room Temperature Analysis of Single PQDs

As previously discussed, PQDs operate well as SPEs, displaying excellent photon purities at both room temperature and cryogenic temperatures, resulting from PQDs colloidal nature and the suppressed multiphoton processes that impart. Their biggest drawback is their incoherent operation, both at cryogenic and room temperatures. Perovskite's biggest boon for photovoltaics, their defect tolerance, becomes an issue for their SPE operation. Energetically shallow defects in the perovskites will act as scattering centers destroying coherence, thus increasing their linewidth. In this work, we examine the room temperature linewidths of High and Low-density PQD ensembles to identify trends in the linewidths of these dots as they approach single density levels. This work is very much ongoing and will be continued by graduate

students that follow after. This line of investigation is to attempt to understand the trends in PQD linewidth and to tease out the origins of the large linewidths in perovskites in general. The progress towards these goals detailed in this dissertation is an examination of the room temperature linewidths of high and low-density PQD thin films to approach the single dot regime.

### 6.5.1 Materials and Methods

Cesium Lead Bromide ( $CsPbBr_3$ ) were purchased from Sigma, product number: 900746. The PQDs are dispersed in toluene at a concentration of 10 mg/mL. These PQDs were fictionalized with, oleic acid and oleylamine, with PL emission at 510 nm. Thin films of these PQDs were synthesized by drop-casting 40  $\mu$ L of this stock PQD solution onto Glass slides. The samples were characterized using a custom-built, PL, TRPL, and Antibunching setup. As this setup was a main component of the work and combines 3 different spectroscopy techniques, it will be elaborated on in this section.

### 6.5.2 PL and Antibunching of Low-Density PQD Ensembles

The stock solution of PQDs was diluted by 1:10 and 1:100 ratios in toluene. TEM of these solutions spun coat dynamically onto atomically thin copper TEM grids at 2000 RPM for 1 min, are shown in Fig. 6.1 A and B for 1:10 and 1:100 dilutions respectively. Much of this project involved the setup of the PL/TRPL/Correlation setup shown in Fig. 6.1. The setup is excited via a MIRA 900 laser pumped with a 6W Verdi laser frequency doubled through a BBO crystal (beta-BaB2O4) to energy upconvert from 810nm to 405nm, designated by the blue line. This is directed through a series of optics into the Nikon 100x objective to the PQD samples being measured. The collected PL is shown as green dots and is directed through a series of mirrors and beamsplitters to two single-photon avalanche diodes and to fiber for PL collection. The single-photon avalanche diodes are set equidistant from the beamsplitter for antibunching measurements. An example of the PL collected from the samples is in Fig. 6.1 D. The bulk, undiluted ensemble displays an FWHM of 111 meV, most likely due to in-homogeneous broadening. The 1:100 dilutes spun coat sample displays an average FWHM of 91meV which others have reported as single PQD linewidths. [33] Fig. 6.1 E displays the antibunching curve of a spot on the 1:100 dilute sample at room temperature. The MIRA is pulsed at 77.6MHz which results in correlation peaks at that frequency, every 13 ns time delays. A true SPE would have a decreased correlation at zero which this sample doesn't. This could be due to the density of PQDs not being low enough or the PQDs having multiphoton emission at RT. More study is needed to confirm.

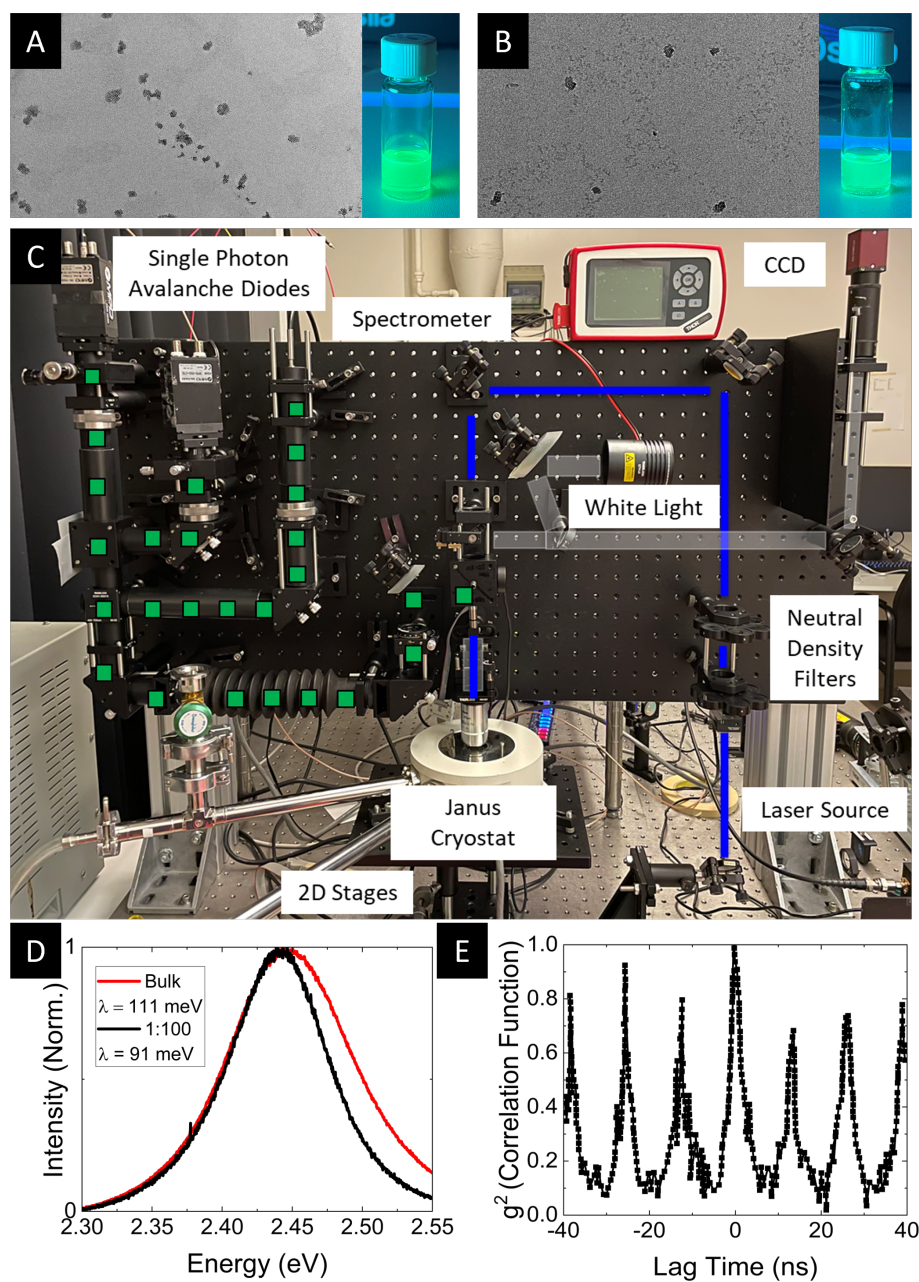


Figure 6.1: **PQD Correlations** A/B: TEM and UV-Solution images of 1:10 / 1:100 dilutions of the PQD stock. Image width is 300nm and 200nm respectively. C: PL/TRPL/Antibunching in-lab setup used to measure the PQD dilutions. D: PL of the bulk PQD ensemble versus the 1:100 dilution. E: correlation function of the 1:100 diluted spin coat samples.

## 6.6 Conclusion

In conclusion, the past 2 decades have seen a large enhancement in colloidal PQD and core-shell quantum dot SPE properties. The Blinking effect most detrimental to these dots has been addressed and suppressed successfully in both the core-shell dot and PQD structure without sacrificing performance. Photon purities of .03 have been achieved for both types of dots showing strong mono-excitonic recombination however the linewidths of both emitters have remained large compared to thermal or lifetime limits, depending on if the measurements are done at room temperature or cryogenic temperatures respectively. Some progress has been made due to better fabrication methods but the best cryogenic lifetimes reported are still an order of magnitude from being coherent, while fully coherent emitters are regularly achieved in epitaxial grown III-V dots. Not that the issue of blinking in these dots has been suppressed, the focus should shift to decreasing the decoherence in the system to decrease linewidths. In this pursuit, the room temperature dilution of PQD ensembles was studied for their SPE and PL properties. While little data of consequence was collected. A significant amount of work was made in developing this custom-built specialized PL/TRPL/Anti-bunching setup.

# Chapter 7

## Conclusion and Outlook

In this dissertation alone we have covered perovskite's applicability in photovoltaics, LEDs, and the emerging field of quantum information as possible single-photon emitters. With the multitude of applications for halide perovskites, it follows that over 10,000 publications a year concern them. The field of perovskites over the last 10 years has primarily focused on boosting efficiency in OMHP PV devices. The efficiency of OMHP PV devices increased from 12% to 25.4% over the last 10 years. In comparison to Si PV cells which have increased the same 11% over the last 45 years. This increase in efficiency has tapered off in the last few years because the field is approaching the theoretical limit of OMPH performance of 31% to 33% as defined by the Shockley Quasar limit. While this 6% gap may appear significant, it is a result of synthesis method limitations that result in uncontrolled growth leading to high defect densities. Due to this stagnation in the increasing OMHP PV efficiencies the field has split into several different directions including but not limited to:

1. OMHP Tandem PV Cells
2. Large Area Roll-to-roll OMHP PV Printing
3. Increasing OMHP Stability

One way of overcoming the stagnation in perovskite PV efficiencies is to incorporate them into a multi-junction solar cell structure, essentially two cells atop each other, focusing on collecting different regions of the solar spectra. Groups working in the field of OMPH/Si Tandems have seen PV efficiencies of above 29%. [23]. Instead of increasing PV efficiencies for OMHP, they seek to make their implementation a reality through large-area roll-to-roll printing. Groups focusing on this often use a system similar to an ink-jet printer to print meters of perovskite cells. Due to the mass-produced nature of these cells, they operate at only 15% to 18% efficiency, but research into this method has brought costs down making this a viable method.



However, despite these two promising fields, their implementation terrestrially still suffers from one key flaw, OMHP stability. Of all the new avenues mentioned, the most important, and the one most perovskites groups have switched to is increasing OMHP stability, both as a standalone absorber layer and in a PV device stack. As previously discussed perovskite films are unstable to almost all forms of stimulus they would encounter in PV operation. Even though they can reach efficiencies of 20% + they cannot maintain that efficiency under operation for longer than a year. Those cells that have achieved this feat are encapsulated by expensive polymers and glass, increasing the cost beyond large-scale feasibility. **This is the future of terrestrial OMHP research, increasing stability.**

To increase the stability of perovskites in PV, an in-depth understanding of what is driving those mechanisms is needed. Significant advancements have been made in this field over the last few years with the demonstration of ion migration through the device stack, the observed chemical degradation at perovskite interfaces, and the use of nm barrier layers over a device to block moisture and oxygen ingress. Ways of mitigating this degradation have been proposed and demonstrated to increase perovskite stability, however, the research is non-standardized and confusion in-sues. Due to the high volume publication nature of the OMHP PV field, there are often publications that seem to contradict one another. This is due to the fickle nature of perovskite synthesis, where perovskite properties can depend on the ambient humidity at the time of synthesis, airflow in the room, and room temperature. This makes it imperative that when working with and publishing on perovskites, all synthesis conditions, ratios and times a properly tracked and recorded, however, this is not always the case with the vast majority of perovskite publications. In addition, this lack of attention to detail can be found in the measurement of perovskite devices as well. Where little detail is reported on specifics of the measurement, such as temperature, power, and the errors involved. The field of perovskites would benefit from the standardization of reporting metrics to help avoid these issues.

**Beyond standardization in the field, the incorporation of non-destructive spectroscopy techniques showcased in this dissertation could significantly advance the current stability research being done.** In this dissertation alone these techniques were used to identify:

1. The shift in the bandgap of MAPI as it degrades towards lead iodide
2. Thermocycling induced strain in the MISSE 13 sample resulting in an arresting of the orthorhombic phase to low T\*
3. The arresting of the orthorhombic phase in conductive PQD's
4. Identification of charge-transfer energies in Mn doped 2-D perovskites\*
5. Generation of free charges in PQDs at low temperature\*

---

## 6. Demonstration that angstrom level changes in functionalizing ligands alter macro PQD properties

The discoveries marked with an asterisk (\*) are new to their respective fields and never previously reported. The most important technique used herein is the temperature-dependent PL and TRPL, which allowed examination of the electronic states, surface states, and structural phase of the perovskite while removing most of the 25meV of thermal background that exists at RT. All fields of perovskite research, especially PV can benefit from a broader implementation of these techniques to enhance their understanding of how the added barrier layers for stability are affecting the underlying physics in the device.

Beyond the impacts, the techniques used herein have on the field the results obtained through those techniques are promising. First and most important is the successful spaceflight of a MAPI thin film on the ISS for 10 months. Perovskites' success as a space-based PV has always been theorized but this is the first successful demonstration longer than a day. This result should drive more groups to consider researching perovskites for space-based applications and jump-start the field, now that it is been proved possible. In addition to thin films, several exciting results were made working with the lower dimensionalities of perovskites. The demonstration and calculation of cascading energy transfer in Mn doped 2-D perovskites has promising applications in polarized LEDs. In addition, the successful demonstration of spin transfer in the doped material may have exciting applications in quantum information. For the work in 0-D, PQDs the most promising result was the generation of almost entirely free charges at cryogenic temperatures, never before reported for PQDs. In addition, this work removed the bars preventing PQD implementation into devices due to their insulating nature with the introduction of PQDs functionalized with conductive ligands.

In conclusion, we have made significant advancements in the fields of; halide perovskite thin films, Mn Doped 2D perovskites, and PQD Ensembles. These advancements were made through the use of non-destructive optical spectroscopy, often employing custom-built optical setups. The key breakthroughs in all projects came from the temperature-dependent PL and TRPL measurements, epitomizing our lab's mixture of both material science and hard nonlinear physics. In addition, this highlights the importance of lowering the thermal background when investigating semiconductor phenomena in an attempt to enhance our understanding of the underlying mechanics at play.

# Appendix A

## Semiconductor Investigation Tools

The investigations into the perovskite semiconductors within this dissertation were done with both plug and play (PNP)<sup>1</sup> along with custom-built (CMB)<sup>2</sup> microscopy and spectroscopy tools. In this section, only the analysis tools used directly by our group will be detailed, not those of our collaborators. The following measurement techniques were used, followed by either the PNP or CMB designation.

1. Transmission Spectroscopy (PNP)
2. Photoluminescence Spectroscopy (CMB)
  - (a) Photon Emission Basics
  - (b) Direct Measurement of PL and TRPL
  - (c) Resorbtion
  - (d) Photo Active Stability
  - (e) Spectral Selective TRPL
  - (f) Polarization Dependent PL
  - (g) Power Dependent Excitation
  - (h) Temperature Dependent PL and TRPL
3. Microscopy (PNP)
  - (a) Confocal
  - (b) Scanning Electron

---

<sup>1</sup>**Plug and Play:** Refers to pre-built setups purchased from companies that have a set of pre-defined functions.

<sup>2</sup>**Custom Built:** Refers to setup built by our group through a combination of free space and fiber-based optics.

## (c) Tunneling Electron

For PNP measurements, the settings and some tips and tricks used will be described within the sections. The CMB measurements will be described in more detail, along with alignment techniques. The point of this section is to make the measurements used in this dissertation reproducible.

## A.1 Transmission Spectroscopy

We begin the discussion with transmission spectroscopy by describing the physics behind photon absorption in a direct gap semiconductor, followed by the experimental methods and finishing with common data processing techniques used to identify the material's band gap.

### A.1.1 Theory

Light absorption in a semiconductor is determined by the absorption coefficient,  $\alpha(\hbar\omega)$ . Starting with Fermi's Golden Rule the probability per unit time and volume,  $R(\hbar\omega)$ , shown in eq. A.1

$$R(\hbar\omega) = \frac{2\pi}{\hbar} |\langle f|H'|i \rangle|^2 \rho(E_f) \quad (\text{A.1})$$

Where  $H'$  is the Hamiltonian of the electron-radiation interaction [151], and  $\rho(E_f)$  is the density of states, at the given energy  $\hbar\omega$ . Fermi's golden rule relates to the absorption coefficient  $\alpha(\hbar\omega)$  through eq. A.2.

$$\alpha(\hbar\omega) = \frac{8\pi}{c \cdot n} \frac{\hbar\omega}{|\epsilon(\hbar\omega)|^2} R(\hbar\omega) \quad (\text{A.2})$$

Where  $\epsilon(\hbar\omega)$  is the amplitude of the incident electric field,  $n$  is the index of refraction  $c$  is the speed of light. We see that  $\alpha(\hbar\omega)$  depends on the Hamiltonian of the specific system along with the density of states at that specific energy. These two factors are material-specific, and changes in  $\alpha(\hbar\omega)$  and specific energies can indicate a change in those material properties. For example, a change in bandgap will alter the probability function ( $|\langle f|H'|i \rangle|^2$ ), of the VB and CB values, thus altering absorption characteristics. The final result of this derivation is shown in eq. A.3.

$$\alpha(\hbar\omega) = \left\{ \begin{array}{ll} 0 & \text{if } \hbar\omega \leq E_g \\ \frac{\hbar}{c \cdot n} \frac{2\pi e^2}{m} \frac{1}{\hbar\omega} \cdot |\langle f|H'|i \rangle|^2 \frac{1}{2\pi^2 \sqrt{\alpha_1 \alpha_2 \alpha_3}} \sqrt{\hbar\omega - E_g} & \text{if } \hbar\omega > E_g \end{array} \right\} \quad (\text{A.3})$$

$$E_{CV}(k) = E(0) + \alpha_1 k_1^2 + \alpha_2 k_2^2 + \alpha_3 k_3^2 \quad (\text{A.4})$$

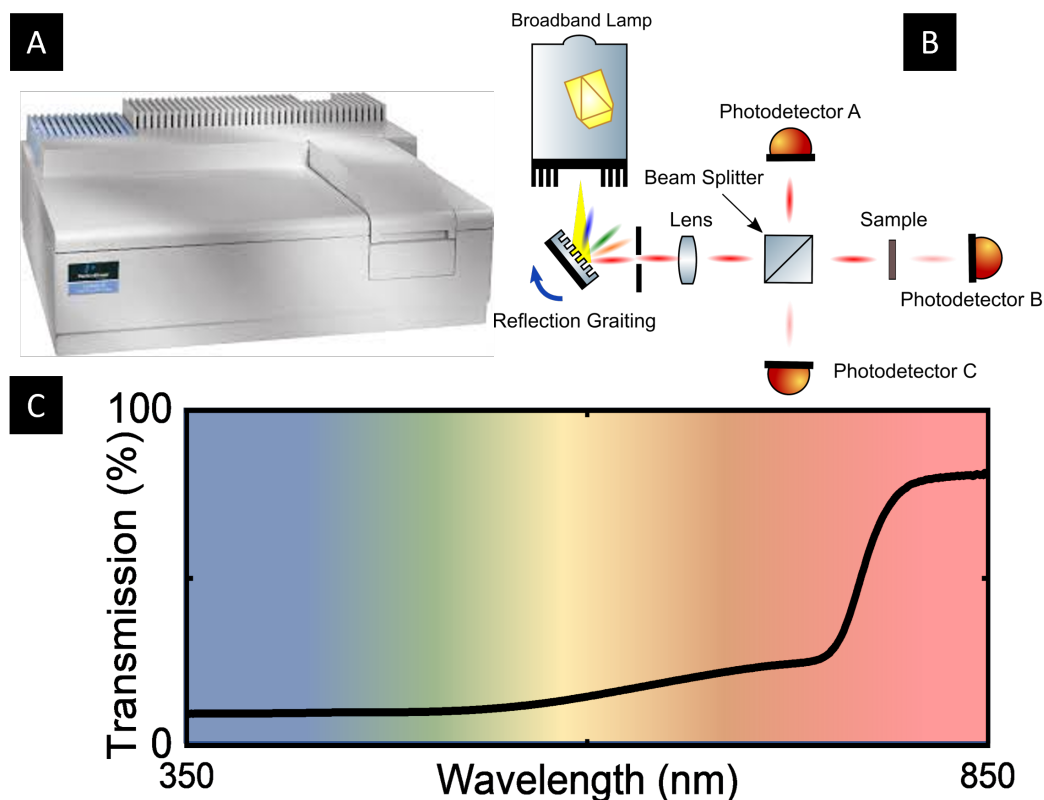


Figure A.1: **Measuring Material Transmission** A: Stock image from Perkin-Elmer. B: Optical image setup simplifying the basics of measuring a materials properties. C: Transmission curve of basic perovskite sample.

Where  $m$  is the mass of an electron,  $E_g$  is the bandgap of the material. The constants  $\alpha_{1,2,3}$  are derived from eq. A.4 the equation describing the energy function of the material. Equation A.3 leads to the phenomenon of a cut-on in the transmission curve of a semiconductor. This is where the semiconductor starts to absorb photons, as we increase in energy. The energy that this transition stops is the bandgap  $E_g$  of the material.<sup>3</sup>

### A.1.2 Experimental

All measurements within this dissertation were performed with a Perkin-Elmer 400 UV-Vis spectrometer, shown in Fig. A.1 A. This PNP setup works via funneling light from a lamp through a grating to spectrally separate the light, collimating it, and

<sup>3</sup>The full derivation for these equations can be found in chapter 5.2 of Balkan's 2012 Semiconductor Research Experimental Techniques textbook pages 128-130

sending it through the sample, shown in Fig. A.1 B. The amount of light sent into the sample is measured via beamsplitter allowing for direct measurement of the input light at photodetector A, then reflection (R) at photodetector C, and transmission (T) at photodetector B. The absorption of the material is typically measured by subtracting the reflection and transmission coefficients from 1, we get this from eq. A.5.

$$T + R + A = 1 \quad (\text{A.5})$$

However, since most solid samples are deposited on glass, the glass-sample interface can cause issues in this measurement. When working with solid samples, it is best to assume the reflection is zero, or at the least, uniform between comparative samples. This leaves equation A.6.

$$A = 1 - T \quad (\text{A.6})$$

This allows measurement of the absorption spectra by observing the transmission spectra. If a true measurement of the absorption coefficient is desired, liquid samples are typically used in quartz cuvet, which is specifically designed not to introduce extra losses in the system.

Fig. A.1 C, displays a transmission curve for a basic perovskite sample. For this curve, we can see that the material doesn't transmit much light between 350 nm and 750 nm. This light is absorbed by the material. After this, we see a cut-on in the transmission curve that we discussed in the theory section, A.1.1. These plots are helpful in determining the characteristics of the materials, as we discussed changes in the transmission curve will be caused by changes in the materials:

1. Changes in local density of states
2. Changes in materials band structure

### A.1.3 Tauc Plot Analysis

We can calculate the bandgap of material from this transmission curve through the use of a Tauc plot. Tauc pioneered this technique when working with amorphous Germanium in the 90s. The analysis is based on equation A.7.

$$(\alpha\hbar\nu)^2 = K(\hbar\nu - E_g) \quad (\text{A.7})$$

Here  $\alpha$  stands for the absorption coefficient,  $\hbar\nu$  is the photon energy, K is an energy-independent constant, and  $E_g$  is the desired value of the bandgap. Examples of this analysis are in section 3.2.2. Where we take the absorption coefficient in eq. A.7 to be 1-T at that energy.

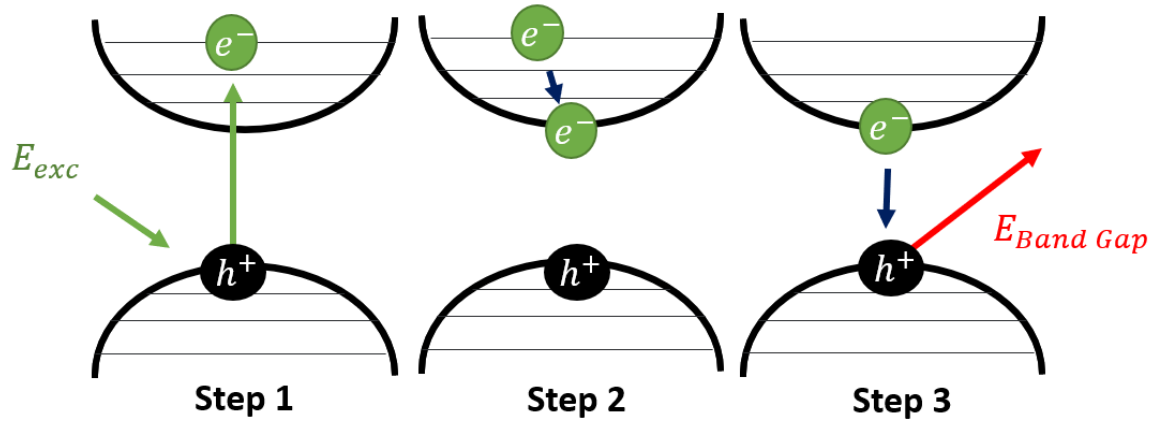


Figure A.2: **Electronic Transitions in Semiconductor** Basic cartoon of photoexcitation, non radiative decay to band edge and recombination of the electron and hole resulting in emission of a photon.

## A.2 Photoluminescence (PL) Spectroscopy

All samples studied in this dissertation are solid-state semiconductor-based. They operate by being optically excited into radiative emission by laser light and all can be simplified into a standard 3-level system shown in Fig. A.2. These electronic structures are formed by the band gaps created by the semiconductor hosts and in some cases, quantum confinement.

### A.2.1 Photon Emission Basics [1]

- Step 1:** The semiconductor absorbs a photon of energy higher than the bandgap of the material exciting an electron from the valence band to the continuum states above the conduction band, leaving a positively charged hole behind.
- Step 2:** The electron and or hole releases energy in the form of phonons and relaxes down to the lowest level in the conduction band. (Only electron shown in Fig. A.2)
- Step 3:** The electron then relaxes back down to the valence band, recombining with the hole and releasing a photon of energy equal to the bandgap.

To quantify this excitation and relaxation process we need to look closer at this process. When a pulsed ( $< 100ps$ ) wave of an incident electromagnetic field interacts with the system it produces an incident Coherence wave (C) that is initially in phase with the electromagnetic pulse. While the Coherence wave is in phase with the field the system is in complete coherence. The first scattering process the system interacts

with begins to decohere the system, the time it takes the decoherence to reach  $e^{-1}$  is the coherence lifetime  $T_2$  of the system. The Coherence decay can be described by Equation A.8.

$$C = C_0 \exp(-t/T_2) \quad (\text{A.8})$$

### Homogeneous Broadening

The following are different things within the quantum emitter system that can destroy its coherence.

1. Scattering with Phonons
2. Scattering with other Excitations
3. Scattering at Impurities of Defects
4. Recombination

If nothing acts on the system to decohere it the coherence will be lost in the recombination of the electron-hole pair. If we describe the system to have a number density of excited electrons  $N(t)$ , with an average recombination lifetime  $T_1$ , then.

$$N = N_0 e^{-t/T_1} \quad (\text{A.9})$$

Knowing that the number density  $N$  is proportional to the Coherence wave squared. Leading to Equation 3 and the simplified relation in Equation 4.

$$N_0 e^{-t/T_1} \propto [C_0 \exp(-t/T_2)]^2 \quad (\text{A.10})$$

$$T_2 \leq 2T_1 \quad (\text{A.11})$$

This suggests that in a fully coherent system where the only coherence destroying process in the system is recombination then  $T_2 = 2T_1$ . If  $T_2 < 2T_1$  then there are some decoherence effects within the system. Most of these decoherence effects are caused by the interaction of the system with some "Bath" that is spatially or electronically separate from the specific system. It is possible to pull characteristics of the emitter from the radiative lifetimes and the linewidth,  $T_1, \lambda$  respectively. Using the uncertainty principle in equation 5 and correlating the uncertainty in time to the radiative lifetime of the excitation we arrive at equation 6.

$$\Delta E \Delta t \leq \frac{\hbar}{2} \quad (\text{A.12})$$

$$\Delta E \leq \frac{\hbar}{T_2} \quad (\text{A.13})$$



Where  $\Delta E$  is proportional to the linewidth of the emitter,  $\lambda$ . Equation A.13 implies that the larger the lifetime the smaller the linewidth of the emitter. So an example a fully coherent emitter with a radiative lifetime of 1ns thus a coherence lifetime of 2ns should have a linewidth of roughly  $1\mu\text{eV}$ . Of course, most emitters will have defects that increase the linewidth of the emitter beyond this lower bound.

### In-homogeneous Broadening

Another factor that will increase the linewidth of the emitter, especially during practical measurements is the measurement of an ensemble of emitters in comparison to a single emitter. This is described as in-homogeneous broadening within the emitter. Small changes in the local band gaps of the material, will cause the linewidth of the emitter to artificially broaden.

### A.2.2 Direct Measurement of PL and TRPL

A custom-built PL and TRPL setup, similar to the one shown in Fig. A.3 was used to collect all PL and TRPL in this dissertation. In this setup, a collimated laser source, shown in blue, is directed using two mirrors<sup>4</sup>, through a short pass filter, beam splitter, and optical objective and is then focused to a point at the focal point of the objective. The short-pass filter serves to filter out any higher-order bands that exist within the laser so they do not interfere with the collection of the higher wavelength emission of the sample. For example, using a 430nm laser, exciting a material that emits at 510nm, it is recommended to use a 450nm short-pass filter. This will only let light lower than 450nm in wavelength through, cutting off any higher-order bands from the laser. The beam splinter serves as a tool to separate the collection and excitation paths. The beam splitter splits the light along two perpendicular vectors along the same plane. In this case, one continues to the objective while the other is reflected and is sent to a power meter, so laser power can be monitored during measurements. The excitation light then passes into the objective and is focused down onto the sample. The size of the excitation spot is determined by equation A.14

$$SpotSize = 0.63 * \lambda * NA \tag{A.14}$$

Where  $\lambda$  is the wavelength of the laser, and NA is the numerical aperture of the objective being used. The focal length and numeric aperture of the objective are specific to manufacturers. The three objectives used in this dissertation are listed in table A.1

Where the Spot size is reported in the metric of its diameter. The laser light hitting the sample at the focal spot is absorbed and remitted by the sample being measured.

---

<sup>4</sup>Typically two mirrors are needed when aligning a beam. One for each degree of freedom. With two mirrors and knowledge -it is possible to redirect a beam along any vector desired.

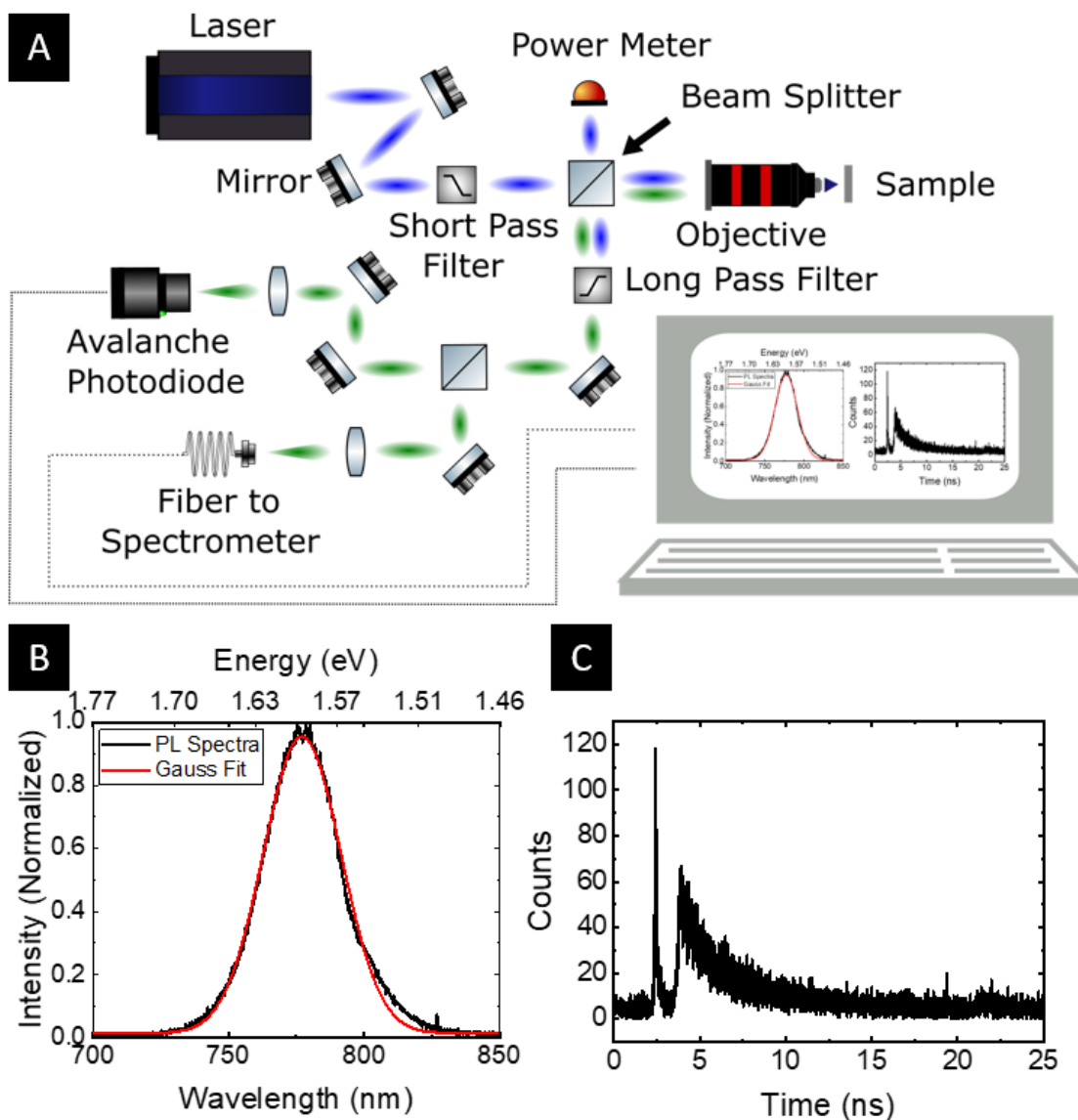


Figure A.3: **PL/TRPL Collection Setup** A: Typical PL/TRPL setup used in the collection of PL and TRPL data within this dissertation. B: Example of a MAPI PL spectra at room temperature, with the corresponding TRPL curve shown in C.

In this diagram, the blue 430nm is remitted as 532nm emission. This green emission, along with the reflected laser light is collected by the objective and collimated and sent back along the beam path. Half the green emission and laser reflection are redirected along the collection path by the beam splitter and pass through the long-pass filter. The long-pass filter is picked to cut out the laser reflection without affecting emission. Since the short pass used for this setup was 450nm, to cut the other end of the spectra,

Objective	Focal Length	NA	Spot Size @ 532nm
4x Olympus	2.5cm	.27	5 $\mu\text{m}$
10x Olympus	1cm	.4	1.5 $\mu\text{m}$
100x Nikon	5mm	.7	.7 $\mu\text{m}$

Table A.1: **Objectives Used:** This table lists the objectives used in this study.

a 450nm long-pass filter was used, to fully cut out all laser signals. From here the emission is redirected with mirrors and focused into two lenses that focus into an optical fiber to a spectrometer and the single-photon avalanche photo-diode (SPAD). The SPAD is a photo-detector sensitive enough to detect and store arrival times of single photons in 4 ps time bins. The spectrometer disperses the collected light across a camera resulting in the spectra shown in Fig. A.3. Analysis of the PL spectra is completed by fitting the PL with a Gaussian shown in equation A.15.

$$I_{PL} = ae^{-4\ln(2)(x-x_{Center})^2/FWHM^2} \quad (\text{A.15})$$

Where  $I_{PL}$  is the intensity shown in the spectra in A.3 B, while x is the wavelength value for each intensity point. The values extracted from the fit are an (amplitude of the Gaussian),  $x_{Center}$  (center wavelength of Gaussian), and the FWHM (Full-Width Half Max of Gaussian). This correlates to the intensity and linewidth of the emitter. The intensity is calculated by equation A.16

$$Intensity = a * FWHM * \sqrt{2\pi} \quad (\text{A.16})$$

Where the linewidth of the emitter correlates directly to the FWHM pulled from the Gaussian fit.

The other half of the detection channel directs the emitted light into a photodiode for the TRPL measurement. For TRPL a pulsed laser source is required. PL can be done with a continuous wave laser or a pulsed laser but TRPL requires a pulsed laser. The laser source used in this dissertation is variable between 77.6MHz and 2.5MHz. The photodiode in this measurement communicates with a correlator, that also communicates with the laser source. The laser source sends a pulse of light onto the sample, this sends a signal to the correlator to have the photodiode start counting. The photodiode resets at the start of the next pulse, beginning collection of photons again. This generates a profile of millions of photons added together that looks similar to the TRPL curve in Fig. A.3 C. Here the sharp peak is the laser reflection from the sample that bleeds through the high-pass filter. This laser peak generates an excited electron population in the sample. As that population starts to recombine emitting light we see a quick rise in counts, followed by gradual decay. Fitting this curve with the exponential decay function shown in equation A.17 we can extract the lifetimes of the populations,  $\tau_i$ .

$$I_{TRPL} = \sum_{n=1}^3 a_i e^{-t/\tau_i} \quad (\text{A.17})$$

Where  $I_{TRPL}$  is the intensity in the TRPL curve and  $t$  is the  $x$  values. The extracted values from the curve are the intensity  $a_i$ , which is the max counts, and  $\tau_i$ , which is the exciting lifetimes. The reason for the summation is due to multiple recombination processes that can have different excitonic lifetimes. Typically when fitting a lifetime curve a single to tri exponential curve is used to extract lifetimes, a single exponential fit is most common.

### A.2.3 Resorbtion

An application of the typical PL measurement can be used to measure the intra-bandgap defects within a thin film sample through a resorption measurement. The setup for this is shown in Fig. A.4 A. In this setup, the sample is mounted so that the middle of the edge of the film is aligned with the center of the fiber leading to the spectrometer. Next, the film is excited at the opposite end of the sample from the collection's spot. The emission from the film can be totally internally reflected within the film itself. While totally internally reflected within the film the emission from the film is being absorbed and remitted from the perovskite over and over. This leaves the emission red-shifted significantly compared to the collection through the normal incidence. For example, the normal incidence average energy of the MAPI film is 1.59 eV, compared to the maximum redshift energy of 1.572 eV, a total shift of 28 eV. This redshift is a measure of the intra-bandgap defects within the perovskite film.

### A.2.4 Photo-active Stability

Another application of photoluminescence is measuring the chemical stability of a semiconductor under solar AM1.5 illumination. Fig. A.4 C displays a laboratory image of the collection setup for the photo-active stability measurement. The spectra of AM1.5 is displayed in Fig. A.4 D, top panel. The photoluminescence of MAPI is centered at 770nm so a 725nm short-pass filter before the sample, a 725nm long-pass after the sample but before the collection fiber to the spectrometer. This allows the collection of the PL from the sample without the noise from the above MAPI bandgap wavelengths. An example of the collected PL over time is in the bottom panel of Fig. A.4 D. Acquisitions were taken every 10 seconds for the first 20 minutes and then once every five minutes for the remainder of the test. The FWHM and center wavelength of the PL is also tracked as a function of time. TRPL is not possible due to the un-pulsed nature of the AM1.5 light source.

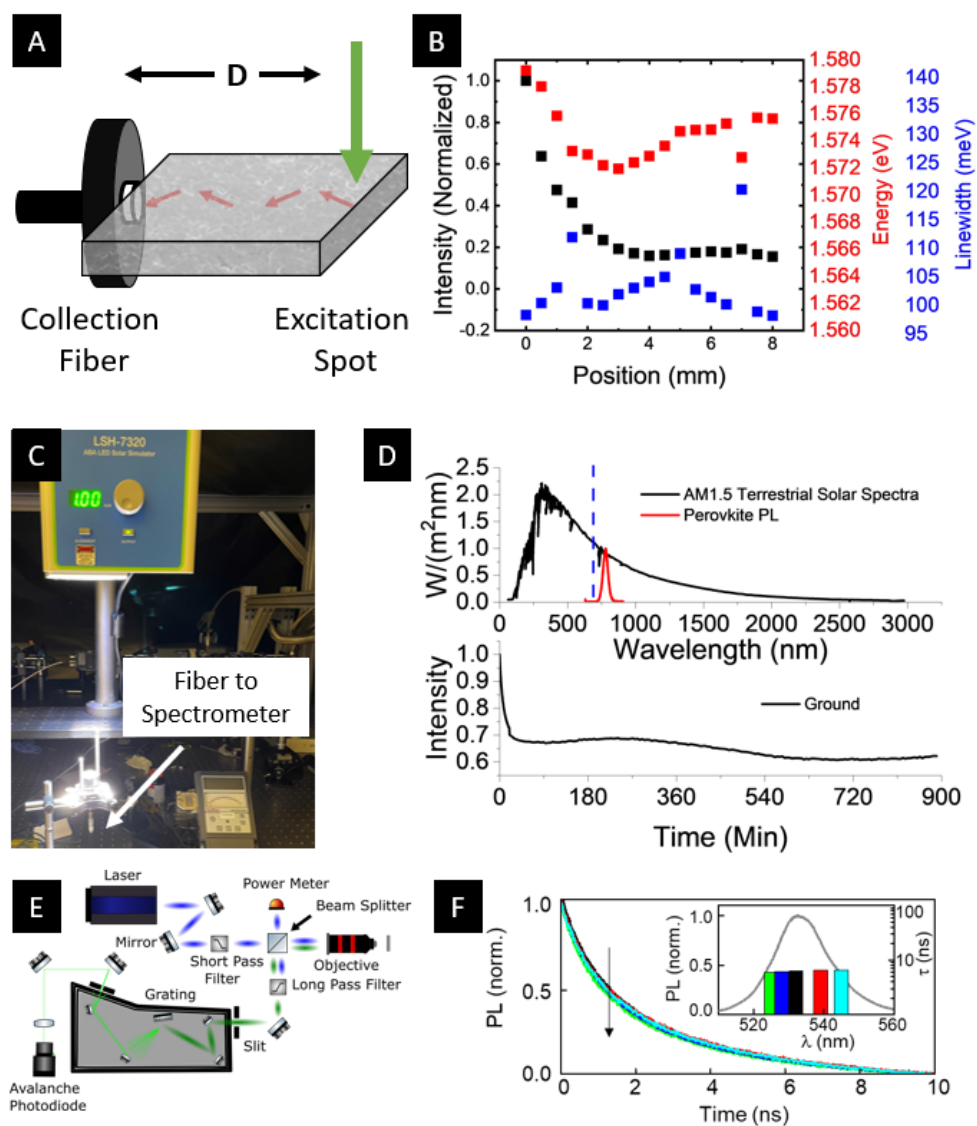


Figure A.4: **Re-Absorption / Photo-active Stability / Spectral Selective TRPL** A: Typical edge collection setup to measure total internal reflection from the emission of the film. B: The results of the Gaussian fit from the resorption measurement on a MAPI film. C: Image from the lab of the AM1.5 photoexcitation setup. D: TOP PANEL) Displays the solar spectrum of the sun terrestrially, with MAPI PL shown in red. The blue line signifies the short-pass filter used before the sample and the long-pass filter used after the sample. BOTTOM PANEL) The PL intensity decay of a typical encapsulated MAPI sample. E: Displays the spectrally selective TRPL setup, with the data acquired from a typical PQD sample in F.

### A.2.5 Spectral Selective TRPL

A specific application of TRPL is to spectrally select the emission wavelengths of the PL to filter out different contributions of different components, this is shown in Fig. A.4 E. In this design, the excitation branch doesn't change but the collection arm is redesigned. The collected emission is redirected into a spectrometer through the entrance slit. The emission is then directed to a grating that spectrally disperses the light which is then redirected out the exit slit. By closing the exit slit it is possible to select a narrow portion of the PL spectra. This light is then directed into the single-photon avalanche diode, typical of the TRPL measurement. This is particularly helpful for analyzing colloidal quantum dot emissions. A common effect in colloidal samples is Foster Resonance Energy Transfer. In this, smaller, higher energy dots donate electrons to close, larger, low energy dots. This results in short lifetimes at the low wavelength/high energy end of the spectra and long lifetimes at the high wavelength/low energy end. A small example of this can be seen in the TRPL curves in Fig. A.4 F. Where the lifetimes increase slightly as the wavelength selection increases. The width of the bar plot signifies the width of the collection range.

### A.2.6 Power Dependent Excitation Spectroscopy

An important measurement for investigating semiconductors with PL and TRPL is the modulation of the excitation lasers' power, typically across 3 orders of magnitude. The setup for this measurement is identical to Fig. A.3 A with the addition of a gradual neutral density filter to allow variation of excitation power. This measurement gives insight into the exciting electron population dynamics within a semiconductor. PL from a power series is analyzed by a traditional Gaussian fit where the extracted intensity is plotted as a function of excitation power. This data is then fit to the power law in equation A.18.

$$I_{PL} = aP^k \quad (\text{A.18})$$

Where  $I_{PL}$  is the measured PL intensity and P is the power at each collection. The extracted values are a, an arbitrary constant, and k is the excitonic species designation. The following designations are:

1.  $k = 1 \rightarrow$  Only Bond Recombination
2.  $1 < k < 2 \rightarrow$  A mixture of Free and Bond Recombination
3.  $k > 2 \rightarrow$  Pure Free Recombination

Where bound emission refers to emission from a recombining electron-hole pair in an exciton. Free recombination refers to when an unbound electron and an unbound hole

recombine. Typically in a confined system like a quantum dot, bound recombination dominates, however, in a semiconductor like MAPI, the exciton binding energy is low enough that electrons disassociate and become free, allowing for free recombination. Typically, a value of less than 1 is a result of the power being too high, thus saturating the emissive qualities of the perovskite.

### A.2.7 Temperature Dependent Spectroscopy

One final and very powerful tool when doing PL and TRPL measurements is temperature dependence. This is accomplished by collecting PL and TRPL from the sample while heating or cooling it. This is typically achieved via a Cryostat to cool samples from RT to as low as 4 K. In this work, two types of cryostats were used, a closed system helium cryostat and a flow cryostat. The closed-loop helium cryostat works similar to a traditional refrigerator, just at an ultra-high vacuum. While the flow cryostat utilizes a cryogenic liquid such as liquid helium or nitrogen. This liquid is guided through a chamber below the sample, passively cooling it to the temperature of the liquid used, 77K and 4K for nitrogen and helium respectively. Cooling a sample down to cryogenic temperatures removes the added noise to the semiconductor's emission that comes from the thermal background. This thermal background is given by  $1/2k_bT$ , where  $k_b$ <sup>5</sup> is the Boltzman constant and T is the temperature. At 300k this value is 25 meV, occupying 25% of a typical MAPI film's linewidth at RT. However, at 10 K this value is less than 1meV, occupying only 4% of the typical MAPI linewidth at 10K. This reduction in the thermal background is a powerful tool to identify underlying interactions that are being swamped out at RT.

## A.3 Microscopy

Multiple forms of microscopy were used in this dissertation all in the PNP style. They included:

1. Talos F200C G2 Transmission Electron Microscope
2. LSM880 confocal Microscope
3. Zeiss Gemini 500 SEM

All TEM images in this document were taken with identical conditions save the magnification and or substrate. Substrates used were either atomically thin copper or a lacy carbon mesh. A scale bar will be included with all TEM images the author captured in the work in this dissertation along with substrate type. All confocal

---

<sup>5</sup>8.617 x 10<sup>-5</sup> eV K<sup>-1</sup>

images were taken with a 405nm diode laser with a scan size of 1/2 mm by 1/2 mm. All SEM images were taken at various magnifications with a 2 nA beam intensity.



# Bibliography

- [1] C. F. C. F. Klingshirn, *Semiconductor optics*. Springer, 2012.
- [2] I. Aharonovich, D. Englund, and M. Toth, “Solid-state single-photon emitters,” *Nature Photonics*, vol. 10, pp. 631–641, oct 2016.
- [3] R. Schneider, F. Weigert, V. Lesnyak, S. Leubner, T. Lorenz, T. Behnke, A. Dubavik, J. O. Joswig, U. Resch-Genger, N. Gaponik, and A. Eychmüller, “PH and concentration dependence of the optical properties of thiol-capped CdTe nanocrystals in water and D2O,” *Physical Chemistry Chemical Physics*, vol. 18, no. 28, pp. 19083–19092, 2016.
- [4] W. J. Yin, J. H. Yang, J. Kang, Y. Yan, and S. H. Wei, “Halide perovskite materials for solar cells: A theoretical review,” *Journal of Materials Chemistry A*, vol. 3, pp. 8926–8942, may 2015.
- [5] M. Hao, Y. Bai, S. Zeiske, L. Ren, J. Liu, Y. Yuan, N. Zarrabi, N. Cheng, M. Ghasemi, P. Chen, M. Lyu, D. He, J. H. Yun, Y. Du, Y. Wang, S. Ding, A. Armin, P. Meredith, G. Liu, H. M. Cheng, and L. Wang, “Ligand-assisted cation-exchange engineering for high-efficiency colloidal  $Cs_{x-1}FA_xPbI_3$  quantum dot solar cells with reduced phase segregation,” *Nature Energy*, vol. 5, pp. 79–88, jan 2020.
- [6] C. Hanmandlu, S. Swamy, A. Singh, H.-A. Chen, A. Mohapatra, C.-C. Liu, C.-S. Lai, C.-W. Pao, P. Chen, and C. W. Chu, “Suppression of Surface Defects to Achieve Hysteresis-Free Inverted Perovskite Solar Cells via Quantum Dots Passivation,” *Journal of Materials Chemistry A*, vol. 8, pp. 5263–5274, mar 2020.
- [7] O. Ouellette, A. Lesage-Landry, B. Scheffel, S. Hoogland, F. P. García de Arquer, and E. H. Sargent, “Spatial Collection in Colloidal Quantum Dot Solar Cells,” *Advanced Functional Materials*, vol. 30, p. 1908200, jan 2020.
- [8] G. Li, J. Huang, Y. Li, J. Tang, and Y. Jiang, “Highly bright and low turn-on voltage CsPbBr<sub>3</sub> quantum dot LEDs via conjugation molecular ligand exchange,” *Nano Research*, vol. 12, pp. 109–114, jan 2019.

- 
- [9] C. Ding, F. Liu, Y. Zhang, D. Hirotsu, X. Rin, S. Hayase, T. Minemoto, T. Masuda, R. Wang, and Q. Shen, "Photoexcited hot and cold electron and hole dynamics at FAPbI<sub>3</sub> perovskite quantum dots/metal oxide heterojunctions used for stable perovskite quantum dot solar cells," *Nano Energy*, vol. 67, p. 104267, jan 2020.
- [10] J. Xue, R. Wang, L. Chen, S. Nuryyeva, T. Han, T. Huang, S. Tan, J. Zhu, M. Wang, Z. Wang, C. Zhang, J. Lee, and Y. Yang, "A Small-Molecule "Charge Driver" enables Perovskite Quantum Dot Solar Cells with Efficiency Approaching 13%," *Advanced Materials*, vol. 31, p. 1900111, sep 2019.
- [11] Q. Zhao, A. Hazarika, X. Chen, S. P. Harvey, B. W. Larson, G. R. Teeter, J. Liu, T. Song, C. Xiao, L. Shaw, M. Zhang, G. Li, M. C. Beard, and J. M. Luther, "High efficiency perovskite quantum dot solar cells with charge separating heterostructure," *Nature Communications*, vol. 10, pp. 1–8, dec 2019.
- [12] X. Ling, S. Zhou, J. Yuan, J. Shi, Y. Qian, B. W. Larson, Q. Zhao, C. Qin, F. Li, G. Shi, C. Stewart, J. Hu, X. Zhang, J. M. Luther, S. Duhm, and W. Ma, "14.1% CsPbI<sub>3</sub> Perovskite Quantum Dot Solar Cells via Cesium Cation Passivation," *Advanced Energy Materials*, vol. 9, p. 1900721, jul 2019.
- [13] D. Ghosh, M. Y. Ali, D. K. Chaudhary, and S. Bhattacharyya, "Dependence of halide composition on the stability of highly efficient all-inorganic cesium lead halide perovskite quantum dot solar cells," *Solar Energy Materials and Solar Cells*, vol. 185, pp. 28–35, oct 2018.
- [14] B. R. Sutherland and E. H. Sargent, "Perovskite photonic sources," may 2016.
- [15] F. Liu, Y. Zhang, C. Ding, S. Kobayashi, T. Izuishi, N. Nakazawa, T. Toyoda, T. Ohta, S. Hayase, T. Minemoto, K. Yoshino, S. Dai, and Q. Shen, "Highly Luminescent Phase-Stable CsPbI<sub>3</sub> Perovskite Quantum Dots Achieving Near 100% Absolute Photoluminescence Quantum Yield," *ACS Nano*, vol. 11, pp. 10373–10383, oct 2017.
- [16] Y.-H. Suh, T. Kim, J. W. Choi, C.-L. Lee, and J. Park, "High-Performance CsPbX<sub>3</sub> Perovskite Quantum-Dot Light-Emitting Devices via Solid-State Ligand Exchange," *ACS Applied Nano Materials*, vol. 1, pp. 488–496, feb 2018.
- [17] Z. Shi, S. Li, Y. Li, H. Ji, X. Li, D. Wu, T. Xu, Y. Chen, Y. Tian, Y. Zhang, C. Shan, and G. Du, "Strategy of Solution-Processed All-Inorganic Heterostructure for Humidity/Temperature-Stable Perovskite Quantum Dot Light-Emitting Diodes," *ACS Nano*, vol. 12, pp. 1462–1472, feb 2018.

- 
- [18] Q. Zhang, Y. Lu, Z. Liu, H. Yu, Y. Duan, L. Liu, S. Chen, and W. Huang, “Highly efficient organic-inorganic hybrid perovskite quantum dot/nanocrystal light-emitting diodes using graphene electrode and modified PEDOT:PSS,” *Organic Electronics*, vol. 72, pp. 30–38, sep 2019.
- [19] Y. Li, S. Chou, P. Huang, C. Xiao, X. Liu, Y. Xie, F. Zhao, Y. Huang, J. Feng, H. Zhong, H. Sun, and Q. Pei, “Stretchable Organometal-Halide-Perovskite Quantum-Dot Light-Emitting Diodes,” *Advanced Materials*, vol. 31, p. 1807516, may 2019.
- [20] E. T. Vickers, E. E. Enlow, W. G. Delmas, A. C. Dibeneditto, A. H. Chowdhury, B. Bahrami, B. W. Dreskin, T. A. Graham, I. N. Hernandez, S. A. Carter, S. Ghosh, Q. Qiao, and J. Z. Zhang, “Enhancing Charge Carrier Delocalization in Perovskite Quantum Dot Solids with Energetically Aligned Conjugated Capping Ligands,” *ACS Energy Letters*, pp. 817–825, 2020.
- [21] H.-S. Yun, K. Noh, J. Kim, S. H. Noh, G.-H. Kim, W. Lee, H. B. Na, T.-S. Yoon, J. Jang, Y. Kim, and S.-Y. Cho, “CsPbBr<sub>3</sub> Perovskite Quantum Dot Light-Emitting Diodes Using Atomic Layer Deposited Al<sub>2</sub>O<sub>3</sub> and ZnO Interlayers,” *physica status solidi (RRL) – Rapid Research Letters*, vol. 14, p. 1900573, jan 2020.
- [22] Y. Wang, Y. Teng, P. Lu, X. Shen, P. Jia, M. Lu, Z. Shi, B. Dong, W. W. Yu, and Y. Zhang, “Low Roll-Off Perovskite Quantum Dot Light-Emitting Diodes Achieved by Augmenting Hole Mobility,” *Advanced Functional Materials*, p. 1910140, mar 2020.
- [23] “Best Research-Cell Efficiency Chart — Photovoltaic Research — NREL.”
- [24] J. J. Berry, J. van de Lagemaat, M. M. Al-Jassim, S. Kurtz, Y. Yan, and K. Zhu, “Perovskite Photovoltaics: The Path to a Printable Terawatt-Scale Technology,” *ACS Energy Letters*, vol. 2, pp. 2540–2544, nov 2017.
- [25] Y. Y. Zhang, S. Chen, P. Xu, H. Xiang, X. G. Gong, A. Walsh, and S. H. Wei, “Intrinsic Instability of the Hybrid Halide Perovskite Semiconductor CH<sub>3</sub>NH<sub>3</sub>PbI<sub>3</sub>\*,” *Chinese Physics Letters*, vol. 35, p. 036104, mar 2018.
- [26] S. Yakunin, L. Protesescu, F. Krieg, M. I. Bodnarchuk, G. Nedelcu, M. Humer, G. De Luca, M. Fiebig, W. Heiss, and M. V. Kovalenko, “Low-threshold amplified spontaneous emission and lasing from colloidal nanocrystals of caesium lead halide perovskites,” *Nature Communications*, vol. 6, pp. 1–9, aug 2015.
- [27] Y. Gao, S. Wang, C. Huang, N. Yi, K. Wang, S. Xiao, and Q. Song, “Room temperature three-photon pumped CH<sub>3</sub>NH<sub>3</sub>PbBr<sub>3</sub> perovskite microlasers,” *Scientific Reports*, vol. 7, pp. 1–6, mar 2017.

- 
- [28] T. B. Song, T. Yokoyama, C. C. Stoumpos, J. Logsdon, D. H. Cao, M. R. Wasielewski, S. Aramaki, and M. G. Kanatzidis, "Importance of reducing vapor atmosphere in the fabrication of Tin-based perovskite solar cells," *Journal of the American Chemical Society*, vol. 139, pp. 836–842, jan 2017.
- [29] Y. Li, W. Yan, Y. Li, S. Wang, W. Wang, Z. Bian, L. Xiao, and Q. Gong, "Direct Observation of Long Electron-Hole Diffusion Distance in CH<sub>3</sub>NH<sub>3</sub>PbI<sub>3</sub> Perovskite Thin Film," *Scientific Reports*, vol. 5, p. 14485, sep 2015.
- [30] S. Sarang, S. Bonabi Naghadeh, B. Luo, P. Kumar, E. Betady, V. Tung, M. Scheibner, J. Z. Zhang, and S. Ghosh, "Stabilization of the Cubic Crystalline Phase in Organometal Halide Perovskite Quantum Dots via Surface Energy Manipulation.," *The journal of physical chemistry letters*, vol. 8, pp. 5378–5384, nov 2017.
- [31] S. B. Naghadeh, S. Sarang, A. Brewer, A. Allen, Y. H. Chiu, Y. J. Hsu, J. Y. Wu, S. Ghosh, and J. Z. Zhang, "Size and temperature dependence of photoluminescence of hybrid perovskite nanocrystals," *Journal of Chemical Physics*, vol. 151, p. 154705, oct 2019.
- [32] L. Protesescu, S. Yakunin, M. I. Bodnarchuk, F. Krieg, R. Caputo, C. H. Hendon, R. X. Yang, A. Walsh, and M. V. Kovalenko, "Nanocrystals of Cesium Lead Halide Perovskites (CsPbX<sub>3</sub>, X = Cl, Br, and I): Novel Optoelectronic Materials Showing Bright Emission with Wide Color Gamut," *Nano Letters*, vol. 15, pp. 3692–3696, jun 2015.
- [33] H. Utzat, W. Sun, A. E. K. Kaplan, F. Krieg, M. Ginterseder, B. Spokoyny, N. D. Klein, K. E. Shulenberger, C. F. Perkinson, M. V. Kovalenko, and M. G. Bawendi, "Coherent single-photon emission from colloidal lead halide perovskite quantum dots.," *Science (New York, N.Y.)*, vol. 363, pp. 1068–1072, mar 2019.
- [34] Y. S. Park, S. Guo, N. S. Makarov, and V. I. Klimov, "Room Temperature Single-Photon Emission from Individual Perovskite Quantum Dots," *ACS Nano*, vol. 9, pp. 10386–10393, aug 2015.
- [35] A. R. Chakhmouradian and P. M. Woodward, "Celebrating 175 years of perovskite research: A tribute to roger h. mitchell," *Physics and Chemistry of Minerals*, vol. 41, pp. 387–391, 5 2014.
- [36] H. D. Megaw, "Crystal structure of barium titanate," *Nature 1945 155:3938*, vol. 155, pp. 484–485, 1945.

- 
- [37] C. C. Stoumpos, C. D. Malliakas, and M. G. Kanatzidis, “Semiconducting tin and lead iodide perovskites with organic cations: Phase transitions, high mobilities, and near-infrared photoluminescent properties,” *Inorganic Chemistry*, vol. 52, pp. 9019–9038, aug 2013.
- [38] A. Poglitsch, D. Weber, A. Poglitsch, and D. Weber, “Dynamic disorder in methylammoniumtrihalogenoplumbates (II) observed by millimeter-wave spectroscopy,” *JChPh*, vol. 87, no. 11, pp. 6373–6378, 1987.
- [39] G. P. Nagabhushana, R. Shivaramaiah, and A. Navrotsky, “Direct calorimetric verification of thermodynamic instability of lead halide hybrid perovskites,” *Proceedings of the National Academy of Sciences of the United States of America*, vol. 113, pp. 7717–7721, jul 2016.
- [40] C. Yi, J. Luo, S. Meloni, A. Boziki, N. Ashari-Astani, C. Grätzel, S. M. Za-keeruddin, U. Röthlisberger, and M. Grätzel, “Entropic stabilization of mixed A-cation ABX<sub>3</sub> metal halide perovskites for high performance perovskite solar cells,” *Energy & Environmental Science*, vol. 9, pp. 656–662, feb 2016.
- [41] Y. Zhou and Y. Zhao, “Chemical stability and instability of inorganic halide perovskites,” *Energy & Environmental Science*, vol. 12, pp. 1495–1511, may 2019.
- [42] J. A. Christians, P. A. Miranda Herrera, and P. V. Kamat, “Transformation of the Excited State and Photovoltaic Efficiency of CH<sub>3</sub>NH<sub>3</sub>PbI<sub>3</sub> Perovskite upon Controlled Exposure to Humidified Air,” *Journal of the American Chemical Society*, vol. 137, pp. 1530–1538, feb 2015.
- [43] S. N. Habisreutinger, T. Leijtens, G. E. Eperon, S. D. Stranks, R. J. Nicholas, and H. J. Snaith, “Carbon Nanotube/Polymer Composites as a Highly Stable Hole Collection Layer in Perovskite Solar Cells,” *Nano Letters*, vol. 14, pp. 5561–5568, oct 2014.
- [44] A. J. Pearson, G. E. Eperon, P. E. Hopkinson, S. N. Habisreutinger, J. T. Wang, H. J. Snaith, and N. C. Greenham, “Oxygen Degradation in Mesoporous Al<sub>2</sub>O<sub>3</sub>/CH<sub>3</sub>NH<sub>3</sub>PbI<sub>3-x</sub>Cl<sub>x</sub> Perovskite Solar Cells: Kinetics and Mechanisms,” *Advanced Energy Materials*, vol. 6, p. 1600014, jul 2016.
- [45] D. Bryant, N. Aristidou, S. Pont, I. Sanchez-Molina, T. Chotchunangatchaval, S. Wheeler, J. R. Durrant, and S. A. Haque, “Light and oxygen induced degradation limits the operational stability of methylammonium lead triiodide perovskite solar cells,” *Energy & Environmental Science*, vol. 9, pp. 1655–1660, may 2016.

- 
- [46] N. Aristidou, C. Eames, I. Sanchez-Molina, X. Bu, J. Kosco, M. S. Islam, and S. A. Haque, “Fast oxygen diffusion and iodide defects mediate oxygen-induced degradation of perovskite solar cells,” *Nature Communications*, vol. 8, p. 15218, aug 2017.
- [47] N. Aristidou, I. Sanchez-Molina, T. Chotchuangchutchaval, M. Brown, L. Martinez, T. Rath, and S. A. Haque, “The Role of Oxygen in the Degradation of Methylammonium Lead Trihalide Perovskite Photoactive Layers,” *Angewandte Chemie*, vol. 127, pp. 8326–8330, jul 2015.
- [48] J. A. Christians, P. Schulz, J. S. Tinkham, T. H. Schloemer, S. P. Harvey, B. J. Tremolet de Villers, A. Sellinger, J. J. Berry, and J. M. Luther, “Tailored interfaces of unencapsulated perovskite solar cells for >1,000 hour operational stability,” *Nature Energy*, vol. 3, pp. 68–74, jan 2018.
- [49] C. C. Boyd, R. Checharoen, T. Leijtens, and M. D. McGehee, “Understanding Degradation Mechanisms and Improving Stability of Perovskite Photovoltaics.,” *Chemical reviews*, vol. 119, pp. 3418–3451, mar 2019.
- [50] M. R. Filip and F. Giustino, “The Geometric Blueprint of Perovskites,” *Proceedings of the National Academy of Sciences of the United States of America*, vol. 115, pp. 5397–5402, may 2018.
- [51] B. Conings, J. Drijkoningen, N. Gauquelin, A. Babayigit, J. D’Haen, L. D’Olieslaeger, A. Ethirajan, J. Verbeeck, J. Manca, E. Mosconi, F. D. Angelis, and H.-G. Boyen, “Intrinsic Thermal Instability of Methylammonium Lead Trihalide Perovskite,” *Advanced Energy Materials*, vol. 5, p. 1500477, aug 2015.
- [52] J. Zhao, Y. Deng, H. Wei, X. Zheng, Z. Yu, Y. Shao, J. E. Shield, and J. Huang, “Strained hybrid perovskite thin films and their impact on the intrinsic stability of perovskite solar cells,” *Science Advances*, vol. 3, nov 2017.
- [53] V. K. Ravi, G. B. Markad, and A. Nag, “Band Edge Energies and Excitonic Transition Probabilities of Colloidal CsPbX<sub>3</sub> (X = Cl, Br, I) Perovskite Nanocrystals,” *ACS Energy Letters*, vol. 1, pp. 665–671, oct 2016.
- [54] M. Weiss, J. Horn, C. Richter, and D. Schlettwein, “Preparation and characterization of methylammonium tin iodide layers as photovoltaic absorbers,” *physica status solidi (a)*, vol. 213, pp. 975–981, apr 2016.
- [55] Z. Xiao, L. Zhao, N. L. Tran, Y. L. Lin, S. H. Silver, R. A. Kerner, N. Yao, A. Kahn, G. D. Scholes, and B. P. Rand, “Mixed-Halide Perovskites with Stabilized Bandgaps.,” *Nano letters*, vol. 17, pp. 6863–6869, nov 2017.

- 
- [56] D. W. Kim, E. D. Jung, C. H. Jang, J. A. Hong, H. S. Kim, Y. W. Noh, and M. H. Song, "Cs incorporation via sequential deposition for stable and scalable organometal halide perovskite solar cells," *Journal of Power Sources*, vol. 520, p. 230783, feb 2022.
- [57] J.-W. Lee, D.-H. Kim, H.-S. Kim, S.-W. Seo, S. Min Cho, N.-G. Park, J.-w. Lee, D.-h. Kim, H.-s. Kim, S.-w. Seo, S. M. Cho, and N.-g. Park, "Formamini-dinium and Cesium Hybridization for Photo- and Moisture-Stable Perovskite Solar Cell," *Advanced Energy Materials*, vol. 5, p. 1501310, oct 2015.
- [58] G. Kim and A. Petrozza, "Defect Tolerance and Intolerance in Metal-Halide Perovskites," *Advanced Energy Materials*, vol. 10, p. 2001959, oct 2020.
- [59] N.-G. Park and K. Zhu, "Scalable fabrication and coating methods for perovskite solar cells and solar modules," *Nature Reviews Materials 2020 5:5*, vol. 5, pp. 333–350, 2 2020.
- [60] Y. Miyazawa, M. Ikegami, H. W. Chen, T. Ohshima, M. Imaizumi, K. Hirose, and T. Miyasaka, "Tolerance of perovskite solar cell to high-energy particle irradiations in space environment," *iScience*, vol. 2, pp. 148–155, 4 2018.
- [61] Y. Tu, J. Wu, M. Zheng, J. Huo, P. Zhou, Z. Lan, J. Lin, and M. Huang, "Tio2 quantum dots as superb compact block layers for high-performance ch3nh3pb3 perovskite solar cells with an efficiency of 16.97vol. 7, pp. 20539–20546, 12 2015.
- [62] S. Kanaya, G. M. Kim, M. Ikegami, T. Miyasaka, K. Suzuki, Y. Miyazawa, H. Toyota, K. Osonoe, T. Yamamoto, and K. Hirose, "Proton irradiation tolerance of high-efficiency perovskite absorbers for space applications," *The Journal of Physical Chemistry Letters*, vol. 10, pp. 6990–6995, 11 2019.
- [63] Y. Tu, G. Xu, X. Yang, Y. Zhang, Z. Li, R. Su, D. Luo, W. Yang, Y. Miao, R. Cai, L. Jiang, X. Du, Y. Yang, Q. Liu, Y. Gao, S. Zhao, W. Huang, Q. Gong, and R. Zhu, "Mixed-cation perovskite solar cells in space," *Science China Physics, Mechanics & Astronomy 2019 62:7*, vol. 62, pp. 1–4, 2 2019.
- [64] L. K. Reb, M. Böhmer, B. Predeschly, S. Grott, C. L. Weindl, G. I. Ivandekic, R. Guo, C. Dreißigacker, R. Gernhäuser, A. Meyer, and P. Müller-Buschbaum, "Perovskite and organic solar cells on a rocket flight," *Joule*, vol. 4, pp. 1880–1892, 9 2020.
- [65] I. Cardinaletti, T. Vangerven, S. Nagels, R. Cornelissen, D. Schreurs, J. Hruby, J. Vodnik, D. Devisscher, J. Kesters, J. D'Haen, A. Franquet, V. Spampinato, T. Conard, W. Maes, W. Deferme, and J. V. Manca, "Organic and perovskite solar cells for space applications," *Solar Energy Materials and Solar Cells*, vol. 182, pp. 121–127, 8 2018.

- 
- [66] W. A. Dunlap-Shohl, Y. Zhou, N. P. Padture, and D. B. Mitzi, “Synthetic Approaches for Halide Perovskite Thin Films.,” *Chemical reviews*, vol. 119, pp. 3193–3295, mar 2019.
- [67] A. Kojima, K. Teshima, Y. Shirai, and T. Miyasaka, “Organometal halide perovskites as visible-light sensitizers for photovoltaic cells.,” *Journal of the American Chemical Society*, vol. 131, pp. 6050–1, may 2009.
- [68] Z. Xiao, C. Bi, Y. Shao, Q. Dong, Q. Wang, Y. Yuan, C. Wang, Y. Gao, and J. Huang, “Efficient, high yield perovskite photovoltaic devices grown by interdiffusion of solution-processed precursor stacking layers,” *Energy & Environmental Science*, vol. 7, pp. 2619–2623, jul 2014.
- [69] N. J. Jeon, J. H. Noh, Y. C. Kim, W. S. Yang, S. Ryu, and S. I. Seok, “Solvent engineering for high-performance inorganic-organic hybrid perovskite solar cells,” *Nature materials*, vol. 13, no. 9, pp. 897–903, 2014.
- [70] O. G. Reid, M. Yang, N. Kopidakis, K. Zhu, and G. Rumbles, “Grain-Size-Limited Mobility in Methylammonium Lead Iodide Perovskite Thin Films,” *ACS Energy Letters*, vol. 1, pp. 561–565, sep 2016.
- [71] J. Schlipf, L. Bießmann, L. Oesinghaus, E. Berger, E. Metwalli, J. A. Lercher, L. Porcar, and P. Müller-Buschbaum, “In Situ Monitoring the Uptake of Moisture into Hybrid Perovskite Thin Films,” *The Journal of Physical Chemistry Letters*, vol. 9, pp. 2015–2021, apr 2018.
- [72] T. J. Peshek, W. Delmas, M. Bush, D. Torres-Gonzalez, S. Khayat, S. Ghosh, J. W. Williams, and L. McMillon-Brown, “Systematic Study of Space-Grade Encapsulants and Barrier Layers for durability of MAPbI<sub>3</sub>,” *Conference Record of the IEEE Photovoltaic Specialists Conference*, vol. 2020-June, pp. 1121–1123, jun 2020.
- [73] V. Adinolfi, W. Peng, G. Walters, O. M. Bakr, and E. H. Sargent, “The Electrical and Optical Properties of Organometal Halide Perovskites Relevant to Optoelectronic Performance,” *Advanced Materials*, vol. 30, p. 1700764, jan 2018.
- [74] R. Thirsk, A. Kuipers, C. Mukai, and D. Williams, “The space-flight environment: the international space station and beyond,” *CMAJ*, vol. 180, pp. 1216–1220, 6 2009.
- [75] A. D. Sheikh, R. Munir, M. A. Haque, A. Bera, W. Hu, P. Shaikh, A. Amassian, and T. Wu, “Effects of High Temperature and Thermal Cycling on the Performance of Perovskite Solar Cells: Acceleration of Charge Recombination and Deterioration of Charge Extraction,” *ACS Applied Materials and Interfaces*, vol. 9, pp. 35018–35029, oct 2017.



- 
- [76] J. He, T. Li, X. Liu, H. Su, Z. Ku, J. Zhong, F. Huang, Y. Peng, and Y. B. Cheng, "Influence of phase transition on stability of perovskite solar cells under thermal cycling conditions," *Solar Energy*, vol. 188, pp. 312–317, aug 2019.
- [77] C. Gueymard, D. Myers, and K. Emery, "Proposed reference irradiance spectra for solar energy systems testing," *Solar Energy*, vol. 73, pp. 443–467, dec 2002.
- [78] M. Ouafi, B. Jaber, L. Atourki, R. Bekkari, and L. Laânab, "Improving UV stability of MAPbI<sub>3</sub> perovskite thin films by bromide incorporation," *Journal of Alloys and Compounds*, vol. 746, pp. 391–398, may 2018.
- [79] A. Farooq, I. M. Hossain, S. Moghadamzadeh, J. A. Schwenzler, T. Abzieher, B. S. Richards, E. Klampaftis, and U. W. Paetzold, "Spectral Dependence of Degradation under Ultraviolet Light in Perovskite Solar Cells," *ACS Applied Materials & Interfaces*, vol. 10, pp. 21985–21990, jul 2018.
- [80] S.-W. Lee, S. Kim, S. Bae, K. Cho, T. Chung, L. E. Mundt, S. Lee, S. Park, H. Park, M. C. Schubert, S. W. Glunz, Y. Ko, Y. Jun, Y. Kang, H.-S. Lee, and D. Kim, "UV Degradation and Recovery of Perovskite Solar Cells," *Scientific Reports*, vol. 6, p. 38150, dec 2016.
- [81] C. Inguibert and S. Messenger, "Equivalent displacement damage dose for on-orbit space applications," *IEEE Transactions on Nuclear Science*, vol. 59, no. 6, pp. 3117–3125, 2012.
- [82] Y. Chen, S. Tan, N. Li, B. Huang, X. Niu, L. Li, M. Sun, Y. Zhang, X. Zhang, C. Zhu, N. Yang, H. Zai, Y. Wu, S. Ma, Y. Bai, Q. Chen, F. Xiao, K. Sun, and H. Zhou, "Self-elimination of intrinsic defects improves the low-temperature performance of perovskite photovoltaics," *Joule*, vol. 4, pp. 1961–1976, 9 2020.
- [83] D. Shi, V. Adinolfi, R. Comin, M. Yuan, E. Alarousu, A. Buin, Y. Chen, S. Hoogland, A. Rothenberger, K. Katsiev, Y. Losovyj, X. Zhang, P. A. Dowben, O. F. Mohammed, E. H. Sargent, and O. M. Bakr, "Low trap-state density and long carrier diffusion in organolead trihalide perovskite single crystals," *Science*, vol. 347, pp. 519–522, 1 2015.
- [84] E. M. Tennyson, T. A. S. Doherty, and S. D. Stranks, "Heterogeneity at multiple length scales in halide perovskite semiconductors," *Nature Reviews Materials* 2019 4:9, vol. 4, pp. 573–587, 7 2019.
- [85] G. M. Paternò, V. Robbiano, L. Santarelli, A. Zampetti, C. Cazzaniga, V. García Sakai, and F. Cacialli, "Perovskite solar cell resilience to fast neutrons," *Sustainable Energy & Fuels*, vol. 3, pp. 2561–2566, sep 2019.

- 
- [86] S. Sarang, H. Ishihara, Y.-C. Chen, O. Lin, A. Gopinathan, V. C. Tung, and S. Ghosh, “Low temperature excitonic spectroscopy and dynamics as a probe of quality in hybrid perovskite thin films,” *Physical Chemistry Chemical Physics*, vol. 18, pp. 28428–28433, oct 2016.
- [87] W. G. Delmas, E. T. Vickers, A. C. DiBenedetto, C. Lum, I. N. Hernandez, J. Z. Zhang, and S. Ghosh, “Modulating Charge Carrier Dynamics and Transfer via Surface Modifications in Organometallic Halide Perovskite Quantum Dots,” *The Journal of Physical Chemistry Letters*, vol. 11, pp. 7886–7892, sep 2020.
- [88] E. V. Péan, C. S. De Castro, and M. L. Davies, “Shining a light on the photoluminescence behaviour of methylammonium lead iodide perovskite: investigating the competing photobrightening and photodarkening processes,” *Materials Letters*, vol. 243, pp. 191–194, may 2019.
- [89] D. Cortecchia, S. Neutzner, A. R. S. Kandada, E. Mosconi, D. Meggiolaro, F. De Angelis, C. Soci, and A. Petrozza, “Broadband emission in two-dimensional hybrid perovskites: The role of structural deformation,” *Journal of the American Chemical Society*, vol. 139, pp. 39–42, jan 2017.
- [90] K. Thirumal, W. K. Chong, W. Xie, R. Ganguly, S. K. Muduli, M. Sherburne, M. Asta, S. Mhaisalkar, T. C. Sum, H. S. Soo, and N. Mathews, “Morphology-Independent Stable White-Light Emission from Self-Assembled Two-Dimensional Perovskites Driven by Strong Exciton-Phonon Coupling to the Organic Framework,” *Chemistry of Materials*, vol. 29, pp. 3947–3953, may 2017.
- [91] Y. Chen, Y. Sun, J. Peng, J. Tang, K. Zheng, and Z. Liang, “2D Ruddlesden-Popper Perovskites for Optoelectronics,” *Advanced Materials*, vol. 30, p. 1703487, jan 2018.
- [92] H. Long, X. Peng, J. Lu, K. Lin, L. Xie, B. Zhang, L. Ying, and Z. Wei, “Exciton-phonon interaction in quasi-two dimensional layered (PEA)<sub>2</sub>(CsPbBr<sub>3</sub>): N<sub>3</sub>-1PbBr<sub>4</sub> perovskite,” *Nanoscale*, vol. 11, pp. 21867–21871, dec 2019.
- [93] Y. Li, S. Chou, P. Huang, C. Xiao, X. Liu, Y. Xie, F. Zhao, Y. Huang, J. Feng, H. Zhong, H. Sun, and Q. Pei, “Quantum Dot LEDs: Stretchable Organometal-Halide-Perovskite Quantum-Dot Light-Emitting Diodes (Adv. Mater. 22/2019),” *Advanced Materials*, vol. 31, p. 1970157, may 2019.
- [94] W. J. Mir, M. Jagadeeswararao, S. Das, and A. Nag, “Colloidal Mn-doped cesium lead halide perovskite nanoplatelets,” *ACS Energy Letters*, vol. 2, pp. 537–543, mar 2017.

- 
- [95] A. Biswas, R. Bakthavatsalam, and J. Kundu, "Efficient Exciton to Dopant Energy Transfer in Mn<sup>2+</sup>-Doped (C<sub>4</sub>H<sub>9</sub>NH<sub>3</sub>)<sub>2</sub>PbBr<sub>4</sub> Two-Dimensional (2D) Layered Perovskites," *Chemistry of Materials*, vol. 29, pp. 7816–7825, sep 2017.
- [96] S. Das Adhikari, S. K. Dutta, A. Dutta, A. K. Guria, and N. Pradhan, "Chemically Tailoring the Dopant Emission in Manganese-Doped CsPbCl<sub>3</sub> Perovskite Nanocrystals," *Angewandte Chemie*, vol. 129, pp. 8872–8876, jul 2017.
- [97] C. Sun, Z. Gao, Y. Deng, H. Liu, L. Wang, S. Su, P. Li, H. Li, Z. Zhang, and W. Bi, "Orange to Red, Emission-Tunable Mn-Doped Two-Dimensional Perovskites with High Luminescence and Stability," *ACS Applied Materials and Interfaces*, vol. 11, pp. 34109–34116, sep 2019.
- [98] J. Zhu, X. Yang, Y. Zhu, Y. Wang, J. Cai, J. Shen, L. Sun, and C. Li, "Room-Temperature Synthesis of Mn-Doped Cesium Lead Halide Quantum Dots with High Mn Substitution Ratio," *Journal of Physical Chemistry Letters*, vol. 8, pp. 4167–4171, sep 2017.
- [99] B. Luo, Y. Guo, X. Li, Y. Xiao, X. Huang, and J. Z. Zhang, "Efficient Trap-Mediated Mn<sup>2+</sup> Dopant Emission in Two Dimensional Single-Layered Perovskite (CH<sub>3</sub>CH<sub>2</sub>NH<sub>3</sub>)<sub>2</sub>PbBr<sub>4</sub>," *Journal of Physical Chemistry C*, vol. 123, pp. 14239–14245, jun 2019.
- [100] R. Bakthavatsalam, A. Biswas, M. Chakali, P. R. Bangal, B. P. Kore, and J. Kundu, "Temperature-Dependent Photoluminescence and Energy-Transfer Dynamics in Mn<sup>2+</sup>-Doped (C<sub>4</sub>H<sub>9</sub>NH<sub>3</sub>)<sub>2</sub>PbBr<sub>4</sub> Two-Dimensional (2D) Layered Perovskite," *Journal of Physical Chemistry C*, vol. 123, pp. 4739–4748, feb 2019.
- [101] L. Hou, Y. Zhu, J. Zhu, Y. Gong, and C. Li, "Mn-doped 2D Sn-based perovskites with energy transfer from self-trapped excitons to dopants for warm white light-emitting diodes," *Journal of Materials Chemistry C*, vol. 8, pp. 8502–8506, jul 2020.
- [102] M. Goryca, T. Kazimierzuk, M. Nawrocki, A. Golnik, J. A. Gaj, P. Kossacki, P. Wojnar, and G. Karczewski, "Optical Manipulation of a Single Mn Spin in a CdTe-Based Quantum Dot," *Physical Review Letters*, vol. 103, p. 087401, aug 2009.
- [103] C. Le Gall, L. Besombes, H. Boukari, R. Kolodka, J. Cibert, and H. Mariette, "Optical spin orientation of a single manganese atom in a semiconductor quantum dot using quaresonant photoexcitation," *Physical Review Letters*, vol. 102, p. 127402, mar 2009.

- 
- [104] R. Viswanatha, J. M. Pietryga, V. I. Klimov, and S. A. Crooker, “Spin-polarized Mn<sup>2+</sup> emission from mn-doped colloidal nanocrystals,” *Physical Review Letters*, vol. 107, p. 067402, aug 2011.
- [105] L. Besombes, Y. Leger, L. Maingault, D. Ferrand, H. Mariette, and J. Cibert, “Carrier-induced spin splitting of an individual magnetic atom embedded in a quantum dot,” *Physical Review B*, vol. 71, p. 161307, apr 2005.
- [106] A. Nag, R. Cherian, P. Mahadevan, A. V. Gopal, A. Hazarika, A. Mohan, A. S. Vengurlekar, and D. D. Sarma, “Size-dependent tuning of Mn<sup>2+</sup> d emission in Mn 2+-doped CdS nanocrystals: Bulk vs surface,” *Journal of Physical Chemistry C*, vol. 114, pp. 18323–18329, nov 2010.
- [107] R. Beaulac, P. I. Archer, S. T. Ochsenbein, and D. R. Gamelin, “Mn<sup>2+</sup>-doped CdSe quantum dots: New inorganic materials for spin-electronics and spin-photonics,” *Advanced Functional Materials*, vol. 18, pp. 3873–3891, dec 2008.
- [108] L. Besombes, Y. Léger, L. Maingault, D. Ferrand, H. Mariette, and J. Cibert, “Probing the Spin State of a Single Magnetic Ion in an Individual Quantum Dot,” *Physical Review Letters*, vol. 93, p. 207403, nov 2004.
- [109] A. L. Efros, E. I. Rashba, and M. Rosen, “Paramagnetic Ion-Doped Nanocrystal as a Voltage-Controlled Spin Filter,” *Physical Review Letters*, vol. 87, p. 206601, oct 2001.
- [110] N. Sugano, Satoru, Kojima, *Magneto-Optics*. Springer-Verlag Berlin Heidelberg, 2000.
- [111] J. Fernández-Rossier and L. Brey, “Ferromagnetism mediated by few electrons in a semimagnetic quantum dot,” *Physical Review Letters*, vol. 93, p. 117201, sep 2004.
- [112] F. Qu and P. Hawrylak, “Magnetic exchange interactions in quantum dots containing electrons and magnetic ions,” *Physical Review Letters*, vol. 95, p. 217206, nov 2005.
- [113] J. Wang, C. Zhang, H. Liu, R. McLaughlin, Y. Zhai, S. R. Vardeny, X. Liu, S. McGill, D. Semenov, H. Guo, R. Tsuchikawa, V. V. Deshpande, D. Sun, and Z. V. Vardeny, “Spin-optoelectronic devices based on hybrid organic-inorganic trihalide perovskites,” *Nature Communications*, vol. 10, pp. 1–6, dec 2019.
- [114] R. Viswanatha, J. M. Pietryga, V. I. Klimov, and S. A. Crooker, “Spin-polarized Mn<sup>2+</sup> emission from mn-doped colloidal nanocrystals,” *Physical Review Letters*, vol. 107, aug 2011.

- 
- [115] A. V. Chernenko, A. S. Brichkin, N. A. Sobolev, and M. C. Carmo, “Mechanisms of manganese-assisted non-radiative recombination in Cd(Mn)Se/Zn(Mn)Se quantum dots,” *Journal of Physics: Condensed Matter*, vol. 22, p. 355306, sep 2010.
- [116] Y. Léger, L. Besombes, L. Maingault, and H. Mariette, “Valence-band mixing in neutral, charged, and Mn-doped self-assembled quantum dots,” *Physical Review B - Condensed Matter and Materials Physics*, vol. 76, jul 2007.
- [117] C. Le Gall, L. Besombes, H. Boukari, R. Kolodka, J. Cibert, and H. Mariette, “Optical spin orientation of a single manganese atom in a semiconductor quantum dot using quasiresonant photoexcitation,” *Physical Review Letters*, vol. 102, mar 2009.
- [118] T. A. Berhe, W.-N. Su, C.-H. Chen, C.-J. Pan, J.-H. Cheng, H.-M. Chen, M.-C. Tsai, L.-Y. Chen, A. A. Dubale, and B.-J. Hwang, “Organometal halide perovskite solar cells: degradation and stability,” *Energy & Environmental Science*, vol. 9, pp. 323–356, feb 2016.
- [119] J. You, L. Meng, T. B. Song, T. F. Guo, W. H. Chang, Z. Hong, H. Chen, H. Zhou, Q. Chen, Y. Liu, N. De Marco, and Y. Yang, “Improved air stability of perovskite solar cells via solution-processed metal oxide transport layers,” *Nature Nanotechnology*, vol. 11, pp. 75–81, jan 2016.
- [120] S. Yang, W. Fu, Z. Zhang, H. Chen, and C. Z. Li, “Recent advances in perovskite solar cells: Efficiency, stability and lead-free perovskite,” jun 2017.
- [121] M. Saliba, T. Matsui, J. Y. Seo, K. Domanski, J. P. Correa-Baena, M. K. Nazeeruddin, S. M. Zakeeruddin, W. Tress, A. Abate, A. Hagfeldt, and M. Grätzel, “Cesium-containing triple cation perovskite solar cells: Improved stability, reproducibility and high efficiency,” *Energy and Environmental Science*, vol. 9, pp. 1989–1997, jun 2016.
- [122] D. Wang, M. Wright, N. K. Elumalai, and A. Uddin, “Stability of perovskite solar cells,” apr 2016.
- [123] B. Chen, J. Song, X. Dai, Y. Liu, P. N. Rudd, X. Hong, and J. Huang, “Synergistic effect of elevated device temperature and excess charge carriers on the rapid light-induced degradation of perovskite solar cells,” *Advanced Materials*, vol. 31, p. 1902413, 8 2019.
- [124] Q. V. Le, K. Hong, H. W. Jang, and S. Y. Kim, “Halide Perovskite Quantum Dots for Light-Emitting Diodes: Properties, Synthesis, Applications, and Outlooks,” *Advanced Electronic Materials*, vol. 4, p. 1800335, dec 2018.

- 
- [125] J. Xue, J. W. Lee, Z. Dai, R. Wang, S. Nuryyeva, M. E. Liao, S. Y. Chang, L. Meng, D. Meng, P. Sun, O. Lin, M. S. Goorsky, and Y. Yang, "Surface Ligand Management for Stable FAPbI<sub>3</sub> Perovskite Quantum Dot Solar Cells," *Joule*, vol. 2, pp. 1866–1878, sep 2018.
- [126] B. Luo, Y.-C. Pu, S. A. Lindley, Y. Yang, L. Lu, Y. Li, X. Li, and J. Z. Zhang, "Organolead Halide Perovskite Nanocrystals: Branched Capping Ligands Control Crystal Size and Stability," *Angewandte Chemie International Edition*, vol. 55, pp. 8864–8868, jul 2016.
- [127] A. Swarnkar, A. R. Marshall, E. M. Sanehira, B. D. Chernomordik, D. T. Moore, J. A. Christians, T. Chakrabarti, and J. M. Luther, "Quantum dot-induced phase stabilization of  $\alpha$ -CsPbI<sub>3</sub> perovskite for high-efficiency photovoltaics," *Science*, vol. 354, pp. 92–95, oct 2016.
- [128] E. T. Vickers, T. A. Graham, A. H. Chowdhury, B. Bahrami, B. W. Dreskin, S. Lindley, S. B. Naghadeh, Q. Qiao, and J. Z. Zhang, "Improving Charge Carrier Delocalization in Perovskite Quantum Dots by Surface Passivation with Conductive Aromatic Ligands," *ACS Energy Letters*, vol. 3, no. 12, pp. 2931–2939, 2018.
- [129] B. Luo, Y.-C. Pu, Y. Yang, S. A. Lindley, G. Abdelmageed, H. Ashry, Y. Li, X. Li, and J. Z. Zhang, "Synthesis, Optical Properties, and Exciton Dynamics of Organolead Bromide Perovskite Nanocrystals," *The Journal of Physical Chemistry C*, vol. 119, pp. 26672–26682, nov 2015.
- [130] J. Dai, J. Xi, L. Li, J. Zhao, Y. Shi, W. Zhang, C. Ran, B. Jiao, X. Hou, X. Duan, and Z. Wu, "Charge Transport between Coupling Colloidal Perovskite Quantum Dots Assisted by Functional Conjugated Ligands," *Angewandte Chemie International Edition*, vol. 57, pp. 5754–5758, may 2018.
- [131] S. J. Lim, L. Ma, A. Schleife, and A. M. Smith, "Quantum dot surface engineering: Toward inert fluorophores with compact size and bright, stable emission," aug 2016.
- [132] H. C. Woo, J. W. Choi, J. Shin, S. H. Chin, M. H. Ann, and C. L. Lee, "Temperature-Dependent Photoluminescence of CH<sub>3</sub>NH<sub>3</sub>PbBr<sub>3</sub> Perovskite Quantum Dots and Bulk Counterparts," *Journal of Physical Chemistry Letters*, vol. 9, pp. 4066–4074, jul 2018.
- [133] X. Yuan, P. Jing, J. Li, M. Wei, J. Hua, J. Zhao, L. Tian, and J. Li, "Temperature-dependent photoluminescence of inorganic perovskite nanocrystal films," *RSC Advances*, vol. 6, no. 82, pp. 78311–78316, 2016.

- 
- [134] C. Palacios-Berraquero, D. M. Kara, A. R. Montblanch, M. Barbone, P. Latawiec, D. Yoon, A. K. Ott, M. Loncar, A. C. Ferrari, and M. Atatüre, “Large-scale quantum-emitter arrays in atomically thin semiconductors,” *Nature Communications*, vol. 8, may 2017.
- [135] K. D. Jo, P. Atkinson, M. Mu, M. Heldmaier, S. M. Ulrich, O. G. Schmidt, and P. Michler, “Triggered Indistinguishable Single Photons with Narrow Line Widths from Site-Controlled Quantum Dots,” *Nano Lett*, vol. 13, 2013.
- [136] G. F. S. & S. K. B. P. Michler, A. Imamoglu, M. D. Mason, P. J. Carson, “Quantum correlation among photons from a single quantum dot at room temperature,” *Nature Letters*, vol. 406, 2000.
- [137] G. Messin, J. P. Hermier, E. Giacobino, P. Desbiolles, and M. Dahan, “Bunching and antibunching in the fluorescence of semiconductor nanocrystals,” *Tech. Rep.* 23, 2001.
- [138] X. Brokmann, E. Giacobino, M. Dahan, and J. P. Hermier, “Highly efficient triggered emission of single photons by colloidal CdSe/ZnS nanocrystals,” *Applied Physics Letters*, vol. 85, pp. 712–714, aug 2004.
- [139] X. Brokmann, G. Messin, P. Desbiolles, E. Giacobino, and J. P. H. M Dahan, “Colloidal CdSe/ZnS quantum dots as single-photon sources,” *New Journal of Physics*, vol. 6, mar 2004.
- [140] C. T. Yuan, W. C. Chou, Y. N. Chen, J. W. Chou, D. S. Chuu, C. A. J. Lin, J. K. Li, W. H. Chang, and J. L. Shen, “Study of fluorescence enhancement of colloidal CdSe/ZnS quantum dots bound to hexadecylamine by single-molecule measurements,” *Journal of Physical Chemistry C*, vol. 111, pp. 15166–15172, oct 2007.
- [141] L. Coolen, X. Brokmann, P. Spinicelli, and J. P. Hermier, “Emission characterization of a single CdSe-ZnS nanocrystal with high temporal and spectral resolution by photon-correlation fourier spectroscopy,” *Physical Review Letters*, vol. 100, jan 2008.
- [142] P. Spinicelli, S. Buil, X. Quélin, B. Mahler, B. Dubertret, and J. P. Hermier, “Bright and grey states in CdSe-CdS nanocrystals exhibiting strongly reduced blinking,” *Physical Review Letters*, vol. 102, mar 2009.
- [143] F. Pisanello, A. Quattieri, G. Leménager, L. Martiradonna, T. Stomeo, R. Cingolani, A. Bramati, and M. De Vittorio, “Single colloidal quantum dots as sources of single photons for quantum cryptography,” in *Quantum Dots and Nanostructures: Synthesis, Characterization, and Modeling VIII*, vol. 7947, p. 794709, SPIE, feb 2011.

- 
- [144] C. Negele, J. Haase, A. Budweg, A. Leitenstorfer, and S. Mecking, “Stable single-photon emission by quantum dot/polymer hybrid particles,” *Macromolecular Rapid Communications*, vol. 34, pp. 1145–1150, jul 2013.
- [145] C. C. Lin, K. Y. Xu, D. Wang, and A. Meijerink, “Luminescent manganese-doped CsPbCl<sub>3</sub> perovskite quantum dots,” *Scientific Reports*, vol. 7, apr 2017.
- [146] V. Chandrasekaran, M. D. Tessier, D. Dupont, P. Geiregat, Z. Hens, and E. Brainis, “Nearly Blinking-Free, High-Purity Single-Photon Emission by Colloidal InP/ZnSe Quantum Dots,” *Nano Letters*, vol. 17, pp. 6104–6109, oct 2017.
- [147] C. Vion, P. Spinicelli, L. Coolen, C. Schwob, J.-M. Frigerio, J.-P. Hermier, and A. Maître, “Controlled modification of single colloidal CdSe/ZnS nanocrystal fluorescence through interactions with a gold surface,” *Optics Express*, vol. 18, p. 7440, mar 2010.
- [148] F. Hu, H. Zhang, C. Sun, C. Yin, B. Lv, C. Zhang, W. W. Yu, X. Wang, Y. Zhang, and M. Xiao, “Superior Optical Properties of Perovskite Nanocrystals as Single Photon Emitters,” *ACS Nano*, vol. 9, pp. 12410–12416, nov 2015.
- [149] G. Rainoì, G. Nedelcu, L. Protesescu, M. I. Bodnarchuk, M. V. Kovalenko, R. F. Mahrt, and T. Stöferle, “Single Cesium Lead Halide Perovskite Nanocrystals at Low Temperature: Fast Single-Photon Emission, Reduced Blinking, and Exciton Fine Structure,” *ACS Nano*, vol. 10, pp. 2485–2490, feb 2016.
- [150] C. T. Trinh, D. N. Minh, K. J. Ahn, Y. Kang, and K. G. Lee, “Organic-Inorganic FAPbBr<sub>3</sub> Perovskite Quantum Dots as a Quantum Light Source: Single-Photon Emission and Blinking Behaviors,” *ACS Photonics*, vol. 5, pp. 4937–4943, dec 2018.
- [151] A. Patane and N. Balkan, eds., *Semiconductor Research*, vol. 150 of *Springer Series in Materials Science*. Berlin, Heidelberg: Springer Berlin Heidelberg, 2012.